

Copyright
by
James Sylvester Grundy
2018

The Dissertation Committee for James Sylvester Grundy
certifies that this is the approved version of the following dissertation:

**Effect of Dopant Level on Environmental Behavior of Doped
Nanoparticles: A Case Study of Indium Tin Oxide**

Committee:

Lynn E. Katz, Supervisor

Navid B. Saleh

Mary Jo Kirisits

Desmond F. Lawler

Delia J. Milliron

Danny D. Reible

**Effect of Dopant Level on Environmental Behavior of Doped
Nanoparticles: A Case Study of Indium Tin Oxide**

by

James Sylvester Grundy

DISSERTATION

Presented to the Faculty of the Graduate School of
The University of Texas at Austin
in Partial Fulfillment
of the Requirements
for the Degree of

DOCTOR OF PHILOSOPHY

THE UNIVERSITY OF TEXAS AT AUSTIN

December 2018

To my wife, Katharine, for your love, support, and patience.

Acknowledgments

First, I am indebted to my supervisor, Professor Lynn Katz, for her guidance and support during my graduate studies. Her mentorship shaped me into the researcher and scholar I am today, and I am fortunate to have been a part of her research family for the past seven years. I thank her for the multitude of research and teaching opportunities, pushing me when I needed it, and for being a great friend and colleague while guiding me through the journey that is a PhD.

I would also like to thank the members of my dissertation committee. It was a pleasure to work closely with and learn from Professor Navid Saleh — without his enthusiasm and intellect, this project would not have been possible. Professor Mary Jo Kirisits has been a joy to work with and her suggestions helped me stay sane when microbes were not behaving. I thank Professor Delia Milliron for productive conversations on semiconductor theory and light-electron interactions, expanding my knowledge and guiding a portion of this work. Professor Desmond Lawler offered many useful discussions, insights, and suggestions related to experiments and writing, and I thank him for his advice over the years. I spent many long days learning the ropes of research in Professor Danny Reible's lab in my first few years of graduate school, and I thank him for continuing with me and serving on my PhD committee.

The community of the EWRE program was one of the reasons I chose to pursue graduate studies at UT, and it did not disappoint. From the open-door policy of many faculty and students to the weekly seminar and happy hour, the people of EWRE shaped a collaborative, inquisitive, and supportive environment that formed many friendships and was a major crutch during my PhD life. I thank Justin Davis, Bryant Chambers, and Erin

Berns for being my sounding boards during my PhD — such intellectual and supportive colleagues and friends will be hard to top. Christine Ngan deserves many thanks for bringing me up to speed on the ITO project, analytical techniques, and helping with data collection. I thank undergraduate assistants Jenny Hui and Jackie McMahon for helping with data collection on this and previous projects. I am also indebted to the many current and former students in the Katz, Saleh, and other research groups that worked alongside and assisted me during my PhD: Paul Bireta, Sam Brodfuehrer, Celina Dozier, Farith Diaz, Yeonjeong Ha, Joon Han, Soyoon Kum, Matt Landsman, Aurore Mercelat, Sheik Nomaan, Cameron Oden, Trevor Williamson, Ki Yeo, Craig Ayers, Dipesh Das, Jaime Plazas-Tuttle, Stetson Rowles, Indu Venu Sabaraya, Anne Mikelonis, Sungmin Youn, Tongren Zhu, and Tory Boyd, among others. I am also grateful for the many other friendships formed during my time at UT, which are too numerous to count.

I thank the staff that assisted with chemical analyses and maintaining equipment, namely, Riki Lugo and Charlie Perego of EWRE along with Drs. Karalee Jarvis, Hugo Celio, and Raluca Gearba-Dolocan of the Texas Materials Institute. I also thank Eric Sikma for assistance with BET measurements and Camila Saez of the Milliron research group for synthesizing and characterizing ITO nanoparticles that were used in this study.

Finally, I am grateful to my parents and family for their support, patience, and understanding during my graduate studies. I was also lucky to meet and marry my wonderful wife, Katharine Batlan, while in graduate school — I am not sure I would have finished without the support from her and her family.

Funding for this work was provided by the National Science Foundation (CBET-1511826). I would also like to thank other sources of funding during my PhD: The National Science Foundation (IGERT-0966298), Cockrell School of Engineering scholarships and General Engineering program, and numerous teaching assistantships.

Effect of Dopant Level on Environmental Behavior of Doped Nanoparticles: A Case Study of Indium Tin Oxide

by

James Sylvester Grundy, Ph.D.
The University of Texas at Austin, 2018

Supervisor: Lynn E. Katz

Novel engineered nanomaterials (ENMs) continue to be synthesized and adopted for commercial and industrial applications. Currently, the classes of ENMs utilized most in consumer products are metal oxides, metals, and carbonaceous materials. An emerging subset of metal oxide ENMs with potential in many applications are doped metal oxides, which are binary metal oxides (MO_x) with some amount of another element, metal or non metal, inserted into the crystal lattice. This research focused on the environmental fate and transport of a major doped metal oxide, indium tin oxide (ITO), that is currently widely produced for applications in electronics. Specifically, this dissertation investigated the particle stability, solubility, and production of reactive oxygen species (ROS) by ITO nanoparticles in aqueous systems.

The stability of ITO particles in electrolyte solutions and the effect of Sn level was investigated in a series of homoaggregation studies. In order to better compare colloidal stability, a novel method, called the TAA-logistic method, for estimating the critical coagulation concentration (CCC) from dynamic light scattering data was developed and

tested with experimental and literature data. Using the new method, particle aggregation kinetics were compared for a range of solution conditions including pH, electrolyte valency, ionic strength, and presence of natural organic matter (NOM). Aggregation kinetics were determined for a set of synthesized particles coated with PAA-PEO polymer and for a set of bare, commercially-obtained particles. Aggregation experiments indicated inclusion of Sn in In_2O_3 decreased the aqueous stability of the nanoparticle, largely due to decreases in the magnitude of surface charge. However, the surface charge and aqueous stability did not always trend linearly with Sn content, indicating other factors, such as the distribution of Sn within the ITO crystal, were also important. Lastly, Suwannee River aquatic natural organic matter (NOM) significantly increased the aqueous stability of ITO nanoparticles through charge reversal and electrostatic stabilization.

Dissolution of ITO in dilute, inert electrolyte was studied in batch and flow-through experiments. Slow dissolution kinetics were shown in both experimental configurations. Sn was not appreciably leached from ITO at either $\text{pH} = 4$ or $\text{pH} = 6$. Inclusion of Sn appeared to reduce In solubility relative to In_2O_3 at $\text{pH} = 6$ but increased In leaching at $\text{pH} = 4$. The discrepancy between dissolution behavior at the two pH values relative to the In_2O_3 end-member indicated more complex solubility than explained by simple ideal solid solution aqueous solution behavior.

Lastly, the electronic band structure of ITO was determined for multiple levels of Sn using ultraviolet photoelectron spectroscopy and UV-vis diffuse reflectance spectroscopy. Inclusion of tin resulted in an increase of the optical band gap and a shift of the conduction band minimum, Fermi level, and valence band maximum to more oxidizing potentials relative to un-doped In_2O_3 . From these findings, ITO would thermodynamically be able to produce hydroxyl radicals from water by photocatalysis under UVB irradiation, regardless of the level of Sn doping. However, the ITO with the highest

doping level investigated, which is the ITO currently produced commercially, was able to produce hydroxyl radicals under UVB illumination at a significantly faster rate than lesser- and un-doped ITO.

This study showed that numerous characteristics related to the transport, transformation, and toxicity of ITO nanoparticles in aqueous environmental matrices were affected by the amount of Sn in ITO. However, the behaviors exhibited by ITO were not easily predicted by simply considering ITO as a mixture of varying amounts of the In_2O_3 and SnO_2 end-members. Therefore, further study of the environmental fate and transport of a more extensive set of doped metal oxides is needed to develop more complex models for assessing the environmental fate and transport of doped metal oxides.

Table of Contents

Acknowledgments	v
Abstract	vii
List of Tables	xiii
List of Figures	xiv
Chapter 1. Introduction	1
1.1 Background and problem statement	1
1.2 Objectives	4
1.3 Dissertation structure	5
Chapter 2. A novel method for estimating critical coagulation concentration: The case of tin-doped indium oxide nanocrystals	7
2.1 Introduction	7
2.1.1 Discussion of current methods to determine the CCC	9
2.1.1.1 Experimental determination of W from DLS data	12
2.1.2 Determination of CCC from $W(C_s)$	16
2.2 Materials and methods	17
2.2.1 Experimental	17
2.2.2 Data analysis using TAA-logistic method	18
2.3 Results and discussion	20
2.3.1 Efficacy of TAA-logistic method for analysis of experimental data	20
2.3.2 TAA-logistic method applied to literature data	21
2.3.3 Implications for fate and transport in aquatic environments	30
Chapter 3. Aggregation of indium tin oxide nanoparticles in aqueous electrolyte solutions: Investigating the role of Sn doping	32
3.1 Introduction	32
3.2 Materials and methods	34
3.2.1 Commercial ITO nanopowder	34
3.2.1.1 Nanopowder characterization	34

3.2.1.2	Dispersion preparation	35
3.2.2	ITO nanoparticle synthesis and aqueous stabilization	36
3.2.2.1	Materials	36
3.2.2.2	Indium oxide and indium tin oxide nanoparticle synthesis	37
3.2.2.3	Characterization	37
3.2.3	Aggregation kinetics	37
3.2.4	Data analysis	39
3.3	Results and discussion	41
3.3.1	Nanoparticle characterization	41
3.3.1.1	TEM and XRD	42
3.3.1.2	Electrophoretic mobility	45
3.3.2	Aggregation	50
3.3.2.1	Effect of ligand presence	52
3.3.2.2	Effect of pH and Sn level	54
3.3.2.3	Effect of counterion - Schulze Hardy rule	55
3.3.2.4	Effect of NOM	57
3.3.3	Environmental implications	62
Chapter 4.	Effect of tin dopant level on dissolution behavior and photo-generation of hydroxyl radicals by indium tin oxide nanoparticles	64
4.1	Introduction	64
4.2	Materials and methods	67
4.2.1	Materials	67
4.2.2	ITO dispersion preparation	67
4.2.3	Dissolution experiments	68
4.2.3.1	Batch dissolution experiment	68
4.2.3.2	Flow-through AFM dissolution experiment	70
4.2.4	Electronic band structure	72
4.2.4.1	X-ray and ultraviolet photoelectron spectroscopy	72
4.2.4.2	Diffuse reflectance UV-vis spectroscopy	74
4.2.5	Terephthalate hydroxyl probe test	75
4.3	Results and discussion	77
4.3.1	Batch dissolution	77
4.3.2	Dissolution monitored by flow-through AFM	83
4.3.3	Apparent optical band gap	87

4.3.4	Dry particle electron band energetics	87
4.3.5	Hydroxyl radical production	90
4.3.6	Environmental implications	95
Chapter 5.	Conclusions and recommendations	98
5.1	Conclusions	98
5.2	Environmental implications	100
5.3	Recommendations for future work	100
Appendix		103
Appendix A.	Appendix for Chapter 2	104
A.1	Discussion of W relating to DLS measurements	104
A.2	Discussion of CCC	105
Bibliography		108
Vita		127

List of Tables

1.1	Important properties and parameters for investigating environmental behavior of ENMs	2
2.1	Summary of methods to determine W from colloidal aggregation monitored by DLS and methods for subsequent CCC determination.	10
3.1	Characteristics of commercial and synthesized ITO nanoparticles used in aqueous stability experiments.	42
3.2	Parameters varied in particle aggregation experiments and associated CCC estimates	51

List of Figures

2.1	Simulated examples of time evolution of apparent hydrodynamic radii that may be encountered when monitoring particle aggregation with DLS	13
2.2	TAA-logistic method to estimate CCC applied to experimental data with moderate diffusion-limited aggregation rate	22
2.3	TAA-logistic method to estimate CCC applied to fullerene aggregation data from literature with low diffusion-limited aggregation rate.	23
2.4	TAA-logistic method to estimate CCC applied to humic particle aggregation data from literature with high diffusion-limited aggregation rate . .	25
2.5	Estimation of CCC when the TAA-logistic method shows a time dependence of the estimated CCC	27
2.6	Comparison of efficacy of TAA-logistic method across range of experimental conditions of experimental and literature data	28
3.1	Scanning TEM images of synthesized ITO nanoparticles	43
3.2	TEM images and XRD spectra of commercial ITO nanoparticles	44
3.3	Elemental TEM-EDX map of commercial ITO	46
3.4	Electrophoretic mobilities of commercial ITO nanoparticles	47
3.5	Zeta-potential of synthesized ITO particles at pH \approx 5.7 and in the presence of CaCl ₂	50
3.6	Aqueous stability of polymer-capped synthesized ITO in CaCl ₂	53
3.7	Aqueous stability of bare commercial ITO at pH = 6.0, 7.0, and 7.9	56
3.8	Comparison of aqueous stability of bare ITO in NaNO ₃ and Na ₂ SO ₄	58
3.9	Aqueous stability of commercial ITO in the presence of NOM in NaNO ₃ and Ca(NO ₃) ₂	60
4.1	Aqueous Sn concentrations in batch dissolution experiment	78
4.2	Dissolved In concentrations over time in batch experiment	80
4.3	Aqueous In concentration in batch experiment relative to In(OH) _{3(s)} solubility	81
4.4	AFM height images of 5% ITO in flow-through dissolution experiment . .	84
4.5	Change in particle height in flow-through dissolution experiment	86
4.6	Total reflectance and Tauc plots of Kubelka-Munk transformation to determine optical bandgap	88
4.7	Estimated electronic band structure of commercial ITO	90

4.8	Dependence of hydroxyl radical production rate of initial terephthalic acid concentration	92
4.9	Time evolution of TPOH fluorescence after UVB irradiation of suspensions of ITO and TPA	94
4.10	Relative photogeneration rates of hydroxyl radical production	96
A.1	Accuracy and relative uncertainty of linear interpolation and tangent methods for estimating CCC from example experimental W from literature . .	107

Chapter 1

Introduction

1.1 Background and problem statement

Engineered nanomaterials (ENMs) are being increasingly incorporated into consumer products,^{1,2} enhancing the potential for ENMs to inadvertently enter aquatic environmental systems during their life cycles. In addition to estimating potential releases, the transport mechanisms and transformation of ENMs in the environment need to be understood to deduce possible exposure routes and estimate ecological and human health risks.³⁻⁵ Much research has focused on environmental behaviors of ENMs already on the market, including noble metal nanoparticles (e.g., nano-Ag), metal oxide nanoparticles (e.g., TiO₂ and ZnO), and carbonaceous materials (e.g., fullerene and carbon nanotubes).⁶ However, continual development of novel ENMs, such as nanohybrids and other mixed ENMs, presents a challenge for researchers assessing potential risk from ENMs to keep up with the pace of development.^{7,8}

One such class of ENMs with many potential applications are doped metal oxides. Doped metal oxides are binary metal oxides, e.g., TiO₂, In₂O₃, and CuO, that have some amount of another element inserted into the crystal, e.g., N-TiO₂, In_aSn_bO, and Cu_aFe_bO, and are produced for their unique properties that are often distinct from their binary end-members.⁹⁻¹¹ Many possible dopant-metal oxide combinations can be produced, and the level of dopant can also be controlled, resulting in a huge number of unique doped metal oxide materials. Although this class of ENMs has a promising future in many products, surprisingly little research into the behavior of doped metal oxides in

aquatic systems and associated ecological and human health risks has been done.

The risk associated with nanoparticles in aqueous environments is often characterized by linking particle properties to physical/chemical and biological processes affecting fate and transport. For particle stability, surface charge, type of stabilizing ligand, and interaction of the particles with natural organic matter (NOM) have been shown to be major factors in assessing aggregation kinetics for a variety of ENMs. The type of stabilizing ligand has also been shown to affect dissolution kinetics for some nanoparticles, such as of nano-Ag.¹² Oxidative stress and membrane damage to pulmonary cells and *E. coli* from exposure to metal oxide nanoparticles has been correlated to the metal oxide electronic band structure,¹³ hydration enthalpy,¹⁴ and ability of the nanoparticle to photocatalyze reactive oxygen species (ROS).¹⁵ Thus, to investigate the environmental fate and transport of metal oxide ENMs, researchers can selectively assess properties of interest, such as those summarized in Table 1.1, that have been shown to be important for the environmental behaviors in question.

Table 1.1: Important properties and parameters for investigating environmental behavior of ENMs

Environmental behavior	Property	Experimental Parameter
Aggregation (Transport)	Particle stability, Homoa-ggregation	Critical coagulation concentration (CCC)
Dissolution (Transformation)	Solubility	Rate of ion release
Toxicity	Photocatalytic reactive oxygen species (ROS), disruption of cellular functions	Optical band gap ($E_{g,opt}$), conduction band minimum (E_{CBM})

To investigate whether doped metal oxides present an increased environmental threat relative to binary metal oxides, it is important to first determine how the environmental behaviors of doped metal oxides relate to that of their binary counterparts.

Specifically, researchers need to ascertain whether the environmental transport, transformation, and toxicity of doped metal oxides can be predicted by simply considering their composition or if other factors are also important. Previous research has shown doping of metal oxides can decrease particle stability in electrolyte solutions,¹⁶ both decrease or increase dissolution rates,^{16–22} and change the band gap energetics and associated toxicity.²³ With many studies demonstrating altered behavior of doped metal oxides from that of the primary un-doped end-member, it is prudent to investigate the environmental behaviors of existing, industrially-relevant doped metal oxide ENMs in order to determine whether these characteristics can be predicted from the composition of doped metal oxides in relation to their binary end-members.

A doped metal oxide that is currently produced in large quantities is indium tin oxide (ITO),²⁴ with the majority of ITO manufactured as nano-scale thin films. ITO has In_2O_3 crystal structure with isomorphic Sn(IV) substitution for In(III), and commercial ITO is currently produced by mixing 10:90 wt.%/wt.% SnO_2 : In_2O_3 and sintering to promote inclusion of Sn in the In_2O_3 lattice. Even though ITO is omnipresent in the consumer electronics industry, little study has been done regarding the fate, transport, and transformation of ITO in the environment. One study investigated the aqueous stability of 10 % Sn ITO nanoparticles in the presence of latex particles,²⁵ but no systematic study of how tin dopant percentage affects aggregation behavior of ITO nanoparticles has been done. Previous research has demonstrated preferential release of In(III) from ITO at low pH²⁶ and in the presence of organic acids,^{27,28} conditions common to deep-lung and gastric environments.²⁹ However, a systematic study on the effect of inclusion of Sn in In_2O_3 has not been done. Both ITO particles and dissolved In(III) have been shown to cause toxicity in bacteria and other model organisms.^{30–32} ITO has also been shown to cause inflammatory pulmonary responses,³³ and occupational airborne exposure to

ITO nanopowders has resulted in premature death.³⁴ Additionally, oxidative stress and environmental toxicity caused by ITO has been demonstrated in model aquatic organisms *Hydra attenuata*³⁵ and zebrafish embryos (*Danio rerio*).³⁶ While toxicity has been demonstrated for ITO and other indium-containing compounds,^{37,38} SnO₂ is a relatively non-toxic material. Inclusion of Sn may change In reactivity toward dissolution and other modes of toxicity, but no studies have considered ITO toxicity as a function of the level of Sn doping. Thus, ITO offers an industrially-relevant doped metal oxide with which to examine how dopant level affects the environmental transport, transformation, and toxicity in relation to the binary metal oxide end-members.

1.2 Objectives

The main goal of this research is to assess whether doped metal oxide ENMs can be treated as mixtures of constituent binary metal oxides regarding the transport, transformation, and toxicity in environmental aqueous systems. This objective is evaluated by using nanoparticulate ITO as a model doped metal oxide and investigating the effect of the level of Sn doping on the environmental properties outlined in Table 1.1 compared to that of un-doped In₂O₃. Specifically, three characteristics of aqueous nanoparticle behavior as a function of Sn doping level are to be determined, as outlined in the following tasks. While the focus of this research was on ITO nanoparticles, the methodologies and findings may help guide studies regarding the aqueous behavior of other doped metal oxide nanoparticles or other hybrid ENMs, such as mixed chalcogenides.

Task 1: Effect of Sn level on electrolyte-induced homoaggregation

This task investigates the aqueous stability to aggregation of ITO with varying levels of Sn by estimating the critical coagulation concentration (CCC) of the particles

in various conditions. First, a novel method of estimating the CCC from dynamic light scattering (DLS) data is formulated in order to better compare stability among different experimental conditions. Then the effect of ligand, NOM, electrolyte type, and pH are investigated to elucidate the role Sn level plays in homoaggregation of ITO.

Task 2: Effect of Sn level on aqueous dissolution in inert electrolyte

Dissolution is an important behavior for both the transformation of ENMs in natural systems and possible routes of toxicity. The objective of this task is to see how the solubility of ITO in slightly acidic and near-neutral, inert electrolyte differs from that of the In_2O_3 and SnO_2 end-members that are used in ITO production.

Task 3: Modulation of band gap energetics

This task investigates the differences in electronic band structure of dry ITO nanoparticles with different Sn levels. It also determines the ability of illuminated suspensions of ITO to produce hydroxyl radicals. Previous research has identified these characteristics as strong predictors of toxicity of metal oxide nanoparticles, and this research examines the appropriateness of these metrics for doped metal oxides.

1.3 Dissertation structure

This dissertation is comprised of five chapters and an associated appendix. Chapter 1 covers the background, motivation, and objective of the research contained within this dissertation.

In Chapter 2, a novel method for estimating the CCC of colloidal aggregation is introduced. The strengths and drawbacks associated with traditional methods of estimating stability ratios and the CCC from experimental DLS data are discussed, highlighting

the need for improved protocols for assessing particle stability. The new method is tested on an experimental data set collected as part of this research in addition to two datasets from literature that cover a wide range of absolute aggregation rates that may be observed with DLS data.

Chapter 3 uses the new method outlined in Chapter 2 to investigate the trends in electrolyte-induced particle aggregation in relation to the Sn doping level in ITO. Characterization of both bare commercially-obtained and polymer-capped synthesized ITO nanoparticles is presented along with experimental methods for assessing particle aggregation using DLS. Particle aggregation is monitored in a variety of conditions to elucidate the role Sn level has on key aggregation parameters and whether aqueous stability of ITO particles can be predicted by considering characteristics of ITO end-members In_2O_3 and SnO_2 .

Chapter 4 experimentally investigates the effect of Sn level on two critical aspects related to particle transformation and toxicity in the environment — dissolution and electronic structure. Again, the predictability of these behaviors in relation to ITO composition is discussed.

Chapter 5 discusses major findings of this research with respect to the environmental fate, transport, and toxicity of ITO in addition to broader implications regarding fate, transport, and toxicity of ENMs in general. Avenues for future research regarding environmental fate and transport of ITO and other doped metal oxides are discussed.

Chapter 2

A novel method for estimating critical coagulation concentration: The case of tin-doped indium oxide nanocrystals

2.1 Introduction

The fate, transport, and bioavailability of particles in the environment has been studied for decades, as particles can enhance transport of contaminants of concern through adsorption or co-precipitation and even act as contaminants themselves.^{39–41} Beginning at the end of the last century and continuing to the present, research has focused on the concept of particle stability in natural aqueous systems because it is a critical aspect of determining how particles transport and where they will accumulate.^{4,42,43} Properties such as particle size, shape and charge impact both the particle stability and the rate of particle aggregation. Solution properties, such as ionic strength and composition, pH, and presence of NOM, also affect particle stability.^{6,44} The concentration of particles further influences the rate of aggregation, since a greater number of particles results in more collisions and a higher aggregation rate.⁴⁵ Under some conditions, which depend on both the particle and solution properties, particles could become extremely unstable and aggregate on contact with another particle. In other conditions, particles may exhibit strong resilience to aggregation due to electrostatic, steric, or some other stabilizing mechanism, and the rate of aggregation will be relatively low.^{46,47} Thus, methods used when researching particle stability need to be able to cover a wide range of aggregation rates to adequately characterize particle stability.

The field of particle stability has grown immensely with the increased appearance of engineered nanomaterials (ENMs) in consumer products,^{1,2} which inevitably are released to the environment during their lifetime. Much research has focused on stability of a variety of ENMs, each with unique particle characteristics. Nanohybrids and doped metal oxides are classes of ENMs with promising industrial outlook due to the ability to tune the constituent materials and dopant levels, respectively. This ability also results in altered particle behavior in environmental systems,^{7,16} and particle stability may, or may not, change when the makeup of nanohybrids are adjusted. In order to assess whether small changes in nanohybrids or doped metal oxides result in altered particle stability, precise determination of the stability is needed, as differences may be small but significant.

A measure of colloidal stability in quiescent systems that has been used extensively is the critical coagulation concentration (CCC).⁴⁸⁻⁵³ Generally, the CCC is regarded as the electrolyte concentration at which the limitation to particle aggregation shifts from fast diffusion-limitation to slower or non-aggregating reaction-limitation.^{45,54} The CCC is dependent on nanoparticle properties, such as shape, molecular makeup, size, and surface charge, as well as on solution characteristics, such as ionic composition, pH, and presence of natural organic matter.⁴⁴ The utility of the CCC lies in the ability to observe how the CCC changes when just one parameter is changed. Typically, the CCC of multiple different particle types or the same particle type with different characteristics (e.g., size or surface coating) are determined in a single electrolyte to compare relative stability and elucidate mechanisms of stability.

Determination of the CCC values for ENMs in a given aquatic environmental system, such as a riverine system, is critical for modeling their fate in natural aquatic environments. If the CCC is large compared to the ionic strength of the system of interest,

the ENMs are likely to stay suspended and transport farther from the source. Conversely, if the CCC is small compared to the ionic strength, the ENMs will preferentially aggregate into larger particles and thus will settle out of the water column faster. The small size of ENMs can complicate determination of the CCC, as many methods require a high particle number for adequate detection, which causes faster aggregation. The opposite problem can occur for large colloids – small particle numbers are needed to avoid saturating the instrument, and small aggregation rates are observed. Thus, experimental methods to estimate CCCs should be able to produce accurate and reliable results regardless of the rate of aggregation of the investigated particles.

Although the general definition of the CCC is well-accepted, the practical determination has varied widely in the literature.^{55–59} A common method is to find the stability ratio, W , or ratio of the fast, diffusion-limited aggregation to an observed aggregation rate under variation of a parameter (e.g., ionic strength). The stability is often reported in the environmental literature as the inverse stability ratio, W^{-1} , or the attachment efficiency, α .⁴⁸ Stability ratios are found for a range of values for a single parameter (e.g., many ionic strengths) and are used to estimate CCC values with a graphical method, called the tangent method, where lines are fit to the diffusion-limited and reaction-limited data points and the intersection taken as the CCC.^{48,50,51,55,57,60–62} Alternative methods to the tangent method are fitting the stability ratios to empirical equations^{59,63} or using the stability ratio to scale aggregation data onto a single master curve.^{58,64} Each method has its own strengths and limitations, which are summarized in Table 2.1.

2.1.1 Discussion of current methods to determine the CCC

Theoretical formulations of the kinetics of particle aggregation primarily rely on the Smoluchowski population balance equations,⁶⁵ while theories on the thermodynam-

Table 2.1: Summary of methods to determine W from colloidal aggregation monitored by DLS and methods for subsequent CCC determination.

Methods for determining W	Data used	Advantages	Disadvantages
Initial slope, linear fit ^{48,51,55,61}	\bar{R}_{DLS} $1.3\bar{R}_{DLS,0}$	\approx Ease of implementation	Small subset of data, susceptible to data variability
Initial slope, nonlinear fit ^{56,57}	Full or all data to $t = t_{trunc}$	Uses more of aggregation curve, making fit more robust to variability	Many t_{trunc} possible, slope variable unless intercept is fixed
Data scaling to master curve ^{58,64}	Full	W based on full aggregation behavior	Separate forms of $\bar{R}_{DLS}(t)$ for $W < 100$ and $W > 100$, more work to implement
Methods for determining CCC from W			
Tangent method ^{48,50,51,55,57,60-62}	W in RLA and DLA	Ease of implementation	May leave out W near CCC, large uncertainty in estimated CCC
Empirical fit ^{59,63}	All W	Less uncertainty in estimated value, use of full dataset	More work to implement, need assumption for form of $W(C_s)$

ics of aggregation are mainly based on DLVO theory.^{46,47} The stability ratio, W , originally derived by Fuchs for continuum diffusion and later adjusted for hydrodynamic interactions by Spielman⁶⁶ and Honig⁶⁷ and for experimental agreement by McGown and Parfitt,⁶⁸ links the kinetic and thermodynamic theories. Theoretical definitions of W ^{55,69} share a common form in Equation 2.1a, where k_{fast} and k_{obs} are observed diffusion-controlled and arbitrary particle aggregation rates, respectively, for a given experimental condition. Note that theoretical derivations of W assume an initially monodisperse suspension of spheres; the overall stability ratio W_T determined by commonly employed techniques, such as dynamic light scattering (DLS), is a weighted summation of individual W_{ij} and collision probabilities P_{ij} among primary particles of size a_i , a_j , and, depending on the system, can be greater than⁷⁰ or less than⁷¹ the theoretical monodisperse stability ratio. To avoid ambiguity, W in this manuscript refers only to experimentally-determined W .

$$W = \frac{k_{fast}}{k_{obs}} \quad (2.1a)$$

$$W = \frac{k_{fast}}{k_{11}} = \frac{\left[\frac{1}{\alpha \bar{R}_{DLS,0} N_0} \left(\frac{d\bar{R}_{DLS}}{dt} \right)_{t \rightarrow 0} \right]_{fast}}{\left[\frac{1}{\alpha \bar{R}_{DLS,0} N_0} \left(\frac{d\bar{R}_{DLS}}{dt} \right)_{t \rightarrow 0} \right]_{11}} = \frac{\left(\frac{d\bar{R}_{DLS}}{dt} \right)_{t \rightarrow 0, fast}}{\left(\frac{d\bar{R}_{DLS}}{dt} \right)_{t \rightarrow 0, obs}} \quad (2.1b)$$

To estimate W from DLS data, **Virden and Berg** used a solution to the Smoluchowski population balance equation for short times and initially monodisperse spherical particles in conjunction with optical theory of DLS to arrive at the oft-used Equation 2.1b.⁷² Here, N_0 is the initial particle number concentration (L^{-1}), $\bar{R}_{DLS,0}$ is the initial z-average hydrodynamic radius (\bar{R}_{DLS}) determined in the absence of electrolyte, α is a function of DLS operating conditions, and k_{11} refers to the observed aggregation rate

of monomers in a given experiment. In colloidal aggregation, the starting suspension is often not composed of monodisperse spheres, so k_{obs} is used in lieu of k_{11} . If the same particle stock (i.e., N_0 and $\bar{R}_{DLS,0}$ are constant) and DLS operating conditions (α is constant) are used to determine both k_{obs} and k_{fast} , then the equation is simplified and W can be calculated from the initial rates of growth of the hydrodynamic radii, shown in the rightmost expression in Equation 2.1b.

2.1.1.1 Experimental determination of W from DLS data

Exemplary aggregation data obtained by DLS are simulated in Figure 2.1. Each curve in Figure 2.1 has an absolute observed aggregation rate (k_{obs}) that is larger than the previous and may be encountered with different experimental conditions. For example, small nanoparticles ($d \ll \lambda_{DLS}$) fall within the Rayleigh scattering limit, meaning the scattering of the laser follows $I \propto d^6$. To gather a sufficient number of scattered photons to adequately characterize small particles, a high N_0 must be used, which increases the aggregation rate for a given electrolyte condition. This rapid aggregation may result in a curve such as shown in Figure 2.1d. Conversely, if conditions are such that N_0 is relatively low or aggregation is unfavorable (i.e., reaction-limited), one may gather a quasi-linear curve resembling that of Figure 2.1a. Curves 2.1b and 2.1c represent either intermediate values for N_0 or more favorable aggregation conditions for a given N_0 than 2.1a.

Typically, experiments to estimate the CCC of a colloid in a given condition are conducted by monitoring the aggregation history (Figure 2.1) after subjecting an aliquot of colloidal suspension to a change in an experimental parameter, such as electrolyte concentration or temperature, while other parameters are held constant. Experiments are performed over a range of the parameter of interest to generate a distribution of curves, some that appear diffusion-limited (i.e., a further change in parameter does not

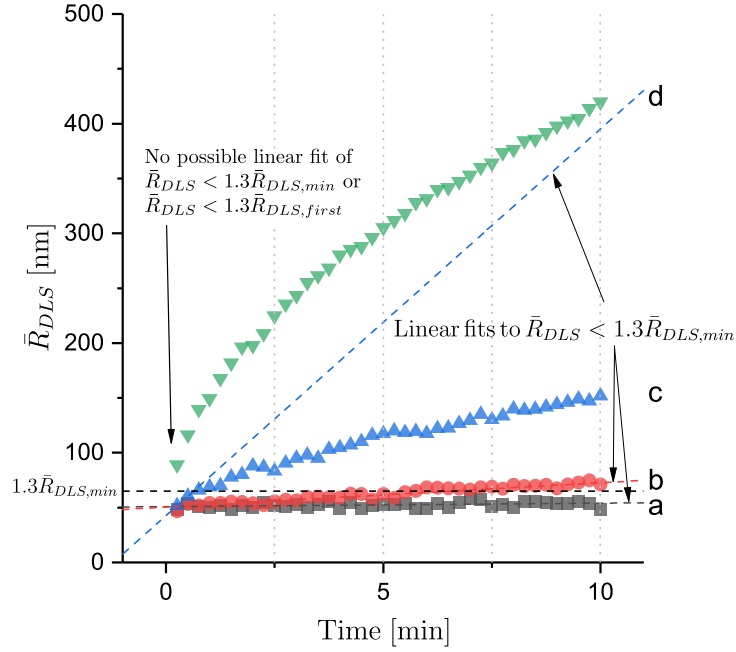


Figure 2.1: Simulated DLS data for different initial particle aggregation rates. Data were generated according to $\bar{R}_{DLS} = \bar{R}_{DLS,0} (1 + t/t_p)^z$, with $\bar{R}_{DLS,0} = 50$ nm and the following for each curve: (a) $t_p = 100$ min, $z = 0.7$, (b) $t_p = 10$ min, $z = 0.55$, (c) $t_p = 1$ min, $z = 0.46$, and (d) $t_p = 0.1$ min, $z = 0.46$, and random Gaussian noise with $\sigma_{DLS} = 2.5$ nm for all data points. Dashed lines signify the truncation radius for the linear fit to determine W (black) and the associated linear fits to the truncated data (colored). Vertical dashed lines indicate arbitrary times of truncation for cubic regressions of the data.

increase k_{obs}) and others that are reaction-limited (i.e., $k_{obs} < k_{obs,fast}$). A value for W is determined for each experimental condition, and the W values are then used to estimate the CCC. Determination of W from curves such as those shown in Figure 2.1 has been done using the following methods summarized in Table 2.1.

The linear-fit method is used widely, presumably due to ease of implementation. Linear fitting works well when the data variability is small and there are enough data points with $\bar{R}_{DLS} \lesssim 1.3\bar{R}_{DLS,0}$, which is the radius associated with complete transformation of singlets to doublets through aggregation. These criteria can be met when the dispersion is monodisperse, the integration time on the DLS is long, and the aggregation rate is slow relative to the integration time, much like that in Figure 2.1a and 2.1b. However, if the aggregation history has large variability and integration times do not adequately sample the particle size distribution, DLS may return \bar{R}_{DLS} further from the true mean \bar{R}_{DLS} . Generally, the data are truncated at $\bar{R}_{DLS} \approx 1.3\bar{R}_{DLS,0}$ and fit using linear least-squares regression to obtain $(d\bar{R}_{DLS}/dt)_{t \rightarrow 0}$ from the fitted slope parameter, which is then used in Equation 2.1b to calculate W . If there is significant variability in the data, there may be multiple time points that might appear acceptable for truncating the data. For example, in Figure 2.1b, $\bar{R}_{DLS} = 1.3\bar{R}_{DLS,0}$ at about $t_a = 5.5$ min, but dips below it again at about 7 min. A fit of the data truncated at the first crossing gives $k_{obs} = (2.21 \pm 0.30)$ nm/min, while a fit to the later truncation time gives $k_{obs} = (0.40 \pm 0.22)$ nm/min. Clearly, the choice of truncation time can significantly influence the determined value of W and all subsequent analyses involving W , such as determination of the CCC.

Another issue in using the linear-fit method arises when the aggregation rate is fast, such as shown in Figure 2.1c and 2.1d, which have two and zero points, respectively, that satisfy $\bar{R}_{DLS} < 1.3\bar{R}_{DLS,0}$. Some authors remedy this situation by instead truncating

the data at $\bar{R}_{DLS} \lesssim 1.3\bar{R}_{DLS,first,exp}$, where $\bar{R}_{DLS,first,exp}$ is the first or minimum point of the curve of interest. This method includes more data points, but undoubtedly results in a different slope than obtained when truncating to fewer points. A common issue associated with linear methods when aggregation is fast is the minimal amount of experimental data used to determine k_{obs} . If only a few data points are used and they display variability (i.e., due to polydispersity), confidence limits on the slope determined from a linear fit may be large.

To rectify this situation, the cubic-fit method for determining W has been used. In this method, the aggregation histories are fit with a spline or regressed with a low-order polynomial or other function. The slope of this function as $t_a \rightarrow 0$ is taken to be $(d\bar{R}_{DLS}/dt)_{t \rightarrow 0}$, analogous to the linear-fit method. However, this method also requires selecting a function to be used for fitting, as well as a decision regarding how much of the data to fit. For example, an ordinary least-squares cubic polynomial fit of each curve in Figure 2.1 was computed at 2.5 min, 5 min, 7.5 min, and 10 min, with each dataset truncated at those times. Looking again at curve b, the parameter fits for the slope as $t_a \rightarrow 0$ for truncation times listed above were nm min^{-1} , $(27.06 \pm 8.90)\text{nm min}^{-1}$, $(3.03 \pm 1.88)\text{nm min}^{-1}$, $(3.95 \pm 3.68)\text{nm min}^{-1}$, and $(2.29 \pm 1.15)\text{nm min}^{-1}$, respectively. Thus, estimates of W obtained from this method can also vary greatly by choice of truncation time and should be used with caution.

The third method to determine W , the scaling method, requires assumption of a functional form of $\bar{R}_{DLS}(t, W)$ and adjustment of W for each aggregation curve such that all curves align on a single master curve.^{58,64} This method is not explored in this study for reasons detailed in Appendix A.

2.1.2 Determination of CCC from $W(C_s)$

Once W for a colloid is determined as a function of the parameter of interest, such as the electrolyte concentration, C_s , the CCC can be determined for the system. Current methods are shown in Table 2.1. The most common practice for CCC determination is the tangent method, where a $\log W$ - $\log C_s$ plot is constructed, one line is fit to each the reaction-limited and diffusion-limited regimes, and the intersection of the line is taken as the CCC. This is a simple method and easily implemented, but has some limitations. First, the uncertainty of the point of intersection is rarely reported in literature, giving no precision to the determination of the CCC. Second, if any W data occur near the CCC, these points would not be included in the linear fits, effectively reducing the data set that was collected. Lastly, if the two lines are not properly fit using linear regression and the intersection found “by-eye”, the point of intersection could vary among analysts. Lastly, the fact that the data are transformed and a $\log W$ - $\log C_s$ plot is used increases the variability.

Another method that has been used, albeit relatively sparingly, is fitting experimentally-determined data to a functional form of $W(C_s)$.^{59,63} The advantage of this method is that all data points are used and data analysis software can yield consistent determination of the CCC with reported uncertainty. The functional form of $W(C_s)$ used can presumably affect the determined CCC; however, in the ranges of W often investigated by DLS, the effect is minimal. Example fits elucidating the advantage of fitting to a functional form of $W(C_s)$ and the issues associated with the tangent method are shown in Figure A.1.

Recently, another method was proposed to determine the CCC for a polydisperse system of natural colloidal particles.⁷³ Termed the total average aggregation (TAA) method, this routine determines the average aggregation rate, $\tilde{\nu}(t_a, C_s) = (\bar{R}_{DLS}(t_a) -$

$\bar{R}_{DLS,0})/t_a$, of each aggregation history of a given experimental condition. Then, each $\tilde{v}(C_s)$ is plotted versus C_s , and the tangent method is used to determine the CCC. Although W was not explicitly discussed in the development of the TAA method, approximations to W were made. This study takes advantages of these approximations to develop a new, robust method for estimating CCC. The new method, called the TAA-logistic method, may be more appropriate when determining the CCC over a wide range of absolute aggregation rates, such as for small (<10 nm) nanoparticles, or when comparing CCCs of similar magnitude, which may be the case for tuned nanohybrids or doped metal oxides. The efficacy of the TAA-logistic method was tested in this study using three distinct datasets, each including some data of particles with similar stability, while each exhibited different magnitudes of diffusion-limited absolute aggregation rate.

2.2 Materials and methods

2.2.1 Experimental

Indium tin oxide (ITO) nanopowders with primary particle size of $r_o \approx 50$ nm and 3 different tin levels, i.e., 100:0, 95:5, and 90:10 wt%:wt% In_2O_3 : SnO_2 (MKnano, Canada) were characterized as summarized in Chapter 3. To determine particle stability, the particles were each dispersed in Type 1 reagent water using bath sonication and subsequently centrifuged to select for the smallest cluster sizes. Electrolyte-induced aggregation of ITO nanoparticles was monitored with DLS, generally according to published methods,⁵³ since this technique is widely adopted in the environmental literature.^{48,50,55,62,74} One of the advantages of using DLS to monitor particle aggregation compared to other methods is the higher resolution of time, allowing the initial aggregation behavior to be observed under the optimal experimental conditions. For each experiment, an aliquot of ITO suspension was mixed with reagent water, a small amount of buffer, and electrolyte solution to arrive

at 1 mL total volume, $C_{\text{ITO}} = 25 \text{ mg L}^{-1}$, the desired pH (6, 7, or 8), and ionic strength, I . The time between mixing and the first DLS time point was recorded for each experiment. The DLS autocorrelation function was integrated every 15 s for a total of 900 s, and the detector was set at 90° . The intensity-weighted apparent hydrodynamic radius (\bar{R}_{DLS}) was determined using a second-order cumulant method using the manufacturer software. Replicate experiments were conducted and showed good reproducibility.

2.2.2 Data analysis using TAA-logistic method

In addition to experimental data generated by this study, the TAA-logistic data analysis method was tested on two datasets of electrolyte-induced aggregation from literature. The first dataset consisted of aggregation of four types of fullerenes (C_{60} , C_{70} , C_{76} , and C_{84}) that exhibited primary cluster diameters of 12 nm to 18 nm, hydrodynamic radii of $(57.6 \pm 2.1) \text{ nm}$, $(64.6 \pm 2.3) \text{ nm}$, $(76.6 \pm 2.8) \text{ nm}$, and $(73.20 \pm 1.94) \text{ nm}$, respectively, and electrophoretic mobilities in $1 \text{ mmol L}^{-1} \text{ NaCl}$ of $(-2.35 \pm 0.17) \times 10^{-8} \text{ m}^2 \text{ V}^{-1} \text{ s}^{-2}$, $(-2.76 \pm 0.09) \times 10^{-8} \text{ m}^2 \text{ V}^{-1} \text{ s}^{-2}$, $(-1.86 \pm 0.08) \times 10^{-8} \text{ m}^2 \text{ V}^{-1} \text{ s}^{-2}$, and $(-1.83 \pm 0.13) \times 10^{-8} \text{ m}^2 \text{ V}^{-1} \text{ s}^{-2}$, respectively.⁵³ The second data set consisted of naturally-occurring humus colloids extracted from soils in basic conditions. These particles exhibited a lognormal distribution of hydrodynamic diameter, with mode of 169.9 nm.⁷³ The surface charge density of these particles at pH = 7 was found to be $\sigma = -0.651 \text{ C m}^{-2}$.

To address previously-discussed limitations of determining $(d\bar{R}_{DLS}/dt)_{t \rightarrow 0}$ and use more of the data gathered in a single experiment, this method uses Equation 2.2, which is equivalent to $\tilde{\nu}_{max}(t)/\tilde{\nu}_{obs}(t)$ as outlined by Jia et al.⁷³ Note that Equation 2.2 uses

the definition of the derivative such that $\lim_{t \rightarrow 0} W_{\text{TAA}} = W$ as given in Equation 2.1b.

$$W_{\text{TAA}}(t) = \frac{\frac{\bar{R}_{DLS,max}(t) - \bar{R}_{DLS}(0)}{t - 0}}{\frac{\bar{R}_{DLS}(t) - \bar{R}_{DLS}(0)}{t - 0}} = \frac{\bar{R}_{DLS,max}(t) - \bar{R}_{DLS,0}}{\bar{R}_{DLS}(t) - \bar{R}_{DLS,0}} \quad (2.2)$$

To use Equation 2.2, each dataset was first truncated at an arbitrary $t = t_{trunc}$ for all aggregation histories investigating a given experimental condition and obvious outliers ($\bar{R}_{DLS}(t_{outlier})$ at least an order of magnitude greater than surrounding points) removed. To reduce the influence of variability in temporal measurements, each truncated aggregation curve was fit with a least-squares regression of a cubic polynomial. For aggregation curves at the same experimental conditions but differing C_s , $\bar{R}_{DLS}(t = t_{trunc}/2)$ of the fitted cubic polynomial was taken as the observed \bar{R}_{DLS} , since sampling the regression at $t = t_{trunc}/2$ ensures minimal uncertainty on the sampled value. Then, among all the curves for a given condition, $\bar{R}_{DLS,max}(t_{trunc}/2)$ is taken to be that observed in the fastest-aggregating curves, while $\bar{R}_{DLS,0}$ is taken from analysis of a non-aggregating aliquot, i.e., no added electrolyte. The sampled $\bar{R}_{DLS}(t_{trunc}/2)$ are used with these values in Equation 2.2 to determine W_{TAA} for each C_s to generate $W_{\text{TAA}}(t_{trunc}, C_s)$.

All CCC values reported in this paper were determined by fitting the experimentally-determined W (from either Equation 2.1b or 2.2 depending on method) to Equation 2.3a,^{59,63} where β and CCC are fitting parameters, using a Levenberg-Marquardt algorithm for non-linear regression as implemented in the package `minpack.lm` in R. Theoretical justifications for using this equation can be found in Appendix A. The effect of choice of t_{trunc} on the fitted CCC was explored by repeating this process for many t_{trunc} and plotting CCC vs. t_{trunc} . When used with Equation 2.2, Equation 2.3a was rearranged to produce Equation 2.3b, where $\bar{R}_{DLS,max}(t)$ and $\bar{R}_{DLS,min}(t)$ are additional fitting parameters. Note that $\bar{R}_{DLS,min}(t) = \bar{R}_{DLS,0}$ can be substituted if $\bar{R}_{DLS,0}$ is char-

acterized (i.e., \bar{R}_{DLS} determined with no added electrolyte), but they should match if an adequate number of aggregation histories are reaction-limited.

$$W^{-1} = \frac{1}{1 + \left(\frac{CCC}{C_s}\right)^\beta} \quad (2.3a)$$

$$\bar{R}_{DLS}(t) = \frac{\bar{R}_{DLS,max}(t) - \bar{R}_{DLS,min}(t)}{1 + \left(\frac{CCC_{TAA}}{C_s}\right)^\beta} + \bar{R}_{DLS,min}(t) \quad (2.3b)$$

2.3 Results and discussion

2.3.1 Efficacy of TAA-logistic method for analysis of experimental data

The methods outlined above to determine W_{TAA} and CCC_{TAA} from experimental DLS aggregation data were first used on the data generated in this study. Figure 2.2 shows the data fitting methodology in determining the CCC_{TAA} value (Figures 2.2a and 2.2b) as well as the confidence in estimating CCC as a function of truncation time (Figure 2.2c) for an exemplary data set. Briefly, Figure 2.2a depicts the aggregation history curves and associated cubic fit to $t = t_{trunc}$ for each ionic strength investigated. Figure 2.2b plots the values for $\bar{R}_{DLS}(t_{trunc}/2)$ for each ionic strength along with the estimated CCC and best-fit line of Equation 2.3b to the data. Figure 2.2c summarizes this process for multiple values of t_{trunc} along with estimates of the CCC using traditional slope-fitting methods. Note in Figure 2.2c (and Figures 2.3c, 2.4c, and 2.6), missing points or error bars indicate the estimated value or error was outside of the plotted range and not retained for clarity. In subsequent discussions regarding the efficacy of the proposed method, a method is considered to predict CCC with higher confidence (1) if the estimated CCC values match with the median estimates or (2) if the estimates show a clear trend over truncation time.

For this data set, the TAA-logistic method showed remarkable precision regardless of the choice of truncation time. Deviations at small times (when $t_{trunc} < 140$) are likely due to a low number of data points used in the cubic fit ($n = 6$) and the associated variability of the collected aggregation history. Agreement among the TAA-logistic method (for $t_{trunc} > 140$ s) and the two linear fit methods is observed, which indicates this method is likely both accurate and precise in determining the CCC for the given dataset. The variability of the CCC determined by the cubic fit method indicates that it is less reliable for these data.

2.3.2 TAA-logistic method applied to literature data

The applicability of this method and relative confidence in estimating CCC values was demonstrated by employing this method for literature-reported aggregation data on other types of colloids. The first data set investigated (Figure 2.3)⁵³ had experimental conditions such that k_{fast} was small relative to the experimental dataset from this study. This condition is manifested through the lower spread among aggregation curves at any given time, an example of which is shown in Figure 2.3a.

The cubic-fit method again exhibited high variability in the estimated CCC, indicating that is an unreliable method for this dataset as well. The TAA-logistic method for these aggregation histories showed relatively good agreement with the linear-fitting methods for $t_{trunc} < 500$ s. At $t_{trunc} > 500$ s, the uncertainty in the TAA-logistic method increased, and $CCC_{TAA} < CCC_{linear}$. At $t_{trunc} > 900$ s the TAA-logistic method resulted in $CCC_{TAA} \approx 0$. The reasons for these deviations and failures of the TAA-logistic method at higher t_{trunc} are likely two-fold. First, the aggregation history (Figure 2.3a) has many curves (seven) that exhibited diffusion-limited behavior (within experimental uncertainty), i.e., $k_{obs} \approx k_{fast}$, and only a small number (two) that exhibited reaction-

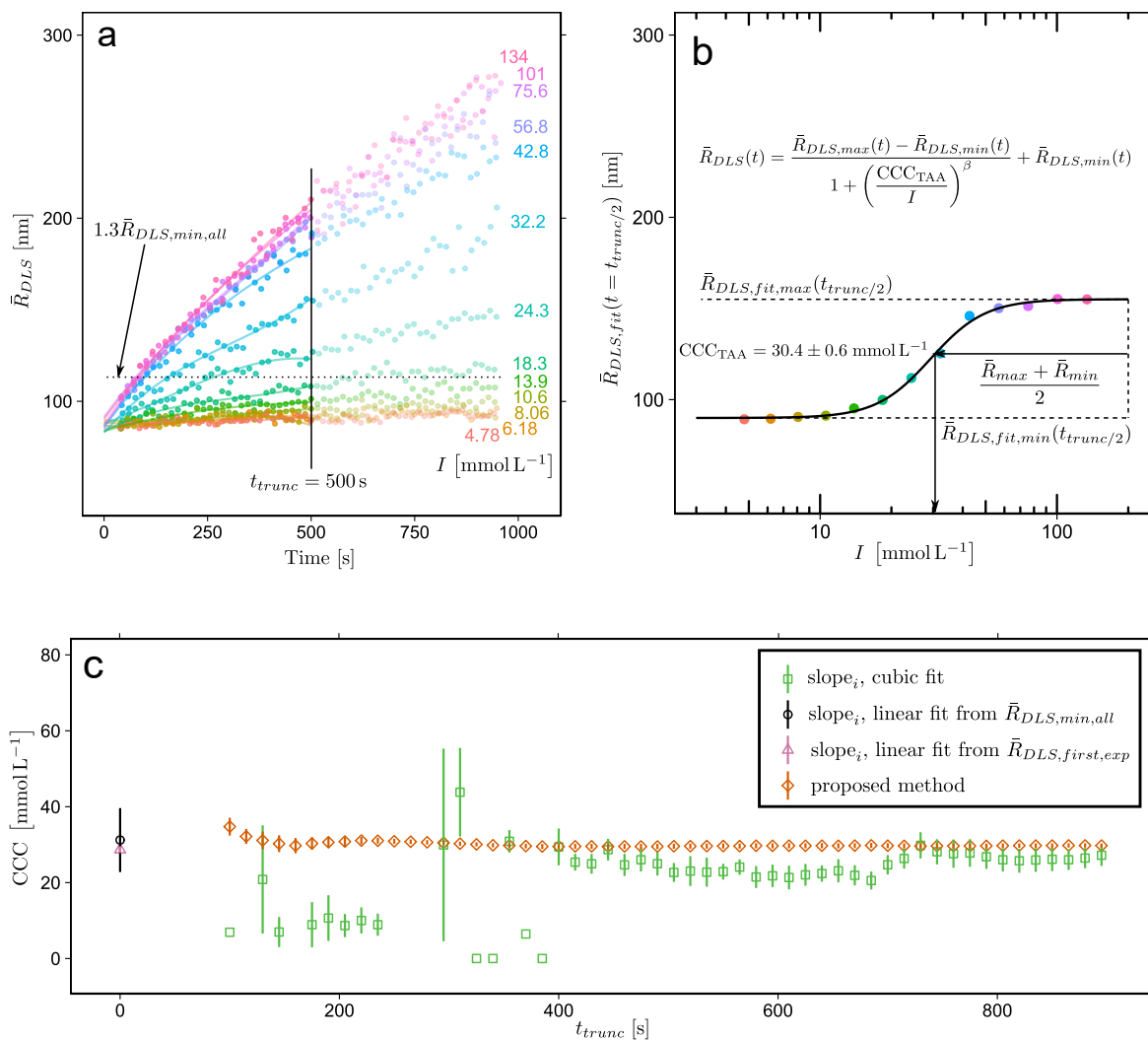


Figure 2.2: Use of TAA-logistic method to determine CCC on a dataset with the following experimental conditions: 0% ITO, $C_{ITO} = 25 \text{ mg L}^{-1}$, $\text{pH} = 7.0$ by addition of 1 mmol L^{-1} MOPSO buffer adjusted to $\text{pH} = 7.0$ with NaOH, and I adjusted through addition of NaNO_3 . (a) Aggregation histories for all ionic strengths tested with cubic fits to $t < t_{trunc}$ shown as colored solid lines. The values of $\bar{R}_{DLS}(t_{trunc}/2)$ for each curve are plotted in (b) versus I , and the fit to Equation 2.3b is plotted as the solid black line. (c) Comparison of CCC determined with the TAA-logistic method to previously used methods. Error bars are ± 1 standard error of the fit for CCC. Note that estimates for the CCC determined with linear fits are shown at $t_{trunc} = 0$ for clarity; these were not actually truncated at $t = 0$.

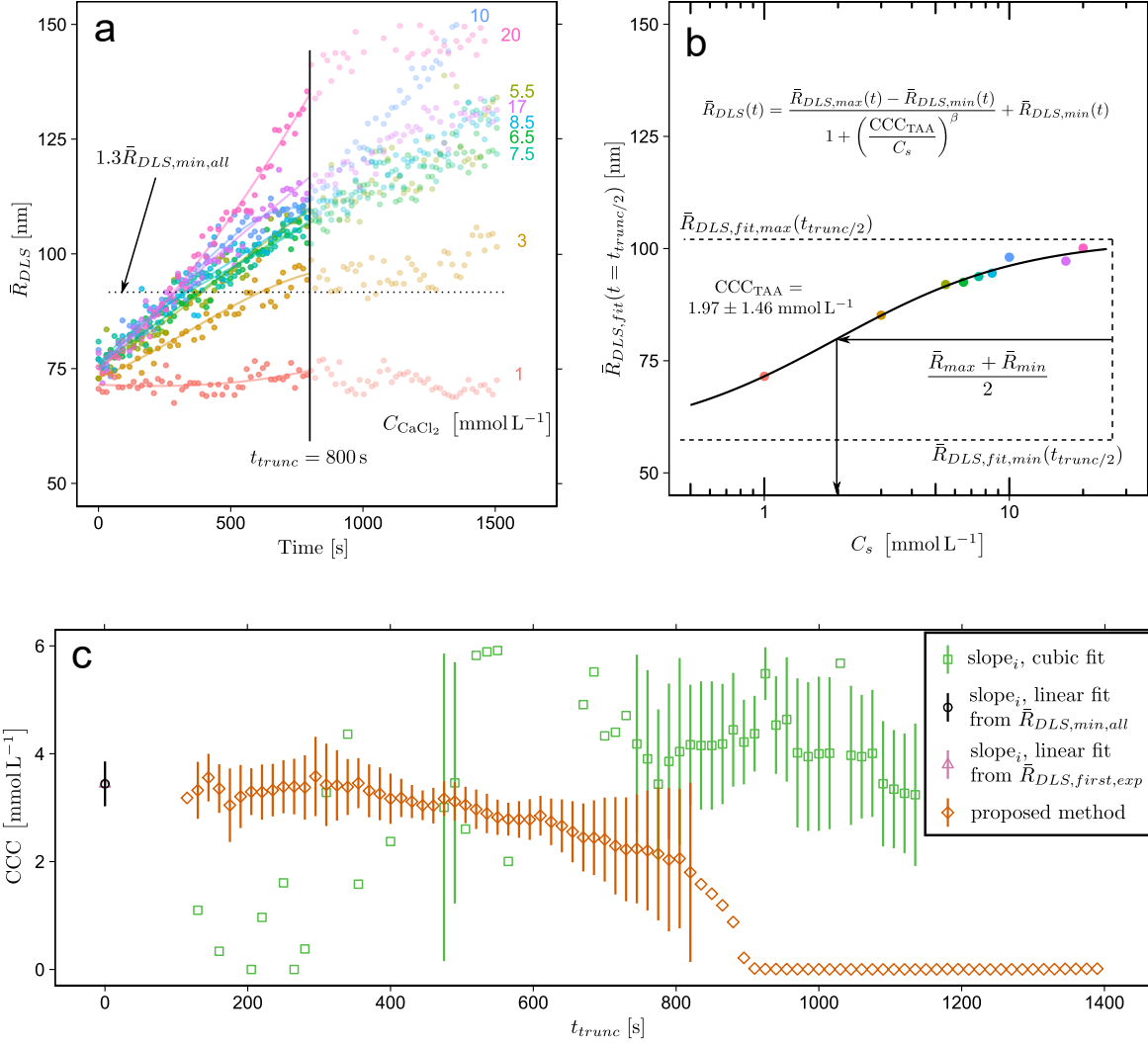


Figure 2.3: Use of TAA-logistic method to determine CCC on a dataset of nC₈₄ in CaCl₂⁵³ (a) Aggregation histories for electrolyte concentrations tested with cubic fits to $t < t_{trunc}$ shown as colored solid lines. The values of $\bar{R}_{DLS}(t_{trunc}/2)$ for each curve are plotted in (b) versus C_s , and the fit to Equation 2.3b is plotted as the solid black line. (c) Comparison of CCC determined with the TAA-logistic method to previously used methods. Error bars are ± 1 standard error of the fit for CCC. Note that estimates for the CCC determined with linear fits are shown at $t_{trunc} = 0$ for clarity; these were not actually truncated at $t = 0$. Also note the legend is not covering up any data points – the cubic-fit method resulted in estimated CCC that were out of the plotting range for at these t_{trunc} .

limited behavior, i.e., $k_{obs} < k_{fast}$. Determination of CCC values with higher confidence (and with Equation 2.3a) requires a number of aggregation history datasets (individual curves) on either side of the CCC and low variability among the determined W at the extremes, as shown in Figure 2.2b. Second, the variability in both the fast- and slow-aggregating curves (especially evident in the aggregation history for $C_s = 20 \text{ mmol L}^{-1}$ in Figure 2.3a) makes an accurate estimate of $\bar{R}_{DLS,fast}$ difficult. As $\bar{R}_{DLS,max}$ and $\bar{R}_{DLS,min}$ are important parameters when using Equation 2.3a, large uncertainties in these values can cause markedly different best-fit CCC_{TAA} values, as shown with this dataset. Thus, the TAA-logistic method had mixed results in data with low k_{fast} and results should be used cautiously. Ensuring an equal number of aggregation experiments on either side of the CCC for a given experimental condition improves method performance in low k_{fast} conditions.

A second dataset from literature was analyzed using TAA-logistic method.⁷³ The experimental conditions of this dataset were such that k_{fast} was large relative to the experimental dataset from this study, which is manifested in the large spread in values among curves in the aggregation history (Figure 2.4a). The linear-fit method to estimate the initial aggregation rate on data for $\bar{R}_{DLS} < 1.3\bar{R}_{DLS,0}$ could not be used on this dataset, as only one out of eight aggregation histories had any $\bar{R}_{DLS} < 1.3\bar{R}_{DLS,0}$.

The cubic-fit method showed much lower variability in this dataset, indicating it as a possible choice when analyzing data with a large k_{fast} . However, the TAA-logistic method showed much greater precision than the cubic-fit method even at low t_{trunc} , indicating superior performance. Interestingly, the CCC values estimated by both the TAA-logistic method and the cubic-fit method showed a strong dependence on truncation time, with smaller t_{trunc} resulting in higher estimates for the CCC than larger t_{trunc} . Recalling Equation 2.2, this is of no surprise, since W_{TAA} is defined using an average

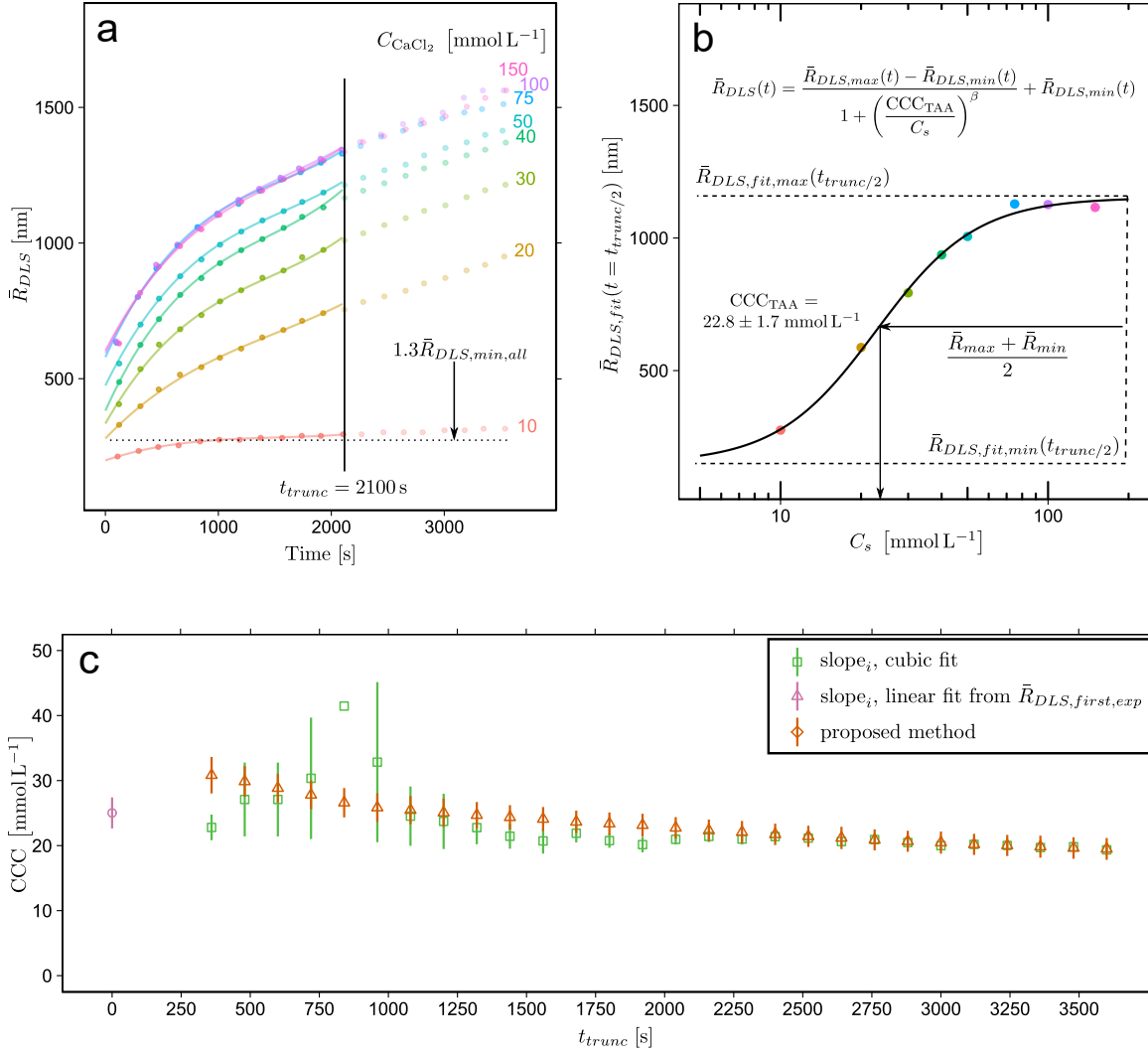


Figure 2.4: Use of TAA-logistic method to determine CCC on a dataset of natural humus colloids⁷³ in CaCl₂ at pH = 8(a) Aggregation histories for all electrolyte concentrations tested with cubic fits to $t < t_{trunc}$ shown as colored solid lines. The values of $\bar{R}_{DLS}(t_{trunc}/2)$ for each curve are plotted in (b) versus C_s , and the fit to Equation 2.3b is plotted as the solid black line. (c) Comparison of CCC determined with the TAA-logistic method to previously used methods. Error bars are ± 1 standard error of the fit for CCC. Note that the estimate for the CCC determined by linear fit is shown at $t_{trunc} = 0$ for clarity; data were not actually truncated at $t = 0$ for this method.

aggregation rate to an arbitrary time. When an aggregation curve has a rapidly changing slope, i.e., aggregation slows down, one would expect W_{TAA} calculated for long times to be less than W_{TAA} calculated at short times.

Although this time-dependence of W_{TAA} may seem problematic, it can be used for further analysis of quickly-aggregating systems to determine a better estimate of the CCC. In fast-aggregating systems, the W as defined in Equation 2.1b cannot be calculated accurately, as no data points are close to $\bar{R}_{\text{DLS},0}$. For a system exhibiting clear power-law behavior in the diffusion-limited aggregation histories, such as those in 2.4a, it can be shown that $W_{\text{TAA}}(t) = W_0 f(t, C_s)$, where W_0 is the W determined by the method of initial slopes (Equation 2.1b). The function $f(t)$ would differ for each C_s , so it is difficult to say exactly how the $f(t)$ would affect determination of the CCC by fitting to Equation 2.3a. However, the clear time-dependence of the CCC suggests that some functional form of $\text{CCC}_{\text{TAA}}(t) = \text{CCC}_0 g(t)$ exists. Thus, if one extrapolates the CCC determined by the TAA-logistic method to $t_{\text{trunc}} = 0$, the CCC_0 can be determined, as demonstrated in Figure 2.5. Using this method, the CCC_0 value for the data presented in Figure 2.4 is estimated to be $\text{CCC}_0 = (36.3 \pm 0.8) \text{ mmol L}^{-1}$, which is 45% greater than that estimated using the linear method ($(25.0 \pm 2.4) \text{ mmol L}^{-1}$). Although this may not be the true CCC value, it is likely a better estimate than previous methods when analyzing rapidly-aggregating data.

Figure 2.6 is a summary of the performance of the TAA-logistic method over all individual experimental conditions considered in this study. Columns 1 and 2 correspond to more of the dataset discussed in Figure 2.3, columns 3 and 4 to that discussed in Figure 2.2, and the final column to that discussed in Figure 2.4. Each plot corresponds to a distinct set of aggregation histories, and all experimentally-determined CCC have been normalized to the median CCC for a given experimental condition.

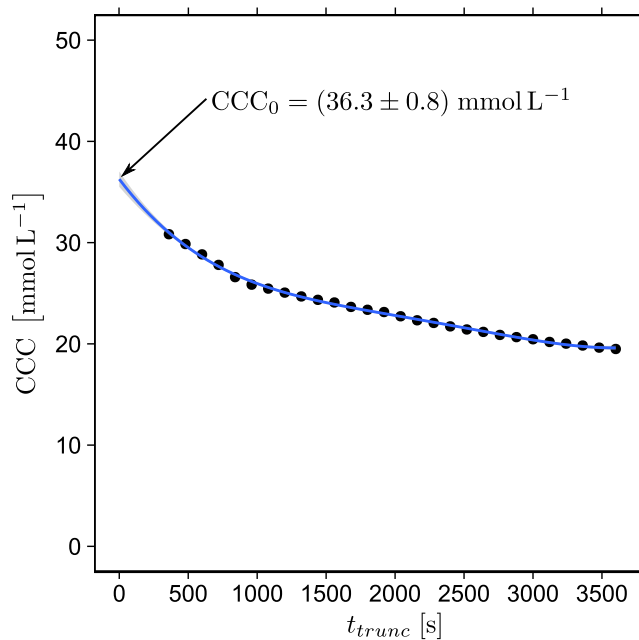


Figure 2.5: Example of more accurate determination of the CCC from $CCC_{TAA}(t_{trunc})$ for quickly-aggregating experimental conditions. All points were used in a quartic polynomial least squares regression, and the intercept at t_{trunc} is taken to be the true value of the CCC as would be determined by Equation 2.1b. Confidence intervals (95 %) are included but are mostly obscured by the best-fit line.

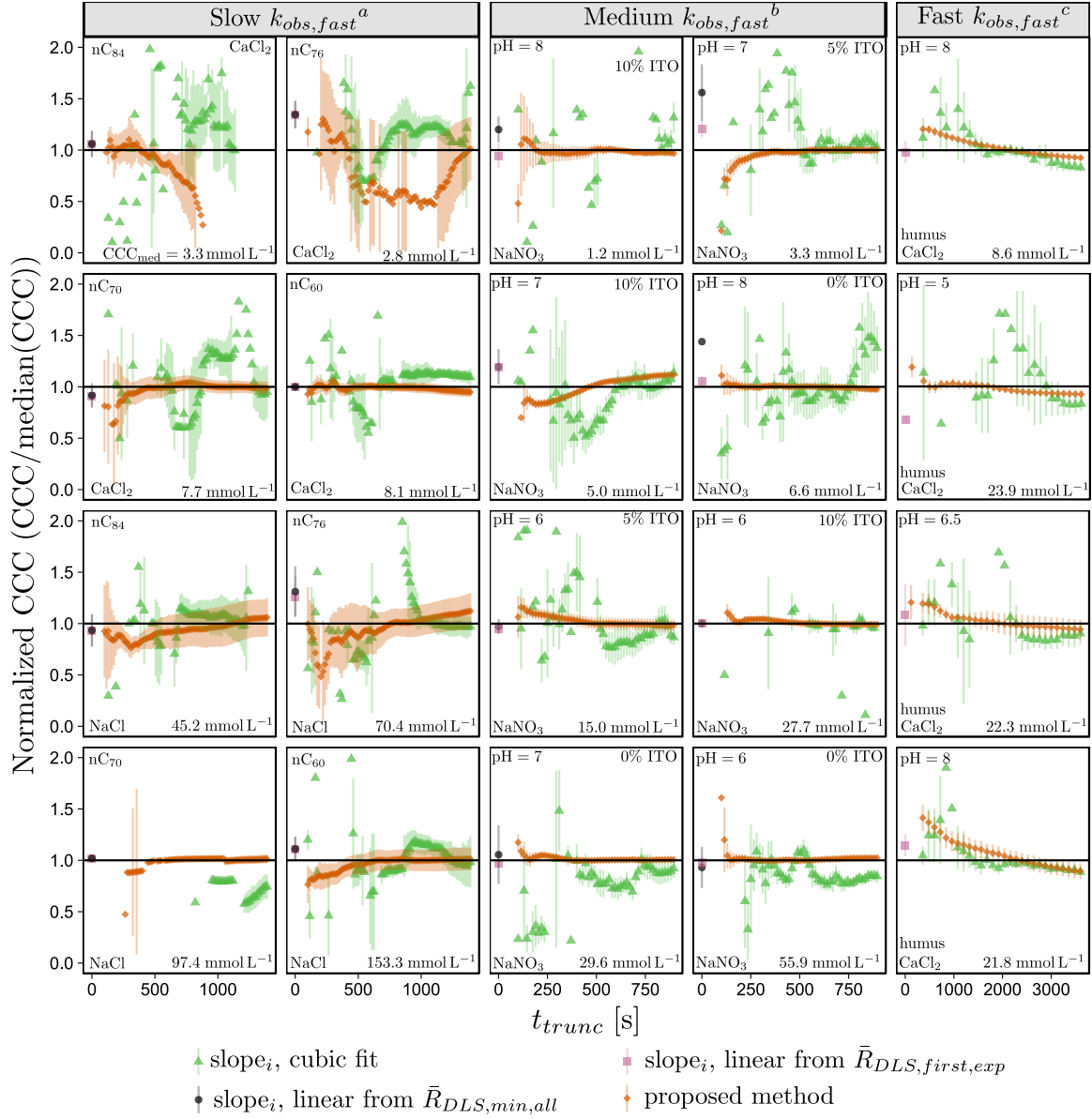


Figure 2.6

Figure 2.6: Comparison of efficacy of TAA-logistic method over a range of experimental conditions. Each plot corresponds to a single experimental condition. The value plotted on the ordinate is the CCC determined by a specific method at a truncation time of t_{trunc} normalized by the median CCC of all CCC determined by all methods for that experimental condition. The (a) first two columns are analyses of data from [Aich et al.](#), the (b) third and fourth column are analyses of data from this study, and the (c) final column are analyses of data from [Jia et al.](#). The median CCC determined for each experimental condition is included in each plot, and the median CCC generally decreases down the rows. Error bars are ± 1 standard error of the fit. Missing error bars indicate the error was greater than the plotting window, while missing points indicate the point was either outside of the plotting window or the fit of W to find the CCC failed due to data variability.

For the low k_{fast} dataset, the method had mixed results, with good results observed for the nC₆₀ and nC₇₀ experiments, but variable results found for the nC₇₆ and nC₈₄ experiments. Since no correlation seems to exist between the performance of the TAA-logistic method and magnitude of the CCC determined, the observed variability is likely due to issues discussed during the analysis of Figure 2.3.

Analysis of the dataset with a median value of k_{fast} mostly led to values of the CCC that were roughly the median CCC over a large range of t_{trunc} with high precision. Some variability at low t_{trunc} was observed, along with some time-dependence. However, overall, the TAA-logistic method performed remarkably well on this dataset, allowing for comparison among CCC with more certainty offered by the linear-fit or cubic-fit methods.

Every experimental condition of the final data set exhibited a dependence of estimated CCC on t_{trunc} , meaning the method outlined in Figure 2.5 could be used for a more accurate estimation. In all datasets investigated, the TAA-logistic method outperformed the cubic fit method, which showed great variability in estimated CCC as a function of t_{trunc} . The CCC estimated with the TAA-logistic method agreed with that found by the linear-fit method, within uncertainty) in about half of the experimental conditions. Thus, while the linear-fit method is the easiest to implement, using more of the aggregation history through use of the TAA-logistic method likely results in a more accurate determination of the CCC by reducing the influence of variability of the initial portion of the aggregation history.

2.3.3 Implications for fate and transport in aquatic environments

Accurate and precise determination of the CCC values of ENMs is vital for determining their fate and transport of aquatic systems. One class of ENMs that is of particular interest are doped metal oxides, which likely behave differently as the dopant

level changes. The CCC values of doped metal oxides in aqueous systems can be compared to determine relative stability and elucidate the effect of dopant level on aggregation, but previous methods to determine the CCC fail to provide the precision required for comparison when the CCC values are close. The new TAA-logistic method fills this gap, allowing for more accurate and precise determination of the CCC from DLS data obtained from a wide range of absolute aggregation rates.

Chapter 3

Aggregation of indium tin oxide nanoparticles in aqueous electrolyte solutions: Investigating the role of Sn doping

3.1 Introduction

Research of particle stability has a long and rich history owing to the importance of either stabilizing or destabilizing particles in many industrial processes. Understanding how particles nucleate and grow, and the factors controlling particle destabilization, is key to efficiently removing natural colloids, including pathogens, from drinking water sources. Conversely, keeping particles stabilized in suspension is a major focus of paint manufacturers. Over the past two decades, production of engineered nanomaterials (ENM) has steadily increased, resulting in a host of new colloids with various compositions, morphologies, surface modifications, and other characteristics.^{1,2}

The environmental fate of the vast array of new nanomaterials being researched and produced often begins with determination of the stability of the ENMs in natural waters. If released to surface waters, ENMs with high stabilities can travel away from the source, whereas ENMs with low stability in natural waters will likely aggregate and settle out of the water column. Numerous studies⁶ have investigated aqueous stability of ENMs, including carbonaceous materials,^{48,53,75} metal oxides,^{43,76} and metallic nanoparticles,^{77,78} both in the presence and absence of natural organic matter (NOM), to determine the important aspects of ENM aggregation in natural aqueous systems. Characteristics that are important for particle and ENM aggregation are particle size,

particle material, surface charge, ionic strength, electrolyte type, and adsorbed molecules and macromolecules, such as NOM.^{6,44} Many of these properties are also functions of other properties. For example, the surface charge of particles in suspension changes with pH and the presence of specifically-adsorbing ions. In some cases, aggregation of ENMs has been shown to follow the classic Derjaguin, Landau, Verwey, and Overbeek (DLVO) theory of colloidal aggregation; in others, additional factors, such as calcium bridging between adsorbed macromolecules,⁷⁵ are also important.

While the body of research on aqueous aggregation of ENMs continues to grow and theories on colloidal stability evolve, the production of new and novel ENMs continues to push the research even further. One emerging class of ENMs with wide-ranging applications is doped metal oxides. Incorporation of foreign elements into a metal oxide crystal structure can lead to unique properties neither the host nor dopant exhibit, and the expression of the properties can be a function of the amount of incorporated dopant. Prediction of aggregation behavior of doped metal oxides could therefore be quite complex, as changes in material properties like the Hamaker constant, surface charge, and how the surface interacts with inorganic and organic ligands and macromolecules all affect the aggregation behavior of ENMs. More research needs to be done to determine if, or how, aggregation of doped metal oxides can be predicted, as little study has been done in this area.¹⁶

This research examines the effect the dopant concentration has on aqueous stability of a doped metal oxide that is currently produced on a large scale. Indium tin oxide (ITO) is used in the electronics industry, largely as nano-scale thin film in LCD screens.⁷⁹ An estimated 700t of indium is produced annually and the majority used in ITO thin films,²⁴ placing ITO among the top 10 produced ENMs on a mass basis.¹ Unlike other highly-produced ENMs, such as TiO₂ and nano-silver, little study has been done regard-

ing the fate, transport, and transformation of ITO in the environment. Thus, this study elucidates the role the dopant level has on aggregation behavior of doped metal oxide nanoparticles while simultaneously determining an important aspect of environmental fate of a major ENM. Comparisons among aggregation behaviors of ITO nanoparticles in near-neutral electrolyte solution illuminate important changes to aggregation mechanisms as a function of tin doping levels and whether the changes can be predicted by considering the aggregation behavior of ITO end-members In_2O_3 and SnO_2 . Lastly, the effect of NOM on aggregation kinetics is investigated to simulate the transport of ITO nanoparticles following a release to surface waters. These behaviors will dictate the fate, transport and ultimately the toxicity of ITO nanoparticles in aqueous environmental systems.

3.2 Materials and methods

Materials and methods are split into those used for synthesized ITO particles and those used for commercially-obtained ITO nanopowders. Any differences in methods between the two ITO types are highlighted in subsequent subsections.

3.2.1 Commercial ITO nanopowder

3.2.1.1 Nanopowder characterization

ITO nanopowders with nominal primary particle diameter of $a = 50$ nm and 3 different tin levels, i.e., 100:0, 95:5, and 90:10 wt%:wt% In_2O_3 : SnO_2 (MKnano, Canada), were characterized for crystallinity with x-ray diffraction (XRD; Rigaku R-Axis Spider). A 40 kV Cu $K\alpha$ radiation source was utilized, and diffraction data collected as the sample was rotated on the ϕ axis at a rate of 1°s^{-1} for 10 min at room temperature (293 K). To determine tin content, aliquots of 500 mg L^{-1} dispersions were digested with concen-

trated, trace metal grade HNO_3 (Fisher Scientific) in 50 mL polypropylene centrifuge tubes for approximately 72 h. Aliquots of the digests were then diluted to 2% v/v HNO_3 and concentrations of In and Sn were determined using ICP-OES. Specific surface areas were analyzed by BET N_2 isotherms at 77 K after activating the powders at 70 °C under vacuum overnight (Quantachrome Autosorb-iQ). JEOL 2010F Transmission electron microscopy was performed on a JEOL 2010F in high-resolution and backscatter modes with energy disperse x-ray spectroscopy (EDX) for elemental mapping. For TEM imaging, particles were ultrasonically dispersed in reagent water and diluted into HPLC-grade ethanol (Fisher), which was then dropcast on carbon-coated mesh TEM grids and allowed to dry at room temperature.

Electrophoretic mobility (EPM) of suspended particles were determined using MP-PALS (Wyatt Möbiu ζ , Santa Barbara, CA). Aliquots of the desired ITO suspension were added to buffered electrolyte solution in base-leached polypropylene vials to match conditions present in the aggregation experiments (i.e., pH, ionic strength, and particle mass concentration). To determine approximate isoelectric points (IEP) of the particles, unbuffered electrolyte solution was bubbled with N_2 to remove carbon dioxide, an aliquot of ITO suspension added, and the pH adjusted with appropriate amounts of HCl or NaOH. Final conditions were of $I = 5 \text{ mmol L}^{-1}$ and $C_{\text{ITO}} = 25 \text{ mg L}^{-1}$ for IEP determination. Injections into the Möbiu ζ were made with a polypropylene syringe to avoid silicate adsorption from glass during EPM measurements.⁸⁰

3.2.1.2 Dispersion preparation

A bath-sonication method was used to prepare aqueous suspensions instead of direct probe sonication due to evidence of release of negatively-charged tip particles during the sonication process,⁸¹ which could affect the aggregation behavior of ITO.

Approximately 10 mg of ITO nanoparticles were added to 5 mL reagent water in a 15 mL polypropylene centrifuge tube, which was then clamped vertically to a ringstand and the bottom of the vial placed near the base of the sonication bath (Branson CPX2800). Ice was added to the bath to keep the bath temperature below or near ambient temperature. The sonicator was run continuously at a setting of HI for 45 min. Following sonication, 7 mL of reagent water was added to the dispersion, which was then centrifuged with a swinging bucket rotor at 2000 RCF for 7 min to 10 min with acceleration and deceleration ramps settings of 0 (Eppendorf 5804 with A-4-44 rotor, Germany). From the centrifuged dispersion, 7 mL of supernatant was retained in an amber base-leached HDPE bottle to select the smallest aggregate sizes for future study. The sonication and centrifugation process was repeated with subsequent 10 min sonication times until an adequate volume of supernatant was retained for the desired experiments.

3.2.2 ITO nanoparticle synthesis and aqueous stabilization

3.2.2.1 Materials

All chemicals were used as received and without further purification. Indium acetate ($\text{In}(\text{ac})_3$, 99.99% trace metal basis), indium acetylacetonate ($\text{In}(\text{acac})_3$, >99.99% trace metal basis), tin (II) acetate ($\text{Sn}(\text{ac})_2$), tin (IV) bis(acetylacetonate)dichloride ($\text{Sn}(\text{acac})_2\text{Cl}_2$, 98%), oleylamine (technical grade, 70%), oleic acid (technical grade, 90%), N,N-dimethylformamide (ACS reagent, $\geq 99.8\%$), nitrosonium tetraborofluorate (95%), were purchased from Sigma Aldrich. Hexane (ACS reagent, various methylpentanes 4.2%, $\geq 98.5\%$), reagent alcohol (ethanol 88% to 91%, methanol 4.0% to 5.0%, isopropyl alcohol 4.5% to 5.5%), and toluene ($\geq 99.5\%$) were purchased from Fisher Scientific.

3.2.2.2 Indium oxide and indium tin oxide nanoparticle synthesis

Indium tin oxide nanocrystals were synthesized using a standard Schlenk line technique adapted from literature⁸² utilizing different ratios of $\text{In}(\text{ac})_3$ and $\text{Sn}(\text{ac})_2$ to arrive at uniformly-doped 8 % and 10 % (mole fraction) ITO nanocrystals. The oleylamine and oleic acid ligands were then stripped according to a procedure reported previously⁸³ and subsequently capped with a PAA-mPEO₄ random copolymer in pH = 9 borate buffer to make the nanocrystals dispersable in water. Indium oxide (0 % ITO) nanocrystals were synthesized following another Schlenk line technique reported in literature⁸⁴ and subsequently ligand-stripped and capped in the same fashion as the ITO crystals.

3.2.2.3 Characterization

Particle sizes and morphologies were determined with scanning TEM (STEM) on a Hitachi S5500 SEM/STEM. Nanocrystal solutions were dropcast on TEM grids (Pelco[®] ultrathin carbon-A 400 mesh grid, Ted Pella). Zeta potential (ZP) measurements of aqueous suspensions of synthesized nanoparticles were determined on a Malvern Zetasizer Nano ZS using folded-capillary cells. Different instrumentation was used for ZP determination of synthesized particles due to instrument availability. Aliquots of synthesized nanoparticles were added to electrolyte solution, mixed, added to the capillary cells, and the ZP determined for different electrolyte concentrations at pH \approx 5.7, matching the pH of aggregation experiments of synthesized nanoparticles.

3.2.3 Aggregation kinetics

Aggregation of ITO dispersions in electrolyte solutions were monitored by time-resolved dynamic light scattering (TR-DLS) using an ALV/CGS-3 goniometer with ALV-7004/USB multi-tau correlator (ALV, Langen/Hessen, Germany), split fiber-optic detec-

tion, and a 21 mW HeNe laser with a wavelength of $\lambda = 632.8$ nm (Model 1154P, Lumentum/JDSU, USA). Toluene was used as the index-matching fluid and was kept at $T = 25.0$ °C during the experiments with a Julabo F25 recirculating water bath with ME controller. Borosilicate glass culture tubes with 10 mm diameter (Cat. No. 14-961-25, Fisher Scientific, USA) were used as sample vials for all experiments. Prior to use in aggregation experiments, the vials were soaked in a 1 % Hellmanex II solution (Hellma GmbH, Germany) for at least 12 h, rinsed profusely with deionized water followed by Type 1 reagent water, and placed in a muffle furnace at 500 °C in ambient air for at least 16 h to remove any adsorbed organics. Only new sample tubes were cleaned and prepared in this fashion - used tubes were discarded after use to avoid possible sample carryover.

For experiments with synthesized ITO suspensions, secondary salt stock solutions were prepared by diluting either 5 mol L⁻¹ NaCl (Cat. No. 59222C, Sigma-Aldrich, USA) or 1 mol L⁻¹ CaCl₂ (Cat. No. C0478, Teknova, USA) with filtered reagent water to various concentrations. For commercial ITO suspensions, NaCl (99.998 %, Alfa Aesar), NaNO₃ (ACS grade, ≥ 99.0 %, Sigma-Aldrich), Ca(NO₃)₂ · 4 H₂O (99.995 %, Alfa Aesar), and Na₂SO₄ (99.9955 %) were dried overnight at 105 °C and dissolved in reagent water. Additionally, MES hydrate (≥ 99.4 %, Sigma-Aldrich), MOPSO (Sigma-Aldrich) and HEPES and Na-HEPES (Sigma-Aldrich) were separately dissolved in reagent water and pH values adjusted to 6.0, 7.0, and 7.9, respectively, with 2 N NaOH (Baker Analyzed grade, J.T. Baker) to result in 10 mmol L⁻¹ buffer stock solutions for pH-controlled experiments. For experiments involving NOM, aliquots of 125 mg L⁻¹ Suwannee River NOM stock solution were added to buffered electrolyte solution prior to addition of nanoparticles. The NOM stock used in this study was Suwannee River NOM (IHSS aquatic NOM 2R101N, isolated by reverse osmosis in 2012⁸⁵) dissolved in reagent water and passed

through a 0.45 μm filter before use. Suwannee River aquatic NOM was used to simulate a release of particles to surface waters since aquatic NOM includes all fractions of NOM present, including oft-used humic and fulvic acids.

To begin an experiment, aliquots of buffer, NOM, and electrolyte stocks were mixed in the pre-cleaned borosilicate sample tubes to the desired concentrations. Then, an aliquot of ITO dispersion supernatant was added to the solution to a final volume of 1.00 mL. The tube was then briefly vortexed to ensure well-mixed conditions and subsequently added to the index-matching bath of the goniometer. The TR-DLS run was started immediately. Scattering data were collected at a sample angle of $\theta = 90^\circ$ with automatic laser attenuation for 10 s to 30 s over a total period of 15 min to 60 min. The shorter collection times were used for fast aggregation to ensure the initial aggregation rate was captured. The experiments involving synthetic ITO suspensions were all run at ambient pH (~ 5.7), and the commercial ITO samples were run at the aforementioned buffered pH values with 0.1 mmol L^{-1} to 1.0 mmol L^{-1} buffer concentration.

3.2.4 Data analysis

Each autocorrelation function from TR-DLS was analyzed by the method of cumulants⁸⁶ using the ALV-Correlator Software version 3.0. The first cumulant from a second-order cumulant fit, $\bar{\Gamma}$, was used to determine the effective average diffusivity of the particles, $\bar{D}_{eff} = \bar{\Gamma}/q^2$, where $q = \frac{4\pi n}{\lambda} \sin\left(\frac{\theta}{2}\right)$, n is the refractive index of the solvent, and other variables are previously defined. The Stokes-Einstein relation was then used to calculate the intensity-weighted effective hydrodynamic radius, $\bar{R}_{DLS} = k_B T / (6\pi\eta\bar{D}_{eff})$, where $k_B = 1.381 \times 10^{-23} \text{ J K}^{-1}$ is the Boltzmann constant and η is the dynamic viscosity of the solvent. For high ionic strength suspensions, viscosity was corrected using an empirical model from literature.⁸⁷

The critical coagulation concentration (CCC) is a metric to determine relative stabilities of particles in electrolyte solutions. Qualitatively, the CCC is the electrolyte concentration at which the rate of particle aggregation switches from mass transfer limitation (when $I > \text{CCC}$) to reaction, or particle-sticking limitation (when $I < \text{CCC}$), where I is the ionic strength in mol L^{-1} . Quantitative definitions of the CCC rely on DLVO theory of colloidal stability. Historically, the CCC was said to occur at the electrolyte concentration such that repulsive energy is eliminated, which occurs when the maximum potential energy drops to zero, or $V_{\text{T}}(h) = V_{\text{EDL}}(h) + V_{\text{vdW}}(h) = 0$ and $dV_{\text{T}}/dh = 0$, where $V_{\text{EDL}} = f(h, I, a, \text{pH})$ is the repulsive interparticle force due to electrostatic double interaction and $V_{\text{vdW}} = f(h, a, A)$ is the attractive interparticle dispersion force. Here, h is the interparticle distance and A is the Hamaker constant for material attraction in fluid medium, which is largely determined by material properties and generally increases with material polarizability. Another definition that has been corroborated by experiments⁸⁸ is the electrolyte concentration that corresponds to an elimination of repulsive forces, which occurs when $dV_{\text{T}}/dh = 0$ and $d^2V_{\text{T}}/dh^2 = 0$.⁸⁹ Many particle aggregation systems, such as nanoparticles in natural waters, may need major corrections to classic DLVO theory, such as hydrophobicity, humic acid, or acid/base corrections, to find the CCC from experimental data.⁴⁴ Thus, this study opted for a simpler empirical approach, rooted in DLVO theory, to determine the CCC of particles under various conditions.

The TAA-logistic method, discussed in Chapter 2, for estimating the CCC was utilized. Briefly, $\overline{R}_{\text{DLS}}$ was monitored over time, which is subsequently referred to as an aggregation history, and a best-fit cubic line to the aggregation history was determined using a least-squares (for commercial ITO) or quantile (for synthesized ITO) regression. The quantile regression on the median was used when a large number of outliers (e.g., errant dust particles) were present, as quantile regression reduces the influence of these

outliers without explicitly excluding them.

For a given aggregation experiment, i.e., same ITO type over a range of electrolyte concentrations, a regression of the aggregation history for each electrolyte concentration was performed to an arbitrary truncation time, t_{trunc} , in order to estimate the hydrodynamic radius at any $t < t_{trunc}$. The fitted hydrodynamic radii at $t = t_{trunc}/2$, $\bar{R}_{DLS,fit}(t_{trunc}/2)$, was compared across electrolyte concentrations and were subsequently fit to the following equation

$$\bar{R}_{DLS,fit}(t_{trunc}/2) = \frac{\bar{R}_{DLS,fit,max}(t_{trunc}/2) - \bar{R}_{DLS,min}}{1 + \left(\frac{CCC}{I}\right)^\beta} + \bar{R}_{DLS,min} \quad (3.1)$$

where $\bar{R}_{DLS,fit,max}(t_{trunc}/2)$ is the maximum, diffusion-limited hydrodynamic radius obtained at that time, $\bar{R}_{DLS,min} = \bar{R}_{DLS,0}$ is the minimum hydrodynamic radius (i.e., what one would get with no added electrolyte), I is the ionic strength, and β is a fitting parameter. The inflection point of the fitted curve occurs when $I = CCC$. This process was repeated for many t_{trunc} to see if the determined CCC was a function of t_{trunc} ; if it appeared to be so, a higher-order polynomial was fit to $CCC(t_{trunc})$ and the intercept with the ordinate taken to be the more accurate estimate of the CCC.

3.3 Results and discussion

3.3.1 Nanoparticle characterization

Table 3.1 summarizes selected nanoparticle characteristics. Tin percentages are given in term of mole percentage of cation, or mol Sn/(mol Sn + mol In). The %Sn of the commercial samples as determined by TEM-EDX was higher than the nominal percentages for both the 5% and 10% ITO, whereas the %Sn as determined by ICP was considerably lower for the 10% ITO. As discussed in subsequent sections, this suggests

Table 3.1: Characteristics of commercial and synthesized ITO nanoparticles used in aqueous stability experiments.

Particle set	Nominal Sn (at%)	Sn (ICP) (at%)	Sn (EDX) (at%)	a (nm)	$R_{\text{DLS},0}$ (nm)	BET SSA ($\text{m}^2 \text{g}^{-1}$)
Commercial	0	0	0	50^a	80-100	10.
	4.8	4.2 ± 0.2	9.5	50^a	80-110	11
	9.3	6.6 ± 0.5	11.2	50^a	90-110	9
Synthesized	0	–	–	5.91 ± 0.42	~ 20	–
	8	–	–	6.06 ± 0.44	~ 50	–
	10	–	–	6.83 ± 0.59	~ 70	–

^a Nominal primary particle size from manufacturer and approximately confirmed with TEM images.

existence of crystalline SnO_2 phases, especially in the 10% ITO. SnO_2 is chemically resistant to dissolution by strong acids and HF, requiring high-temperature fusions with Na_2CO_3 and S to solubilize Sn for quantification. Thus, SnO_2 likely was not digested in concentrated HNO_3 , and the %Sn determined by ICP was attributed to Sn atoms incorporated into the ITO crystal. Lastly, for all ITO types, $R_{\text{DLS},0} > a$, indicating cluster formation during the respective dispersion processes.

3.3.1.1 TEM and XRD

STEM images of the synthesized samples are shown in Figure 3.1. Each particle type exhibited spherical morphology and monodisperse primary particle size of <10 nm. Size determinations are summarized in Table 3.1.

TEM images and X-ray diffraction patterns for each commercial ITO are shown in Figure 3.2. The particles had roughly the same size and morphology, showing spherical to cubic character. The main features of the XRD diffraction patterns for 0%, 5%, and 10% ITO indicated a cubic (bixbyite) structure (space group $Ia\bar{3}$) matching well with that of crystalline I_2O_3 (PDF No. 01-071-2194, ICDD). Additionally, the diffraction pattern for 10% ITO, and the 5% ITO to a lesser degree, included small peaks that matched

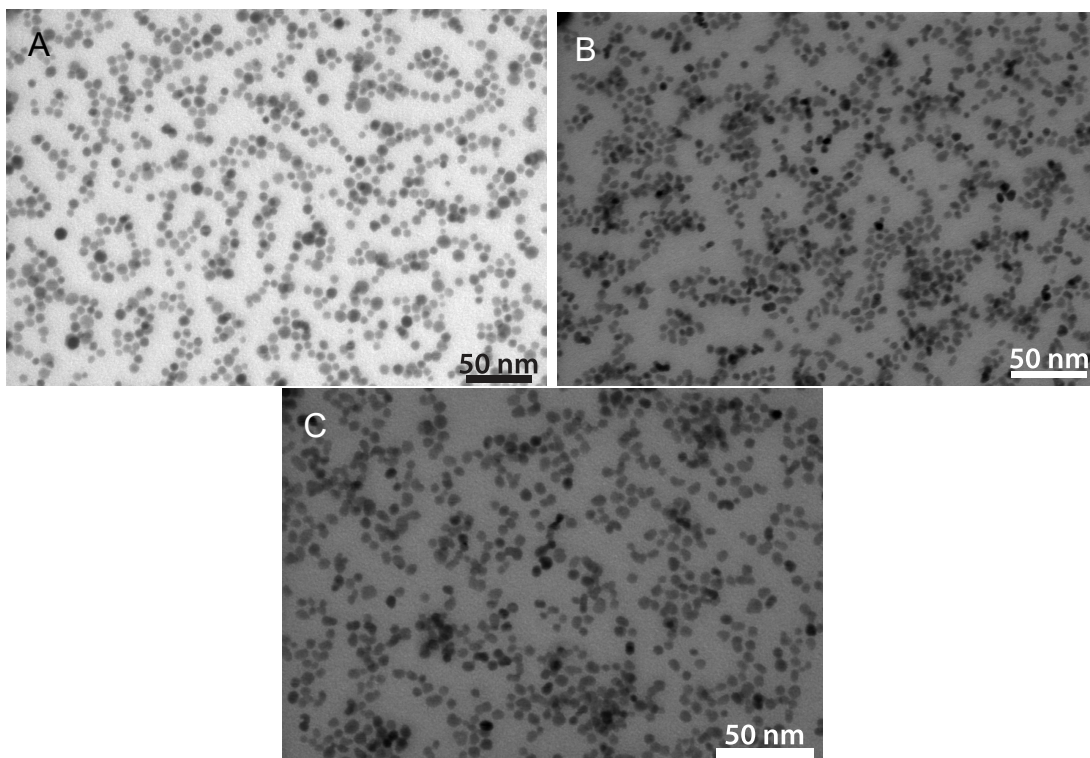


Figure 3.1: Scanning TEM images of synthesized (a) In_2O_3 (0% ITO), (b) 8% ITO, and (c) 10% ITO.

well with the crystal structure of tetragonal cassiterite SnO_2 (PDF 01-027-1147, ICDD), indicating the presence of either distinct particles of SnO_2 or heterogeneity within the 10% ITO nanoparticles.

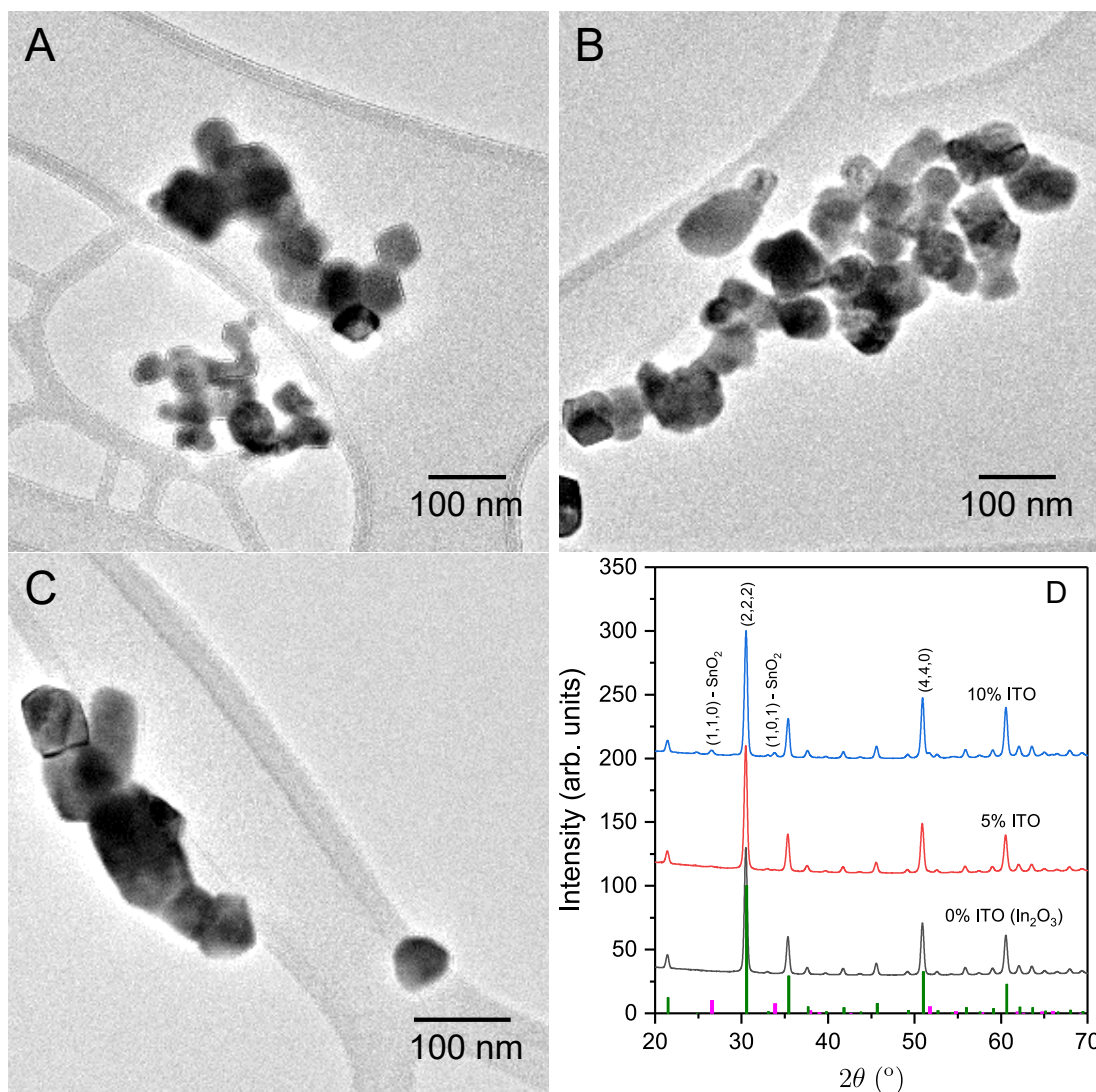


Figure 3.2: TEM images of (a) 0%, (b) 5%, and (c) 10% ITO. XRD spectra of all 3 powders are shown in (d). The bars on the ordinate correspond to XRD peak locations and relative intensities for In_2O_3 (taller, green bars) and SnO_2 (shorter, magenta bars).

EDX spectra from HRTEM were used to investigate the location of the SnO_2 crystal structure detected in XRD. No Sn was detected in EDX spectra for the 0% ITO,

corroborating the XRD pattern showing a single In_2O_3 bixbyite phase present. Atomic EDX maps for 5 % (left) and 10 % ITO (right) are shown in Figure 3.3. In both the 5 % and 10 % ITO, areas of inhomogeneous Sn incorporation can be seen, as evidenced by red patches in the cluster of primary particles (top plots). Zoomed-in maps (bottom plots) confirmed the islands were distinct SnO_2 primary particles and not heterogeneities within ITO crystals. Determination of distinct SnO_2 crystal structure within the ITO crystal structure was not possible due to the polycrystalline nature of the ITO particles. The atomic percentages of the clusters determined by EDX were 9.5 %:90.5 % Sn:In at% for the 5 % ITO and 11.2 %:88.8 % Sn:In at% for the 10 % ITO.

The presence of distinct SnO_2 , confirmed with both XRD and TEM-EDX, may be due to preparation method for the commercial ITO and the solubility of SnO_2 in In_2O_3 . Studies on the effect of sintering temperature on end-member crystallography found that crystals of ITO and SnO_2 would be present for sintering temperatures of $T < 1325^\circ\text{C}$ and $X_{\text{Sn}} > 4.5\%$ to 5%.^{90,91} Lower temperatures and shorter sintering times resulted in smaller metastable ITO crystals with higher Sn content, but SnO_2 was nearly always present when Sn was added above thermodynamic equilibrium of $X_{\text{Sn}} > 4.5\%$ to 5%.⁹¹ Further analyses of the commercial ITO in this study will continue to refer to the powders as 0 %, 5 %, and 10 % ITO, and implications of free SnO_2 crystals will be discussed.

3.3.1.2 Electrophoretic mobility

Electrophoretic mobility is a measure of the velocity of a particle or macromolecule in an applied external electric field and is an indirect measure of the surface charge of the particle. All the commercial ITO suspensions exhibited positive electrophoretic mobilities at $\text{pH} = 6.0$, as shown in Figure 3.4a, meaning they were positively charged at this pH . The 10 % ITO had an isoelectric point of $\text{pH}_{\text{IEP}} \approx 9.3$, shown as the pH at which the

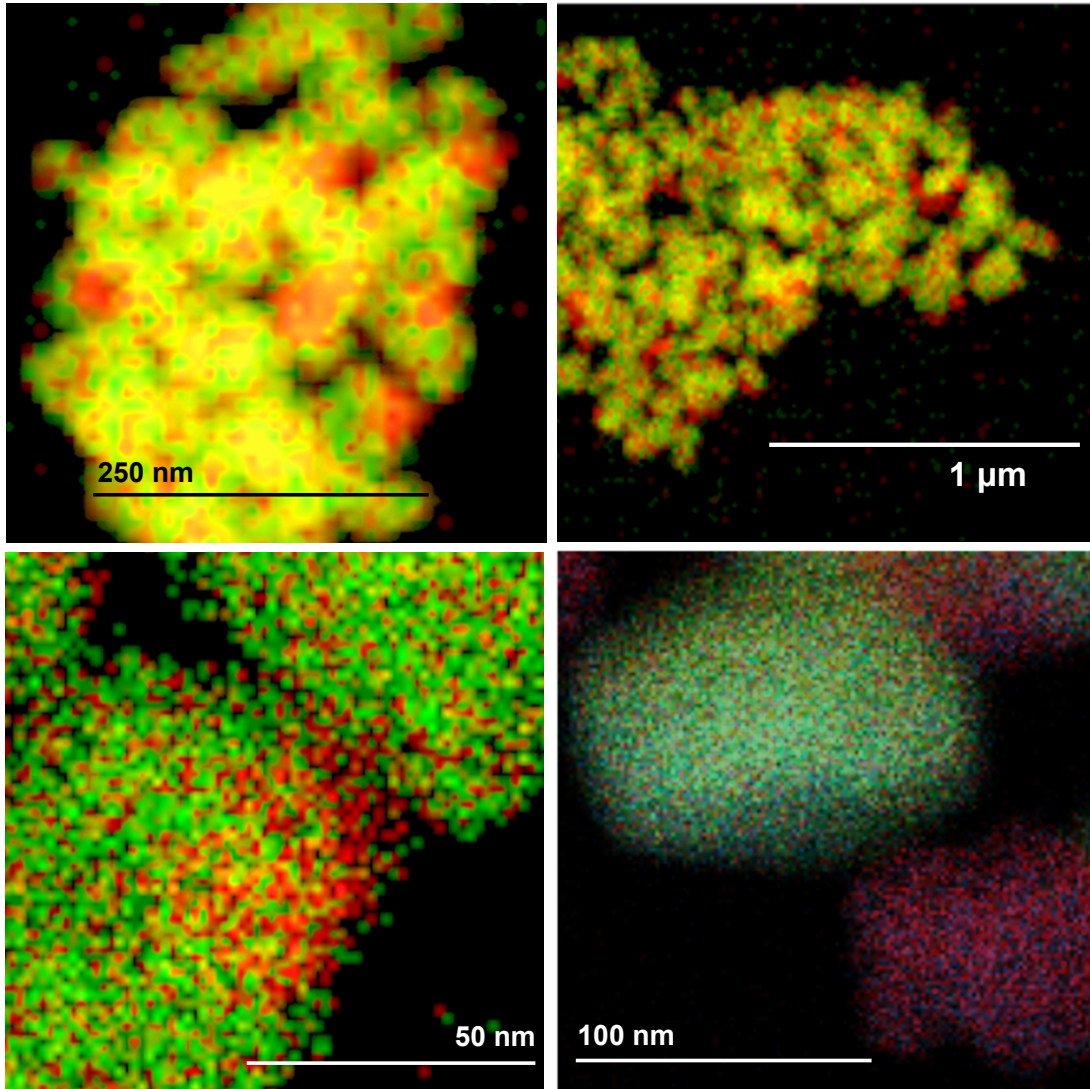


Figure 3.3: EDX map of 5% ITO (left) and 10% ITO (right). Top images are overall mapping of a cluster of primary particles, and bottom images are enlarged to focus on primary particles. Green is In, red is Sn, and blue is O (only included in right-bottom).

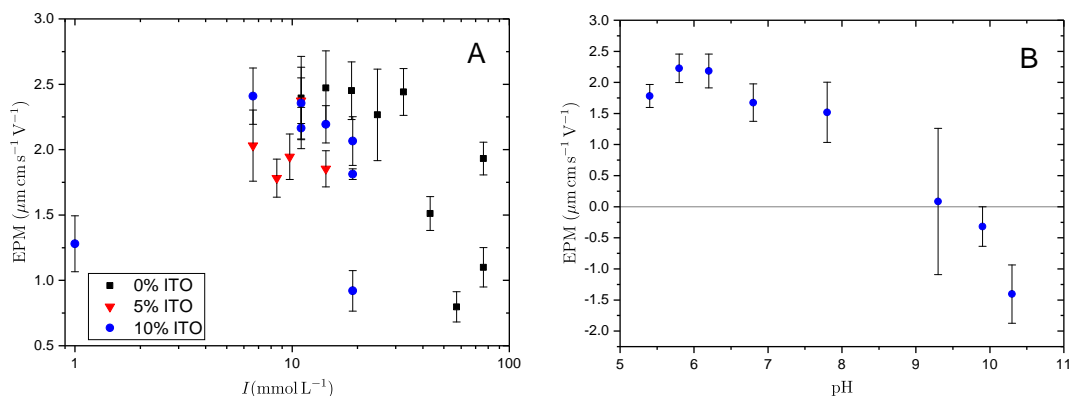


Figure 3.4: EPM of (a) 0 %, 5 %, and 10 % ITO at $\text{pH} = 6.00 \pm 0.04$ in 1.0 mmol L^{-1} MES buffer and electrolyte added as NaNO_3 ; and (b) 10 % ITO in 5 mmol L^{-1} NaCl . Error bars signify the standard deviation of a total of 9 to 15 data points from 3 injections of the same suspension into the instrument. Replicate sample points at the same I are true sample replicates (i.e., different suspensions) at I near the CCC of the particles.

experimental data crosses the abscissa in Figure 3.4b. This matches well with previous studies of pristine In_2O_3 particles.⁹² Furthermore, the EPM at $\text{pH} \approx 6.0$ in Figure 3.4b, which was collected for 10 % ITO in de-aerated, unbuffered 5 mmol L^{-1} electrolyte, is not significantly different than that collected at $\text{pH} = 6.00$ in 1.0 mmol L^{-1} MES buffer, indicating that the Good's buffer MES does not significantly change the surface charge.

The point of zero charge, p.z.c., which is similar to pH_{IEP} , is the pH when a particle has no net surface charge. Without some non-electrostatic stabilization mechanism, particles are destabilized at pHs near the p.z.c. since the low repulsion from low surface charge is not able to overcome attractive dispersion forces between particles. For mixed oxides, the p.z.c. has been shown to occur between the p.z.c. of the binary end-members, and not necessarily as a weighted average of end-member fractions.⁹³ The p.z.c. of In_2O_3 is approximately $\text{pH} = 9$, and the p.z.c. of SnO_2 is approximately $\text{pH} = 4.5$.⁹⁴ Thus, the p.z.c. of both 5 % and 10 % ITO would fall between $\text{pH} = 4.5$ and $\text{pH} = 9$, more likely falling near the higher end due to the larger amount of incorporated In_2O_3 .

From the trends of EPMs shown in Figure 3.4a, it appears likely that the p.z.c. of the commercial ITO trends as 0% > 10% > 5%. Thus, as the pH is increased from pH = 6 to pH = 8, the 5% ITO would be the first type to completely destabilize, since it likely exhibits the lowest p.z.c. Increasing the pH past the p.z.c. of the 5% ITO would cause the 10% to completely destabilize, followed by 0% ITO at an even higher pH. If the p.z.c. was some combination of the p.z.c. of the end-members, i.e., $\text{p.z.c.} = f(\chi_{\text{In}_2\text{O}_3})\text{p.z.c.}_{\text{In}_2\text{O}_3} + f(\chi_{\text{SnO}_2})\text{p.z.c.}_{\text{SnO}_2}$, one would expect the p.z.c. to trend as 0% > 5% > 10%. The different experimental trend indicates some other property, such as near-surface lattice strain, is likely important in the regulation of surface charge at ITO surfaces and dependent on the amount of substituted Sn.

Note that the EPM determined with MP-PALS is an average EPM — differentiation of EPMs from separate populations is not possible with this technique. Thus, the less positive or even negative EPM of distinct SnO₂ crystals at near-neutral pH is included in the average EPM, meaning the true EPM of the ITO crystals in the 10% may be underestimated in Figure 3.4. However, the effect of Sn level, whether in SnO₂ crystal form or incorporated into the ITO crystal, is embodied in this average EPM. For the 5% ITO, which has less free SnO₂ as determined by ICP-OES and TEM, the true EPM of the ITO crystals is likely slightly more positive than what was found in Figure 3.4a, but one cannot say for certain with this technique. Thus, comparison of EPMs among ITO types at the same pH and ionic strength is still a measure of the relative effect of Sn even when the exact crystalline forms including Sn are not known.

As discussed, EPM, and thus surface charge, of the bare commercial ITO samples did not follow expected trends of homogeneous solid solutions or mixtures of two completely different crystal types, with the 5% ITO behaving differently than expected relative to the 0% and 10%. The EPMs of the ligand-capped synthesized ITO are more in-

dicative of the EPMS of the ligand itself, but since the ligands are on highly-homogeneous ITO crystals, any differences in EPM observed among the synthesized ITO would be attributed to interaction between the ligand and crystal. No observed differences among EPMS of ligand-capped synthesized ITO would indicate the ligand dominates all surface charge, completely masking any effect of the nanocrystal differences.

The ZPs of PAA-PEO capped, synthesized ITO in water at $\text{pH} \approx 5.7$ are plotted against $[\text{CaCl}_2]$ in Figure 3.5. CaCl_2 was used as the electrolyte because aggregation experiments indicated high particle stability even at high NaCl concentrations, and determination of the ZP at high ionic strength is difficult due to hydrolysis of water and electrode degradation during experimental runs. Aggregation experiments in CaCl_2 resulted in better destabilization of particles at lower ionic strengths where ZP could be determined with better confidence. The ZP was calculated from the EPM using Smoluchowski's equation in the Malvern software. The ZP is the potential at the shear plane of a moving particle and is used extensively in modeling of stability in nanoparticle systems as a measure of surface charge. The ZP of all polymer-capped synthetic particles were negative in all conditions, although they were near zero for $[\text{CaCl}_2] \approx 30 \text{ mmol L}^{-1}$. The negative ZP is likely due to the PAA-PEO capping polymer covering the particle surface and screening the positive charge at the surface of the particle. However, differences in the ZP among ITO type were observed, indicating differences in the ITO surfaces were important and not completely screened by the polymer. At a given ionic strength, the ZP magnitude trended as $\text{ZP}_0 > \text{ZP}_8 > \text{ZP}_{10}$, and the stability of particles at $\text{pH} \approx 5.7$ would likely follow the same trend, since particles exhibiting ZPs of lower magnitude are less stable if electrostatics is the only stabilization mechanism. The results further indicate likely high stability for un-doped ITO, even in the presence of a ligand, and decreased stability with the inclusion of Sn.

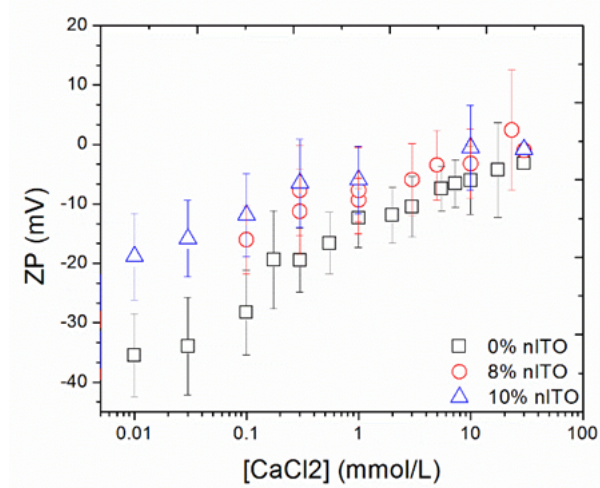


Figure 3.5: Zeta-potential of synthesized ITO particles at $\text{pH} \approx 5.7$ and in the presence of CaCl_2 .

3.3.2 Aggregation

Time series of effective z-average hydrodynamic radii, \overline{R}_{DLS} , of ITO were observed for various conditions to parse out how the level of Sn affected important aspects of particles stability. Namely, synthesized particle aggregation was investigated to see the effect of Sn on particle stability in the presence of an adsorbing ligand. Aggregation of commercial particles without stabilizing ligands was monitored at different pHs and in different electrolytes to determine if changes in surface charge or Hamaker constant were more important to changes in particle stability. Lastly, commercial ITO was added to an electrolyte containing NOM to simulate an environmental release and to investigate the effect NOM concentration has on particle stability. A summary of experimental conditions is given in Table 3.2, and aggregation behavior with respect to critical environmental parameters are discussed in the following sections.

Table 3.2: Values of parameters used in homoaggregation experiments along with estimates for CCC and β as fitting parameters to Equation 3.1. Uncertainty expressed as standard error of the estimate from nonlinear regression. ND = Not Determined.

ITO Source	ITO (%Sn)	pH	Electrolyte	NOM (mg L ⁻¹)	CCC (mmol L ⁻¹ as <i>I</i>)	β
Commercial	0	6.0	NaNO ₃	0	56.5 ± 1.2	3.50 ± 0.24
		7.0	NaNO ₃	0	29.7 ± 0.6	3.77 ± 0.24
		7.9	NaNO ₃	0	6.38 ± 0.17	2.62 ± 0.16
	5	6.0	NaNO ₃	0	14.7 ± 0.8	4.46 ± 0.94
		6.0	NaNO ₃ /NaCl ^a	0–2.5	~ 200	ND
		7.0	NaNO ₃	0	3.26 ± 0.13	3.03 ± 0.33
		7.9	NaNO ₃	0	<0.073	ND
		7.9	NaNO ₃ /NaCl ^a	0–2.5	230 ± 8	3.12 ± 0.30
		7.9	Ca(NO ₃) ₂	2.5	16.70 ± 0.53	4.62 ± 0.61
		10	6.0	NaNO ₃	0	27.4 ± 0.4
	6.0		Na ₂ SO ₄	0	4.00 ± 0.04	4.64 ± 0.19
	7.0		NaNO ₃	0	5.63 ± 0.09	3.01 ± 0.14
	7.9		NaNO ₃	0	1.18 ± 0.03	2.26 ± 0.12
Synthesized	0	~ 5.7	CaCl ₂	0	13.9 ± 6.0	ND
	8	~ 5.7	CaCl ₂	0	8.2 ± 0.1	ND
	10	~ 5.7	CaCl ₂	0	0.64 ± 0.04	ND

^a NaCl was used for high ionic strength experiments due to availability of stock solutions.

3.3.2.1 Effect of ligand presence

The set of synthesized ITO particles were all capped by PAA-PEO polymer in the same fashion. Ligand-stripped particles were added dropwise to DMF containing a dissolved PAA-PEO polymer and the polymer allowed to associate on the particle surface. The DMF was then added dropwise into excess water buffered at $\text{pH} = 9$ with borate and stirred for 48 h, at which point the capped ITO was concentrated and purified by spin dialysis. Ligands can have a huge effect on aggregation behavior, and large polymer capping agents can effectively screen all electrostatic interaction of the nanoparticle with the solution while sterically inhibiting particle aggregation.

To investigate the effect of the PAA-PEO polymer cap on nanoparticle stability, particle aggregation kinetics were monitored after addition of an aliquot of synthesized ITO stock to a solution containing CaCl_2 at $\text{pH} \approx 5.7$. Experiments using NaCl showed high particle stability even at high ($\sim 1 \text{ mol L}^{-1}$) ionic strength and are not included here. Figure 3.6 compares the stability of synthesized ITO nanocrystals by comparing the hydrodynamic radius for all the data collected up to $t_{trunc} = 500 \text{ s}$. The right plateau of each curve signifies diffusion-limited aggregation, and the inflection point is the estimated CCC for t_{trunc} . Clearly, the 10% ITO reached diffusion-limited aggregation at a lower ionic strength than the 8% ITO, with 0% ITO exhibiting the highest stability.

Plots of the estimated CCC as a function of the choice of t_{trunc} showed a time-dependence of the estimated CCC (not shown). The intercept of a 4th-order polynomial regression of CCC vs. t_{trunc} was taken to be an estimate of the CCC at short time periods, and these values are given in Table 3.2 along with estimates of the uncertainty. The estimates for $\text{CCC}_{t=0}$ show the same trend seen in Figure 3.6, with incorporation of Sn resulting in lower particle stabilities. This trend was also seen in the ZP data presented in Figure 3.5.

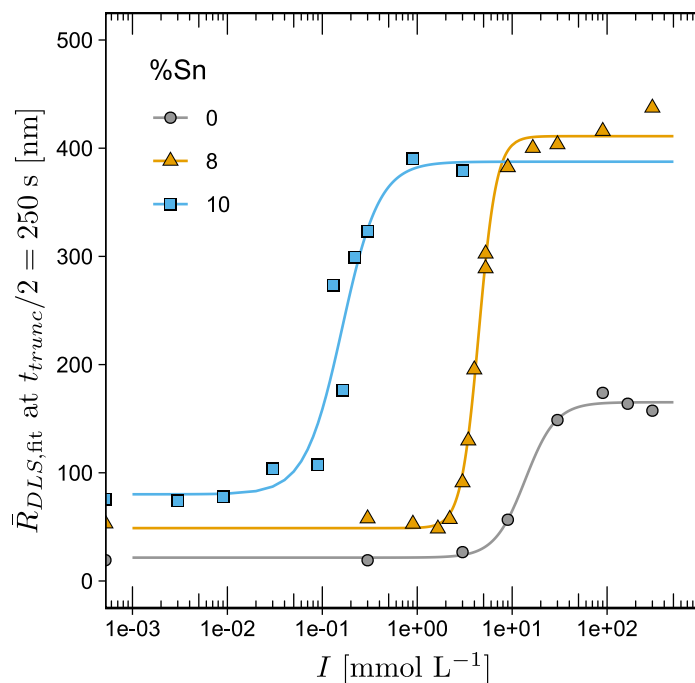


Figure 3.6: Fits of Equation 3.1 (lines) to fitted hydrodynamic radii for $t_{trunc} = 500$ s. All points correspond to a single aggregation history carried out at ambient pH ≈ 5.7 and addition of ionic strength as CaCl_2 . Particle concentrations were 120 mg L^{-1} , 60 mg L^{-1} , and 67 mg L^{-1} for 0%, 8%, and 10% ITO, and were chosen to get adequate photon counts while not having too rapid of aggregation.

Electrostatic destabilization of particles in solution by addition of electrolyte is more effective for low surface charges, since fewer ions are needed to effectively screen the particle charge. Since the particles exhibiting lower ZP are the least stable, it appears the destabilization mechanism of these particles is electrostatic — no evidence of substantial steric hindrance to particle aggregation was observed. A lower ZP with increased Sn content could mean two things (1) The polymer did not fully screen the particle surface charge and the (positive) surface trend comes through, or (2) the surface charge difference of the bare particles resulted in different amounts or orientations of the adsorbed capping polymer. In either scenario, the change in particle surface charge ultimately dictated the aqueous stability of the particles, with lower magnitudes of surface charge correlating to increased tin and lower particle stability.

3.3.2.2 Effect of pH and Sn level

To further investigate the effect of Sn, aggregation of bare commercial ITO was monitored at different pHs in the presence of electrolyte. As discussed in the previous section, the expected particle stability should be lowest near pH_{IEP} and increase in either direction as the surface gains positive (at lower pHs) or negative (at higher pHs) surface charge. The values for pH_{IEP} for the commercial ITO powders were in the range of 8 to 9.5. Thus, in the absence of NOM, the expected particle stability, as expressed in terms of the CCC, would be $\text{CCC}_{\text{pH}=6} > \text{CCC}_{\text{pH}=7} > \text{CCC}_{\text{pH}=7.9}$.

Figure 3.7 compares the stability of the commercial ITO powders at $\text{pH} = 6.0$ (Fig. 3.7a), $\text{pH} = 7.0$ (Fig. 3.7b), and $\text{pH} = 7.9$ (Fig. 3.7c), buffered with 0.1 mmol L^{-1} to 1.0 mmol L^{-1} MES, MOPSO, and HEPES buffer, respectively. Note that the 5% ITO was unstable with addition of only 0.1 mmol L^{-1} HEPES buffer. At concentrations below this amount, the carbonate species present in solution became significant, causing

the HEPES to lose buffering capacity. Thus, a full curve to find $\text{CCC}_{\text{pH}=7.9}$ could not be collected, and $\text{CCC}_{\text{pH}=7.9} < 7.3 \times 10^{-5} \text{ mol L}^{-1}$ as I for 5% ITO is assumed. Estimated CCC values using the TAA-logistic method are summarized in Table 3.2.

For each particle type, the stability trended as $\text{CCC}_{\text{pH}=6} > \text{CCC}_{\text{pH}=7} > \text{CCC}_{\text{pH}=7.9}$, as expected from estimates of pH_{IEP} from EPM measurements. At each pH, the particle stability followed 0% > 10% > 5%, which also mirrored the estimated trend in EPM measurements at pH = 6.0 at various ionic strengths, as shown in Figure 3.4. Thus, it appears the change in surface charge with Sn dopant level is the major factor that contributes to differences in particle stability and overcomes any concomitant increase in Hamaker constant.

3.3.2.3 Effect of counterion - Schulze Hardy rule

All of the aggregation experiments in Figure 3.7 were conducted in buffered suspensions with adjustment of ionic strength with NaNO_3 . Since ITO is positively charged at near-neutral pH, divalent anions, such as SO_4^{2-} or CO_3^{2-} should be more effective in compressing the electric double layer than monovalent anions, such as NO_3^- , due to higher charge densities. Both SO_4^{2-} and CO_3^{2-} can be found as minor or major constituents in surface waters, so they may be more important anions for ITO stability in aqueous environmental systems than other major anions, such as Cl^- .

Aggregation kinetics experiments were carried out using Na_2SO_4 as the electrolyte and compared to those with NaNO_3 to confirm the efficacy of SO_4^{2-} in destabilizing ITO nanoparticles. Figure 3.8 depicts the hydrodynamic radii at 425 s of aggregation as determined by cubic fits of 950 s of aggregation histories of 10% ITO at pH = 6.0 in both NaNO_3 and Na_2SO_4 electrolyte. The 10% ITO particles were clearly less stable in Na_2SO_4 electrolyte, as evidenced by the shift of the curve to lower ionic strengths. This

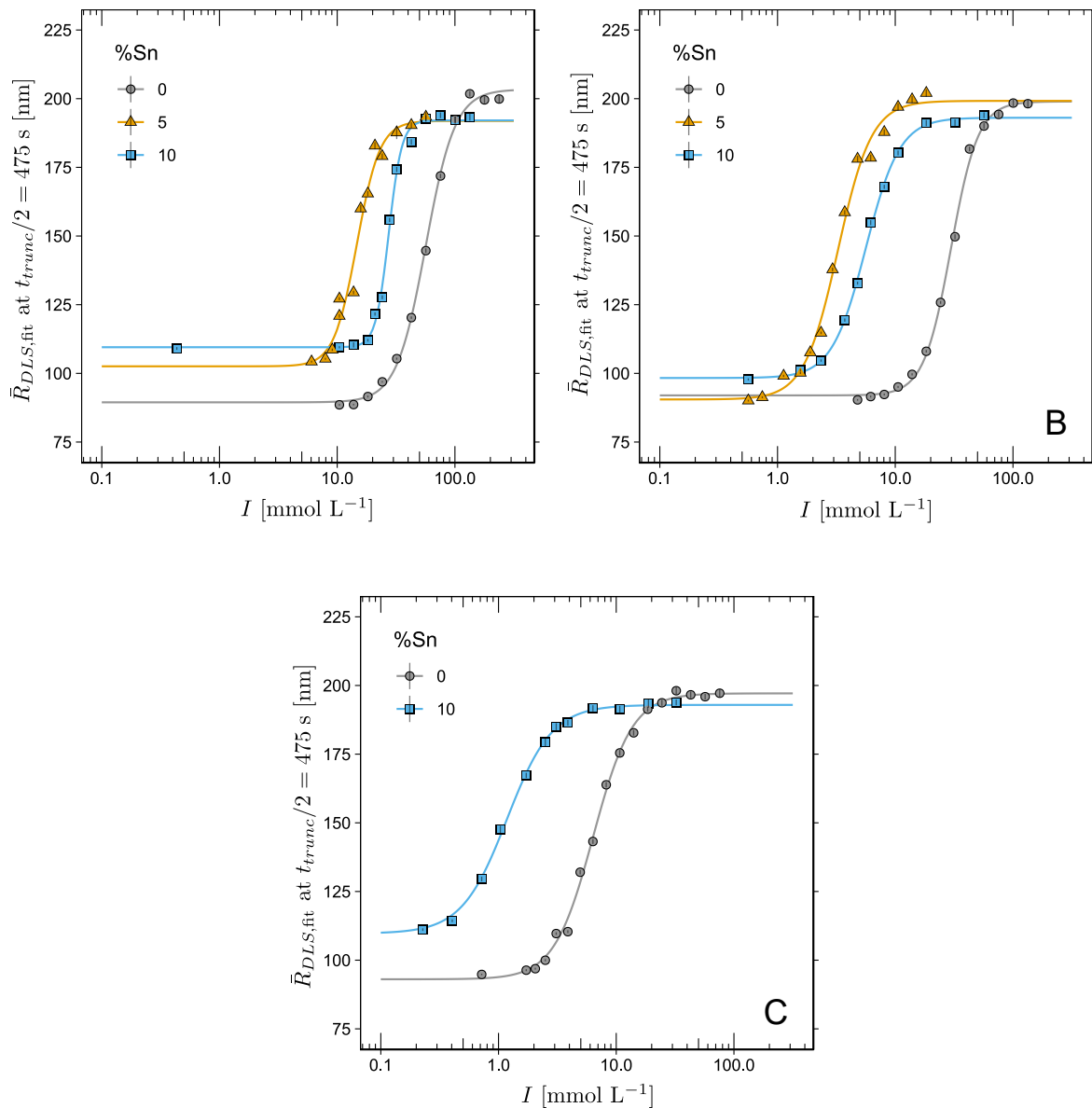


Figure 3.7: Fits of Equation 3.1 (lines) to fitted hydrodynamic radii for $t_{trunc} = 950$ s (points) for the following conditions: (a) pH = 6.0, NaNO₃ electrolyte; (b) pH = 7.0, NaNO₃ electrolyte; (c) pH = 7.9, NaNO₃ electrolyte. The 5% ITO was unstable with addition of only 0.1 mmol L⁻¹ HEPES buffer; therefore, a full curve to determine the CCC could not be collected at pH = 7.9.

confirms the greater efficacy of SO_4^{2-} in compression of the electric double layer than NO_3^- .

The Schulze-Hardy rule states that, for high surface charge, $\text{CCC}_{z:z}/\text{CCC}_{1:1} \propto z^{-6}$, where z is the valency of electrolyte. Thus, for a 2:2 electrolyte, such as CaSO_4 , one would expect a CCC that is 1/64 of that for a 1:1 electrolyte, such as NaNO_3 . Further mathematical treatment of the Poisson-Boltzmann equation found that, for high surface charge, $\text{CCC}_{2:1}/\text{CCC}_{1:1} \approx 1/42$, and for a diminishingly low surface charge, $\text{CCC}_{2:1}/\text{CCC}_{1:1} \approx 1/3.5$.⁹⁵ Noting that $[\text{Na}_2\text{SO}_4] = 1 \text{ mmol L}^{-1}$ is equivalent to $I = 1/2 \sum_i c_i z_i^2 = 3 \text{ mmol L}^{-1}$, the Schulze-Hardy rule for a 2:1 electrolyte in units of ionic strength translates to $\text{CCC}_{2:1}/\text{CCC}_{1:1} \approx 1/14$ for high surface charge and $\text{CCC}_{2:1}/\text{CCC}_{1:1} \approx 1/1.17$ for low surface charge. From Figure 3.8 and Table 3.2,

$$\text{CCC}_{\text{Na}_2\text{SO}_4}/\text{CCC}_{\text{NaNO}_3} \approx (4.5 \text{ mmol L}^{-1})/(30 \text{ mmol L}^{-1}) = 1/6.66$$

which is intermediate of the two extremes and would be expected for an intermediate surface charge. Thus, it's likely the ITO system obeys the Schulze-Hardy rule, since the EPM (a proxy for surface charge) at $\text{pH} = 6$ is moderate.

3.3.2.4 Effect of NOM

Previous studies have shown that the presence of NOM can either stabilize or destabilize nanoparticles depending on nanoparticle characteristics and solution chemistry.^{48,75} To investigate the effect of NOM on ITO particle stability, aliquots of 5% ITO stock were added to solutions of Suwanee River NOM and selected electrolyte to simulate a release of ITO nanoparticles to natural surface water. The concentration of NOM was $C_{\text{NOM}} = 2.5 \text{ mg L}^{-1}$ unless otherwise noted. Efforts were focused on 5% ITO since it exhibited the lowest stability in the absence of NOM, and it was hypothesized NOM would stabilize ITO through surface adsorption, subsequent charge reversal, and electrostatic

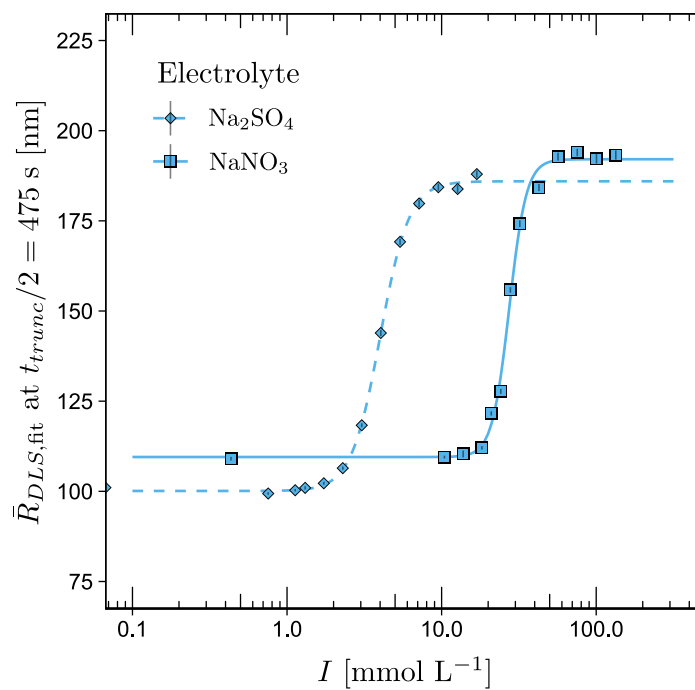


Figure 3.8: Fits of Equation 3.1 (lines) to fitted hydrodynamic radii for $t_{trunc} = 950$ s at pH = 6.0 in NaNO₃ (right, solid) and Na₂SO₄ (left, dashed). $C_{ITO} \approx 25$ mg L⁻¹ 10% ITO was used for all points.

and steric stabilization at near-neutral pHs.⁹⁶ Thus, if the NOM stabilized the 5% ITO, which had the lowest EPM (and thus surface charge) at pH = 6.0, it would stabilize the more positively-charged 10% and 0% ITO as well.

Figure 3.9 depicts the effect of addition of 2.5 mg L⁻¹ NOM on the stability of 25 mg L⁻¹ 5% ITO under various conditions. All points are hydrodynamic radii at $t_{trunc}/2 = 425$ s from least-squares cubic fits of the aggregation histories. The lines are best fits of Equation 3.1 to the associated grey points, and the inflection point of each line corresponds to the estimated CCC. The grey data points and lines correspond to pH = 7.9, a pH at which 5% ITO was unstable in the absence of NOM with addition of even small amounts of buffer, i.e., $CCC < 0.073$ mmol L⁻¹ as I . In the presence of NOM and NaNO₃ at pH = 7.9 (right set of points), $CCC_{1:1} \approx 230$ mmol L⁻¹ as I , clearly demonstrating that the presence of NOM stabilized the ITO in suspension. Furthermore, some aggregation experiments were carried out at pH = 6.0 with the same NOM concentration as the pH = 7.9 experiments. These points, which are unlabeled orange points, fell closely in line with the pH = 7.9 points, indicating pH had little effect on particle stability in the presence of NOM at near-neutral pH.

As shown in Figure 3.4, bare ITO particles exhibited a positive surface charge in the pH range investigated in this study, whereas NOM carries a strong negative charge in the same pH range.⁹⁶ Thus, a likely mechanism for ITO stabilization by NOM is adsorption of NOM to the ITO surface, switching the positive ITO charge to an overall large negative charge capable of electrostatically stabilizing the ITO/NOM particle. A suspension of 5% ITO at pH = 6.0 containing $C_{ITO} \approx 25$ mg L⁻¹, $C_{MES} = 1.0$ mmol L⁻¹, and $C_{NaNO_3} = 10.0$ mmol L⁻¹ exhibited a ζ -potential (from EPM and Smoluchowski equation) of (17.6 ± 2.5) mV while an identical suspension containing an additional $C_{NOM} = 2.5$ mg L⁻¹ exhibited a ζ -potential of (-44.4 ± 1.4) mV. Thus, NOM appeared to lead to

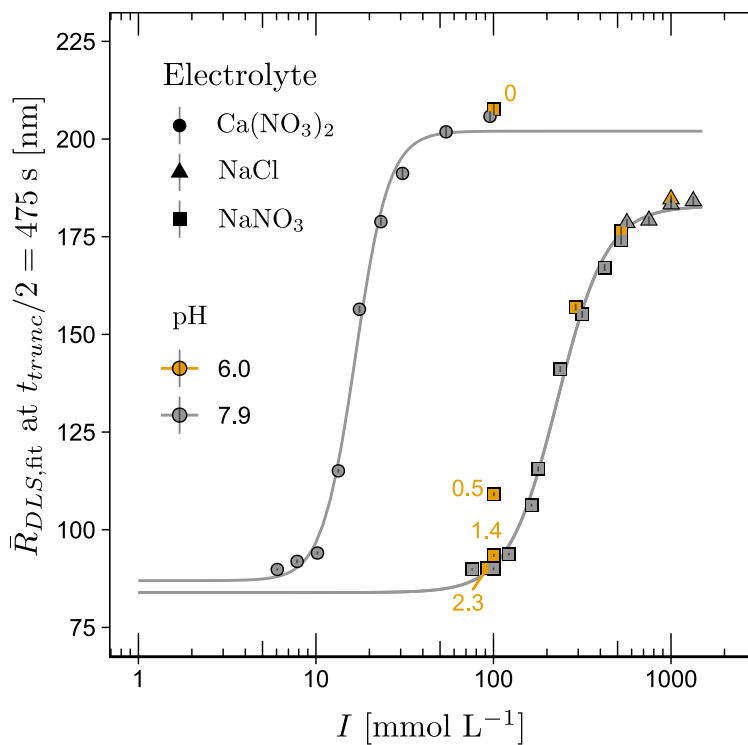


Figure 3.9: Fits of Equation 3.1 (lines) to fitted hydrodynamic radii for $t_{trunc} = 950$ s at pH = 7.9 (grey) and pH = 6.0 (orange) in NaNO₃ and NaCl (right line) and Ca(NO₃)₂ (left line). For all points, $C_{ITO} \approx 25$ mg L⁻¹. NaCl was used at higher ionic strengths due to immediate availability of stock solutions. Also shown are points where NOM concentrations were adjusted at a given pH and electrolyte concentration (points labeled with NOM concentration in mg L⁻¹). $C_{NOM} = 2.5$ mg L⁻¹ for all other points.

a charge reversal from adsorption onto the ITO surface.

To further investigate the mechanism of stabilization of ITO by NOM, aggregation of 5% ITO in the presence of NOM was monitored following addition of $\text{Ca}(\text{NO}_3)_2$ at $\text{pH} = 7.9$. The particle stability decreased relative to that when NaNO_3 or NaCl were used as electrolyte as evidenced by the shift of the curve in Figure 3.9 to lower ionic strengths, but was more stable than bare ITO at the same pH . Recall that, for a 2:1 electrolyte and high surface charge, $\text{CCC}_{2:1}/\text{CCC}_{1:1} \approx 1/14$ in terms of ionic strength. From the data shown in Figure 3.9,

$$\text{CCC}_{\text{Ca}(\text{NO}_3)_2}/\text{CCC}_{\text{NaNO}_3} \approx (16.7 \text{ mmol L}^{-1})/(230 \text{ mmol L}^{-1}) = 1/13.8$$

which is very close to the theoretical limit suggested by the Schulze-Hardy rule. Thus, the stabilization of ITO by NOM is most likely largely electrostatic in nature.

Some studies have observed aggregation rates of nanoparticles in excess of the diffusion-limited rate in the presence of NOM or other organic polymers for Ca^{2+} concentrations higher than the CCC.^{75,97} In Figure 3.9, this would mean the samples would not plateau at higher concentrations, but rather continue increasing. Such behavior has been attributed to bridging between both adsorbed and free NOM by Ca^{2+} ions, causing the collision cross-section of an aggregate to increase. Such behavior was not observed with ITO and the NOM used in this study. The orange point labeled “0” in Figure 3.9 was an experiment run on the same day as the $\text{Ca}(\text{NO}_3)_2$ experiments, i.e., from the identical particle stock, with NaNO_3 as the electrolyte and in absence of NOM at $\text{pH} = 6$. The aggregation rate of this point is diffusion-limited, i.e., the ionic strength is well above the associated $\text{CCC}_{5\% \text{ITO}} \approx 20 \text{ mmol L}^{-1}$ shown in Figure 3.7a and Table 3.2. The aggregation experiments with $\text{Ca}(\text{NO}_3)_2$ as electrolyte in Figure 3.9 show aggregation rates approaching, but not exceeding, this diffusion-limited rate. Thus, calcium bridging had minimal effect on particle stability in this system.

Lastly, the effect of NOM concentration on aggregation kinetics was investigated. Aliquots of 5 % ITO were added to 100 mmol L⁻¹ NaNO₃ solutions at pH = 6.0 that contained 0 mg L⁻¹, 0.5 mg L⁻¹, 1.4 mg L⁻¹, and 2.3 mg L⁻¹ NOM, shown as orange squares labeled with the NOM concentration in Figure 3.9. As the NOM concentration decreases from 2.3 mg L⁻¹ to 0 mg L⁻¹, the radius at time $t_{trunc}/2$ increases, indicating relatively less stable particles. Each point can also be imagined as a sampling of the right curve as it is shifted left, i.e., as the particle stability decreases. Thus, the point with $C_{NOM} = 1.4 \text{ mg L}^{-1}$ has a CCC about 20 mmol L⁻¹ less than that of $C_{NOM} = 2.5 \text{ mg L}^{-1}$, and the $C_{NOM} = 0.5 \text{ mg L}^{-1}$ has a CCC roughly 100 mmol L⁻¹ less. From Figure 3.9, it is quite clear that addition of even a small amount of NOM resulted in large increases of particle stability.

3.3.3 Environmental implications

Releases of nanoparticles and other ENMs to the environment inevitably get transported to surface waters, whether it be from direct discharge or precipitation and runoff. Indium tin oxide is an industrially-produced ENM, and the Sn content of ITO can be adjusted to arrive at desired optoelectronic behaviors. Although ITO is an industrial-relevant ENM, little study of aquatic behavior of ITO has been done. The results of this study indicate that the stability of ITO nanoparticles trends with the surface charge of ITO in solution, which is in turn dependent on the Sn level within ITO. For polymer-capped ITO nanocrystals synthesized in this study, the stability trended as 0 % > 8 % > 10 %, and the trend likely mirrored that of the native surface charge of the particles. For the commercial particles used in this study, the surface charge and stability trended as 0 % > 10 % > 5 % at near-neutral pH. Previous studies on homogeneous solid solutions would suggest a surface charge and stability trend of 0 % > 5 % > 10 % ITO at near-neutral pH, indicating the commercial ITO did not behave as expected. Thus, for

ITO and likely for other mixed metal oxides, other factors, such as point defects near the surface of the lattice, may play an important in aggregation behavior in electrolyte solutions. Nevertheless, NOM was shown to electrostatically stabilize ITO at near-neutral pHs, likely shielding any differences in particle stability due to differences in Sn levels exhibited by bare ITO particles.

Chapter 4

Effect of tin dopant level on dissolution behavior and photogeneration of hydroxyl radicals by indium tin oxide nanoparticles

4.1 Introduction

Metal oxide-based nanomaterials are an important class of engineered nanomaterials (ENMs) that are increasingly utilized in a number of industries for various applications.^{1,2} One reason for the widespread use of metal oxide nanomaterials is the wide range of beneficial uses owing to the unique behaviors associated with the numerous possible metal oxide combinations. For example, TiO_2 is used in a wide variety of applications, such as pigments and photocatalysis, because of its interaction with light and low solubility.⁹⁸⁻¹⁰⁰ In medicine, magnetic Fe_3O_4 particles are used for MRI imaging¹⁰¹ and targeted drug delivery.¹⁰² Metal oxide nanomaterials can be formed from a single metal, such the binary metal oxides ZnO , TiO_2 , and Al_2O_3 , or two or more metals, which are called bimetallic or polymetallic oxides, doped metal oxides (in the case the dopant is also a metal), or mixed metal oxides. Doped metal oxides often exhibit unique characteristics, especially regarding behavior of electrons. As such, they are often used in electronic or catalytic capacities.⁹ Furthermore, impurities in metal oxide structure, such as O vacancies or N substitution for O, can be introduced to alter the behavior.^{103,104}

The multitude of unique compositions of metal oxide nanoparticles also results in a wide range of environmental fate and transport of these particles. Because metal oxide nanoparticles are increasingly prevalent, many studies have investigated the en-

vironmental transport,⁴³ transformation,^{105,106} and toxicity^{13,14} of binary metal oxide nanoparticles. For binary metal oxide nanoparticles, numerous modes of toxicity in both mammalian cells and *E. coli* highly correlated with two main characteristics: aqueous solubility and the energy level of the conduction band minimum, E_{CBM} .^{13,14} Metal oxide nanoparticles with relatively higher aqueous solubilities were able to leach potentially-toxic metal ions, such as Cu^{2+} or Zn^{2+} , whereas particles with $-4.12 \text{ eV} > E_{\text{CBM}} > -4.84 \text{ eV}$ with respect to vacuum were able to disrupt cellular redox processes by accepting or donating electrons. Toxicity of metal oxide nanoparticles has also been correlated to ability of the nanoparticle to generate reactive oxygen species (ROS), such as OH^\bullet , $\text{O}_2^{\bullet-}$, or $^1\text{O}_2$, upon illumination, which can subsequently react with and disrupt cell membranes.¹⁵ Thus, both the solubility and electronic band structure of metal oxide nanoparticles are important indicators of potential toxicity.

Fewer studies have investigated the routes of toxicity of doped metal oxides, but the body of literature is growing. Stankic et al. recently compiled a review of antibacterial properties of metal oxides, including doped metal oxides.¹⁰⁷ Doped metal oxides exhibit not only different overall cytotoxic potentials, but also different routes of toxicity than the end-member metal oxides. For example, numerous studies have demonstrated that doping of ZnO nanoparticles with Fe reduces the rate of Zn^{2+} leaching and associated toxicity from that of pure ZnO.^{17,18,108} However, introduction of Fe into ZnO also increases the photocatalytic activity toward ROS production, increasing cytotoxic effects through that route.¹⁰⁹

One doped metal oxide with a large existing market is indium tin oxide (ITO), which is used in LCD displays and other optoelectronic applications. Approximately 700 t of indium is produced annually,²⁴ the majority of which for manufacture of ITO thin films,⁷⁹ placing it among the top 10 produced ENMs on a mass basis.¹ Although ITO

is currently produced as a thin film at a doping level of 90:10 wt%:wt% In_2O_3 : SnO_2 , current research direction points toward production of thin films composed of small (<10 nm) nanoparticles with variable Sn content based on the desired optical and electronic behavior.^{110–113} Dissolution of ITO has been studied extensively, but usually in regards to acid etching to form electrical contacts or indium recovery from spent electronics.^{27,114,115} Only two studies have investigated ITO dissolution at $\text{pH} > 4$,^{26,29} with one finding preferential dissolution of In at near-neutral conditions.²⁹ Toxicity of ITO to microorganisms or aquatic species has been demonstrated,^{35–37} but the effect of Sn dopant level on routes of toxicity has not yet been studied.

This study uses ITO as an example doped metal oxide to investigate how two major predictors of metal oxide toxicity, metal ion release and energetic band structure, are affected by incorporation of a minor cation (Sn^{4+}) into a metal oxide crystal (In_2O_3). Specifically, dissolution of nanoparticulate In_2O_3 and ITO with two different Sn-levels was investigated in controlled batch experiments and a flow-through atomic force microscope (AFM) setup to elucidate the effect of Sn level on thermodynamics and kinetics of ITO dissolution. The electronic band structure of the ITO powders were also interrogated with ultraviolet photoelectron spectroscopy (UPS) and diffuse-reflectance UV-Vis spectroscopy, while a hydroxyl radical probe was used to investigate if aqueous ITO suspensions could produce ROS under UV irradiation at environmentally-relevant pHs. The objective of this study was to determine whether trends in particle dissolution rates and photogeneration of reactive oxygen species (ROS) in aqueous systems can be correlated to the amount of SnO_2 in ITO.

4.2 Materials and methods

4.2.1 Materials

Indium tin oxide (ITO) nanopowders with primary particle size of $a \approx 50$ nm and 3 different tin levels, i.e., 100:0, 95:5, and 90:10 wt%:wt% In_2O_3 : SnO_2 were procured from a commercial vendor (MKnano, Canada).

The following chemicals were used as received: NaClO_4 (98.0 %-102.0 %, Alfa Aesar), HClO_4 (99.9985 %, Alfa Aesar), NaCl (99.998 %, Alfa Aesar), NaNO_3 (ACS grade, ≥ 99.0 %, Sigma-Aldrich), HNO_3 (TraceMetal grade, Fisher Scientific), MES hydrate (≥ 99.4 %, Sigma-Aldrich), 2 N NaOH (Baker Analyzed grade, J.T. Baker), and terephthalic acid (TPA) (98 %, Sigma-Aldrich).

Salts were dried at 105°C overnight before use. All solutions were prepared in Type 1 reagent grade water ($18\text{ M}\Omega\text{ cm}$) from a Millipore Elix Essential followed by Synergy UV High Flow system. Solutions were generally stored in amber HDPE bottles or PP centrifuge tubes that were soaked in 10 % HNO_3 overnight and rinsed with copious amounts of deionized water followed by a reagent water rinse.

Determinations of pH of solutions and suspensions were done after a standard 3-point calibration with either a Sensorex S900C or Orion Ross Ultra 8103BNUWP pH probe and Orion Star A211 pH meter.

4.2.2 ITO dispersion preparation

A bath-sonication method was used to prepare suspensions of ITO due to evidence of release of negatively-charged tip particles from a probe sonicator.⁸¹ Approximately 10 mg of ITO nanoparticles was added to 5 mL reagent water in a acid- and base-washed 15 mL polypropylene (PP) centrifuge tube. The tube was then clamped vertically to a ringstand and the bottom of the vial placed near the base of the sonication bath (Branson

CPX2800, Branson Ultrasonics, USA). The tube cap was screwed on loosely to allow for better cavitation within the suspension. Ice was added to the bath to keep the bath below or near ambient temperature. The sonicator was run continuously at a setting of HI for 45 min.

For batch dissolution experiments, the sonicated dispersion was used as is. For other experiments requiring ITO in suspension, 7 mL of reagent water was added and the dispersion centrifuged with a swinging bucket rotor at 2000 RCF for 7 min to 10 min with acceleration and deceleration ramp settings of 0 (Eppendorf 5804 with A-4-44 rotor, Germany). For flow-through AFM experiments, 1 mL of supernatant was retained for sample preparation. For the TPA hydroxyl probe test, 7 mL of supernatant was retained in an amber, base-leached, HDPE bottle to select the smallest aggregate sizes for future study. This process was repeated with subsequent 10 min sonication times until an adequate volume of supernatant was retained for the experiments.

4.2.3 Dissolution experiments

4.2.3.1 Batch dissolution experiment

Reagent water was boiled the day prior to the start of the batch dissolution experiment. After about 15 min of a rolling boil, the water was quickly poured into borosilicate Nalgene bottles which were immediately capped and allowed to cool. The water-filled bottles were then transferred to a glovebox containing N₂ (Labconco Protector Glove Box Model 50700, USA) and the water poured into FEP bottles, which were left uncapped overnight to allow residual dissolved CO₂ and O₂ to escape into the N₂ atmosphere.

The suspensions of ITO prepared for the batch dissolution experiments were not centrifuged after sonication, but instead immediately capped and brought into the anaerobic glovebox. Each ITO suspension was split into two FEP bottles that contained

degassed reagent water and enough dried NaClO_4 to result in a final concentration of 5 mmol L^{-1} NaClO_4 . The mass concentration of ITO in each of these stock solutions was about 50 mg L^{-1} . The pH of one stock suspension was adjusted to $\text{pH} = 4.0$ and the other to $\text{pH} = 6.0$ with 0.1 mol L^{-1} and $1 \times 10^{-3} \text{ mol L}^{-1}$ HClO_4 , respectively. Each stock solution was split into acid-washed FEP and PP centrifuge vials, the caps screwed on tightly, and Parafilm applied around the caps. The vials were then sealed in two Ziploc bags, brought out of the N_2 chamber, put on a rotary shaker table, and covered with two black plastic bags to ensure dark conditions.

To determine aqueous In and Sn concentrations at a given time interval, a method detailed in Rai et al. was used. Briefly, a set of batch vials, i.e., 0 %, 5 %, and 10 % ITO at $\text{pH} = 4$ and $\text{pH} = 6$, were centrifuged at 2000 RCF for 25 min and then moved into the N_2 atmosphere. From each vial, 1 mL of supernatant was placed into a 3 kDa centrifugal filter (Amicon) and centrifuged at 4000 RCF for 30 min. The centrifuge filter was then brought back into the N_2 atmosphere and the filtrate removed and discarded. Then, 5 mL of supernatant was added to the filter and centrifuged at 4000 RCF for 30 min. This filtrate was added to pre-prepared 15 mL PP centrifuge tubes containing a solution of reagent water and HNO_3 to result in 10 mL of solution acidified to 2 % v/v HNO_3 for analysis on ICP-MS.

In and Sn concentrations were determined using an Agilent 7500ce ICP-MS at the University of Texas at Austin (Dept. of Geological Sciences). The instrument was optimized for sensitivity across the AMU range, while minimizing oxide production (1.5 %). Internal standards, mixed into unknowns via in-run pumping, were used to compensate for instrumental drift and internal standard sensitivity variations were well within QA tolerances (± 50 %). Limits of detection (LODs), were determined from a population of blank (2 % HNO_3) analyses interspersed throughout the analytical sequence. Analyte

recoveries obtained for replicates ($n = 4$) of an independent quality control standards (5 ppb) were typically within 2% (In) and 8% (Sn) of certified values, with mean standard deviations of 0.11 (In) and 0.12 (Sn). Relative standard deviations were computed from triplicate injections of each QA standard and unknown.

4.2.3.2 Flow-through AFM dissolution experiment

Muscovite mica sheets (12 mm V-1 grade, Electron Microscopy Sciences) were attached to magnetic sample pucks with Devcon 5-ton epoxy. The mica were then cleaved using ScotchTM tape in reagent water and dried in a stream of high-purity N₂. Muscovite mica¹¹⁶ has a point of zero charge (p.z.c.) of $\text{pH}_{\text{p.z.c.}} < 3$ while ITO has a p.z.c. around 8 to 9 as shown in Figure 3.4b. Thus, suspended ITO particles would be able to electrostatically adsorb or deposit on a mica surface. To adsorb ITO to mica, 40 μL of centrifuged ITO suspension was drop-cast onto the freshly-cleaved mica and allowed to sit quiescently for 1 h. The excess ITO suspension was then rinsed off with reagent water and the sample discs dried in a gentle stream of N₂.^{117,118}

For AFM imaging, a DNP-10 “A” cantilever was used (nominal spring constant $k = 0.35 \text{ N m}^{-1}$) in a fluid cell on a Bruker MultiMode 8 AFM with Nanoscope V controller and “J” scanner. Prior to imaging, the cantilever was exposed to a UV-ozone treatment (UVP HL-2000 HybriLinker) for 5 min and 120 mJ cm^{-2} to remove adsorbed organics. An ITO-laden sample puck was placed on the scanner and the tip brought into close proximity to the sample to ensure a good seal between the fluid cell and sample. Fluid was pulled through the cell at a rate of 0.5 mL min^{-1} with a peristaltic pump from an HDPE Mariotte bottle with the head level set about 2 cm above the fluid cell in order to keep the mica wetted. The fluid was $10 \text{ mmol L}^{-1} \text{ NaNO}_3$, and pH was adjusted to $\text{pH} = 4$ with concentrated HNO_3 or $\text{pH} = 6$ with addition of $2.0 \text{ mol L}^{-1} \text{ NaOH}$ and MES

powder with a final concentration of 0.1 mmol L^{-1} MES. The AFM was allowed to warm up for 1 h prior to imaging to reduce piezo drift, and flow was paused during all imaging. The tip was offset by $50 \mu\text{m}$ during imaging to reduce tip shielding effects.¹⁰⁵

All images were acquired in ScanAsyst or PeakForce Quantitative Nanomechanical Property Mapping (PeakForce QNM) mode, and at least three images were taken during each imaging event. An initial image with a scan size of $20 \mu\text{m}$ and scan rate of 0.5 Hz was acquired in order to find particles previously imaged in higher resolution. A $6.6 \mu\text{m}$ image and a $2.2 \mu\text{m}$ image of previously-imaged particles were acquired at a scan rate of 1.0 Hz . The PeakForce Setpoint was set at 0.03 V for each image to minimize movement of particles by tip-particle interaction. All images had a resolution of 512 samples/line, resulting in point-to-point distances of 39 nm , 13 nm , and 4.3 nm for $20 \mu\text{m}$, $6.6 \mu\text{m}$, and $2.2 \mu\text{m}$ images, respectively.

AFM images were analyzed using freely-available Gwyddion software, version 2.51.¹¹⁹ The particle height was used as the metric for comparison of particle size among images, since tip convolution resulted in lateral stretching of the particles. Images were first leveled using a revolving arc in both directions with a real radius of half of the image width, as this leveling technique has been shown to be superior to other flattening techniques in analyzing nanoparticle heights.¹²⁰ Particles were then identified with a grain height threshold of roughly 10 nm , and this threshold was adjusted to ensure neighboring particles were counted as distinct. Then, maximum heights of each grain (i.e., particle) were determined using grain distributions.

4.2.4 Electronic band structure

4.2.4.1 X-ray and ultraviolet photoelectron spectroscopy

X-ray photoelectron spectroscopy (XPS) is a surface-sensitive interrogation technique that gives binding energies of core electrons — information useful when quantifying relative amounts of surface atoms or distinguishing bond types among the same atom, e.g., a relative amounts of C–C and C–O bonds. Ultraviolet photoelectron spectroscopy (UPS) is similar to XPS, but uses lower energy UV-radiation to interrogate the surface, giving information about less-tightly bound valence electrons. For semiconducting materials, UPS can yield information such as the work function, ϕ , and ionization potential, I_p , which can be used to find the valence band maximum, $E_{\text{VBM}} = I_p - \phi$.⁹ Thus, a combination XPS/UPS analysis can result in characterization of surface concentrations of atoms of interest and determination of E_{VBM} and the Fermi level, $E_{\text{F}} = E_{\text{vac}} - \phi$. Both are typically performed under ultrahigh vacuum conditions on dry samples, as was done in this study.

Sample preparation. A piece of double-sided conductive carbon tape (Ted Pella, Inc.) was adhered to 316 stainless steel XPS sample bar. Approximately 10 mg of each ITO nanopowder was pressed into the tape with a stainless steel microspatula. The sample bar was then gently tapped to remove any ITO powder not adhered to the sample tape. To provide a Fermi-level reference, a gold-sputtered silicon plate was placed on the sample bar and screwed into place with a copper clamp to ensure conductivity between the gold film and the sample bar.

XPS operating conditions. The photoelectron spectrometer used in this study was the Kratos Axis Ultra DLD with a hemispherical analyzer capable of ultrahigh vacuum x-

ray photoelectron spectroscopy (XPS), ultraviolet photoelectron spectroscopy (UPS), and low-energy ion scattering spectroscopy. The prepared sample bar was loaded into the sample transfer chamber and allowed to pump down overnight (about 17 h) to 7×10^{-9} Torr. The bar was then loaded into the sample analysis chamber, which had a pressure of 3×10^{-9} Torr during XPS experiments.

Low-resolution XPS survey spectra of the gold reference and ITO samples were collected to determine proper sample locations, verify chemical composition of the samples, and to ensure adequate surface cleaning from Ar^+ ion sputtering by reduction of the adventitious C 1s peak. The photoelectron analyzer was operated in spectrum mode with a slot aperture and the kinetic energy was scanned from 286.69 eV to 1486.69 eV with a step size of 1.0 eV, a dwell time of 300 ms, and a pass energy of 80 eV. The x-ray source was monochromatic Al $K\alpha$ emission with an energy of 1486.69 eV.

An XPS survey spectrum was collected for each sample and the reference. The gold reference was then sputtered for 1 min with Ar^+ ions accelerated toward the reference at 4 kV to remove adventitious carbon on the surface due to previous exposure to ambient air. The gold reference was then rescanned to verify removal of the adventitious carbon.

UPS operating conditions. After the initial XPS scans, the Kratos was switched over to differential-pump UPS mode using a He I emission line with an energy of 21.21 eV as the photon source. The pressure in the sample analysis chamber was increased to 4×10^{-8} Torr during UPS experiments. The photoelectron analyzer was operated in spectrum mode with a 110 μm aperture and the kinetic energy was scanned from 5.00 eV to 35.00 eV with a step size of 0.05 eV, dwell time of 500 ms, and a pass energy of 5.00 eV. The sample bar was biased at -10 V to ensure electrons at the secondary electron cutoff

would have enough kinetic energy for determination of the work functions of the samples. UPS spectra were collected in triplicate. Additionally, a spectrum of the carbon tape was collected to confirm uniqueness of the ITO spectra. The values for E_F for the Au reference and ITO samples were determined by taking the midpoint of the spectra at the secondary electron cutoff, and the values of $E_F - E_{VBM}$ for ITO were determined from the onset of the valence electrons relative to the E_F of the gold reference.

4.2.4.2 Diffuse reflectance UV-vis spectroscopy

A Cary 5000 UV-Vis-NIR spectrophotometer with integrating sphere diffuse reflectance accessory was used to determine the apparent optical band gap, $E_{g,opt}$, of nanopowders. Each ITO nanopowder was pressed into a carbon tape and placed onto a black sample holder, which was placed at the rear of the integrating sphere chamber. Total reflectance spectra were collected at wavelengths of 200 nm to 600 nm with a resolution of 1 nm. Specular reflectance was negligible, likely due to the small particle size, so the total reflectance spectra was taken to be that of diffuse reflectance. The resulting spectra were analyzed using the Kubelka-Munk transformation in a Tauc plot to determine $E_{g,opt}$ of the ITO powders.¹²¹ The reflectance data were transformed using Equation 4.1

$$F(R) = \frac{(1 - R)^2}{2R} \quad (4.1)$$

where R is the wavelength-dependent reflectance. The Kubelka-Munk transformation was used as α in Equation 4.2, known as a Tauc plot,

$$F(R) = \alpha \propto \frac{(h\nu - E_{g,opt})^\gamma}{h\nu} \quad (4.2)$$

where $h\nu$ is the energy of radiation (eV), and $\gamma = 0.5$ or $\gamma = 2$ for a direct-allowed or indirect-allowed optical band gap material, respectively.^{121,122} A recent study suggested an alternative method for determining $E_{g,opt}$ of bulk, degenerate, polycrystalline semiconductors such as ITO.¹²³ However, the current study focuses on ITO nanoparticles, which would exhibit localized energy states, a condition more appropriate for the Tauc plot method.¹²³

Estimates for $E_{g,opt}$ from Equation 4.2 were determined by first plotting $(F(R)h\nu)^2$ vs $h\nu$. Then, an algorithm was implemented in R to minimize the uncertainty of the intercept of the line with the abscissa, which also minimized the uncertainty in the estimate of $E_{g,opt}$. At least 15 points were required in each regression to avoid identifying a portion of the lower-energy tail as the linear portion of the curve, and most regressed lines included more than 15 points. The estimate was bounded by $3.0 \text{ eV} < E_{g,opt} < 4.3 \text{ eV}$ based on visual inspection of the $[F(R)]^2$ curves.

4.2.5 Terephthalate hydroxyl probe test

Terephthalate (TP) has been shown to be a selective probe molecule for detection and quantification of hydroxyl radicals in aqueous solutions.^{124,125} TP does not exhibit significant fluorescence, and reaction of a hydroxyl radical with the aromatic ring of TP results in only one molecule with significant fluorescence, 2-hydroxyterephthalate (TPOH), resulting in sensitive detection of the fluorescent product. Terephthalate has also been shown to be resistant to direct oxidation by surface-bound holes, making it superior to other fluorescent hydroxyl probes that are susceptible to hole oxidation.¹²⁶ However, while TP exhibits minimal adsorption at $\lambda > 310 \text{ nm}$, TPOH has an absorption peak at 275 nm to 350 nm and has been shown to degrade by direct photolysis.¹²⁷ Since this study was comparing relative hydroxyl production rates among ITO types for fixed

wavelengths and intensities, photolysis of TPOH was not taken into account.

A stock solution of terephthalate was prepared by dissolving terephthalic acid (TPA) in 0.02 mol L^{-1} NaOH, which was then adjusted to $\text{pH} \approx 6.1$ with 0.1 mol L^{-1} HCl. Suspensions of ITO nanopowders were prepared as discussed above. Mixtures of ITO suspension, TPA stock solution, 1.0 mol L^{-1} NaCl solution, and reagent water were prepared in an amber HDPE bottle to result in desired final concentrations of ITO, TPA, and NaCl. Adjustments to pH of the final mixture were done by addition of 0.1 mol L^{-1} NaOH solution.

The ITO/TPA/NaCl mixture was then split into 1.2 mL plastic vials (1.00 mL of mixture in each), loaded into a plastic tray, and placed underneath a narrowband 9 W UVB lamp with peak emission at 311 nm (Philips PL-S 9W/01/2P). A box was placed over the bulb and sample tray to reduce ambient light exposure. All experiments were conducted with the tray the same distance from the bulb.

At set times after commencement of UVB irradiation, triplicate sample vials were removed and the mixture placed into 1.5 mL polypropylene microcentrifuge tubes, which were kept in the dark. At the termination of UVB exposure, the samples were centrifuged at 10 000 RCF for 5 min to remove the ITO nanoparticles from suspension. From the supernatant of each vial, 200 μL was pipetted into a black 96-well plate. The fluorescence of the product TPOH in the supernatant was determined with a Biotek Synergy HT microplate reader, with 360/40 excitation filter and 460/40 emission filter. Although these filters are not centered on the peak excitation and emission wavelengths for TPOH of 312 nm and 426 nm, respectively, enough fluorescence was detected to differentiate the behaviors of the different ITO types. Following fluorescence measurements, the supernatants were removed from the 96-well plates, added to a 10 mm quartz cuvette, and [TPA] determined on an Agilent 8454 UV-Vis spectrophotometer. No significant changes

in [TPA] were observed in any experiments.

4.3 Results and discussion

4.3.1 Batch dissolution

The batch dissolution experiment was run for a total of 36 d. Figure 4.1 depicts the aqueous concentration of Sn(IV) (solid line) in equilibrium with crystalline SnO_{2(c)} (cassiterite) as determined by Rai et al.¹¹⁸ in addition to the limits of detection (LOD) for the ICP-MS analyses (dot-dash lines) and ITO samples with dissolved Sn concentrations above the LOD (points) in this study. It is important to note that an estimate for the true value of the hydrolysis constant that dictates the horizontal portion of the solubility curve in Figure 4.1 has yet to be determined — the value of the hydrolysis constant for $\text{Sn}^{4+} + 4\text{H}_2\text{O} \rightleftharpoons \text{Sn}(\text{OH})_{4(\text{aq})} + 4\text{H}^+$ was reported as $\log_{10} K_{h14}^0 \leq -0.62$ in Rai et al. due to the LODs of Sn determination with ICP-MS ($\log_{10} \text{Sn} = -9.0, -8.0, \text{ and } -8.9$).¹¹⁸ Similar LODs were attained in this study ($\log_{10} \text{Sn} = -9.0$ and -9.3).

Of the 18 samples analyzed for Sn, 14 were below the LOD. Although a handful of samples had detectable Sn, the concentrations were within about $2 \times \text{LOD}$ in all cases. Regardless of whether the detections were real, they all occurred near the proposed limit of solubility of SnO_{2(c)}, which suggests that SnO_{2(c)} is likely the equilibrium-determining solid Sn phase for ITO. Thus, Sn in ITO appeared to behave similar to pure phase SnO_{2(c)} when exposed to aqueous solutions, but detection limits precluded differentiation of the relationship between solid Sn level and aqueous Sn concentrations.

To see whether the systems had achieved equilibrium, the concentration of aqueous In was plotted versus time for $\text{pH}_i = 4$ and $\text{pH}_i = 6$, as shown in Figures 4.2a and 4.2b, respectively. Figure 4.2a clearly shows the system had not reached, but was approaching, equilibrium for all ITO types at $\text{pH}_i = 4$ at 35 d, whereas the system may have reached

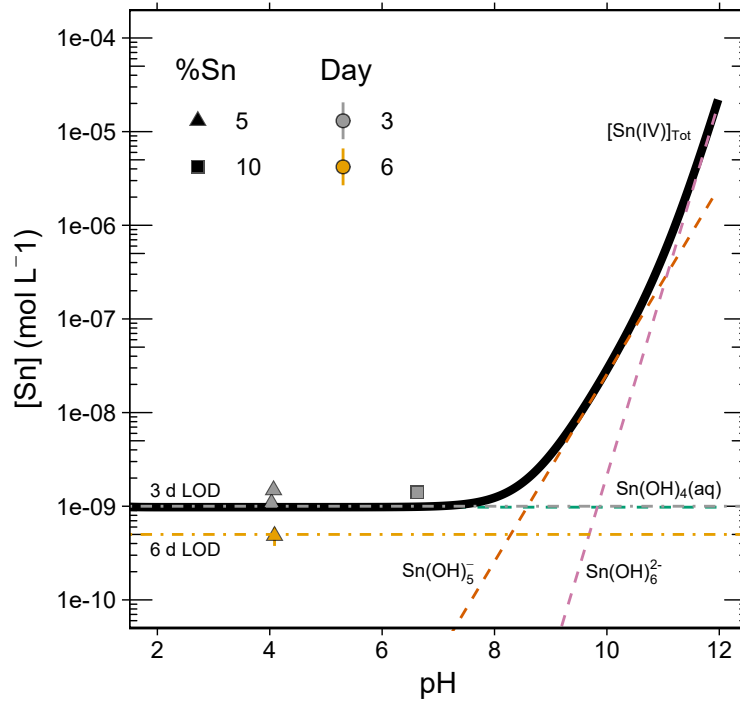


Figure 4.1: Sn concentrations in filtrates (points) that were greater than the LOD (dot-dashed lines; grey (top): 3 d samples, orange (bottom): 6 d samples). No 35 d samples had a detectable Sn concentration. The solid black line represents total dissolved Sn(IV) concentration in equilibrium with bulk crystalline SnO₂ (cassiterite) and is the summation of the Sn(OH)_m^{4-m} concentrations. Note the Sn(OH)_{4(aq)} line is concurrent with the 3 d LOD line.

equilibrium at $\text{pH}_i = 6$, as evidenced by the more linear nature of concentrations in Figure 4.2b. Although the systems were possibly not yet at equilibrium, the behaviors over time were consistent, enabling subsequent comparisons among Sn doping levels.

Kinetics of batch dissolution of solid phase particles that approach equilibrium are often modeled by the Noyes-Whitney equation:¹⁰⁶

$$C(t) = C^{\text{sat}}(1 - e^{-kt}) \quad k = \frac{A_{\text{surf}}D}{V_{\text{solution}}\delta} \quad (4.3)$$

where C^{sat} is the saturation concentration, A_{surf} is the exposed surface area of the particle, D is the diffusivity of the dissolving species, V_{solution} is the solution volume, and δ is the diffusion layer thickness. In this study, δ , V_{solution} and D are all constant for a given pH. Further models, such as the shrinking sphere model, have been used in the differential form of Equation 4.3 to incorporate the effect of the change of A_{surf} as dissolution proceeds. To assess whether the differences in concentrations among the ITO types in Figure 4.2 are from differences in surface area, the initial rates of dissolution were estimated as a line from the origin to the first points and normalized by the BET surface area. The BET surface areas for the 0%, 5%, and 10% ITO were $10 \text{ m}^2 \text{ g}^{-1}$, $11 \text{ m}^2 \text{ g}^{-1}$, and $9 \text{ m}^2 \text{ g}^{-1}$ as discussed in Chapter 3. Normalization of the initial rates at $\text{pH}_i = 4$ by the BET surface areas gives $r_i = 5.2 \times 10^{-8} \text{ mol g L}^{-1} \text{ m}^{-2}$, $7.6 \times 10^{-8} \text{ mol g L}^{-1} \text{ m}^{-2}$, and $6.9 \times 10^{-8} \text{ mol g L}^{-1} \text{ m}^{-2}$ for 0%, 5%, and 10% ITO, respectively. Normalization would bring the 5% and 10% ITO closer together in Figure 4.2a, both substantially higher than the 0%.

Figure 4.3 depicts the dissolved In concentrations from the 35 d samples for all ITO types. The two dashed lines represent the aqueous In(III) concentration in equilibrium with $\text{In}_2\text{O}_{3(\text{s})}$ and $\text{In}(\text{OH})_{3(\text{s})}$ using suggested solubility and hydrolysis constants from Brown and Ekberg¹²⁸ and Wood and Samson,¹²⁹ respectively. Values below the

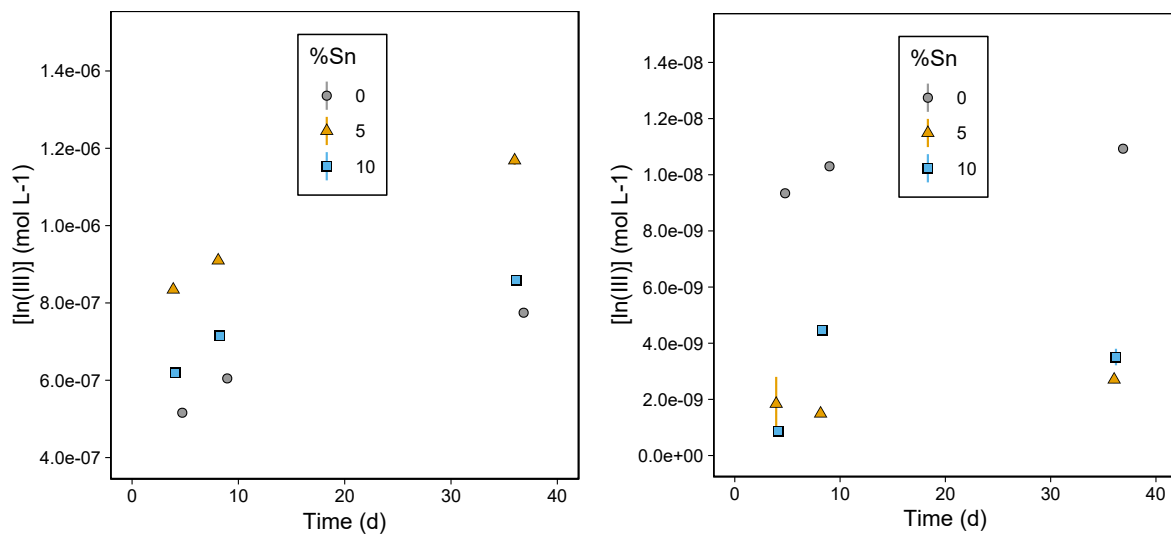


Figure 4.2: Concentration of dissolved In over time at (left) pH_i = 4 and (right) pH_i = 6. Note the difference in ordinate scale. Error bars represent relative standard deviation of triplicate injections of the same sample on ICP-MS and are obscured by the point in most cases.

line are undersaturated with respect to the solid phase (i.e., solid dissolution is thermodynamically favorable), and values above are oversaturated (i.e., thermodynamically favorable to precipitate).

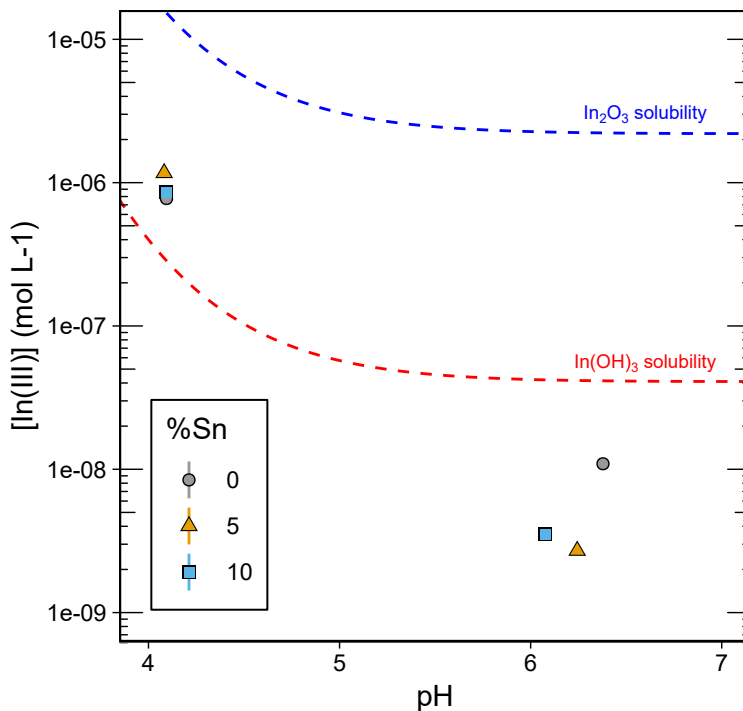


Figure 4.3: Dissolved In concentrations of batch dissolution experiment plotted against the final pH of the suspension at sampling time. Dashed lines represent the concentration of In that would be in equilibrium with In_2O_3 (blue) and $\text{In}(\text{OH})_3$ (red). Error bars are the relative standard deviation from triplicate injections of the same solution into the ICP-MS and are obscured by the point in most cases.

Several observations can be made with respect to the data in Figures 4.2 and 4.3. First, at $\text{pH}_i = 6$, the In_2O_3 (0% ITO) and the 5% and 10% ITO nanoparticles investigated in this study appear to be less soluble than $\text{In}(\text{OH})_3$. This result may be due to uncertainty in the estimates for $(\log_{10}^* K_{s10} = 5.06 \pm 0.10)^{128}$ or $\log_{10} K_{h13} = -12.4$ (no uncertainty given),¹²⁹ or the approach to equilibrium is slow at this pH. Second, the aqueous concentration of In for all ITO types at $\text{pH} = 4$ were slightly higher than

would be expected in equilibrium with $\text{In}(\text{OH})_{3(\text{s})}$, which could again be due to uncertainty in the estimates for the hydrolysis constants. Moreover, both groups of points indicate equilibrium aqueous In concentrations are likely dictated by the solubility of lesser soluble $\text{In}(\text{OH})_{3(\text{s})}$, not $\text{In}_2\text{O}_{3(\text{s})}$. Lastly, both 5% and 10% ITO exhibit markedly lower aqueous In concentrations than 0% ITO at $\text{pH}_i = 6$, while 5% ITO showed greater solubility than 0% and 10% ITO at $\text{pH}_i = 4$.

It is clear from the last point above that inclusion of Sn in the In_2O_3 crystal to form ITO changes the solubility from that of pure In_2O_3 . However, the difference in behavior between $\text{pH} = 6$ and $\text{pH} = 4$ is an interesting result. If one assumes Sn is isomorphously and fairly homogeneously substituted for In, one would assume the associated aqueous solubility of In and Sn in ITO may follow that of an ideal solid solution of $\text{In}_2\text{O}_{3(\text{s})}$ and $\text{SnO}_{2(\text{s})}$. If this were the case, the minor constituent (Sn) would exhibit markedly decreased aqueous solubility, while only a minor decrease in solubility would be observed for the major constituent (In).¹³⁰ This hypothesis could partially explain the decreased aqueous In concentrations observed at $\text{pH}_i = 6$, but one would expect a concomitant decrease in In concentrations at $\text{pH}_i = 4$. Thus, the data from this study suggest ITO does not behave like an ideal solid solution in regards to aqueous solubility.

Preferential leaching from mixed metal oxides, also known as incongruent dissolution, definitely occurred at all time points at $\text{pH}_i = 4$, since $[\text{In}]/[\text{Sn}] > C_{\text{In},\text{solid}}/C_{\text{Sn},\text{solid}}$. The LOD limitations for Sn make an assessment of whether incongruent dissolution also occurred at $\text{pH}_i = 6$ difficult. For 5% and 10% ITO, $[\text{In}] = 2 \times 10^{-8} \text{ mol L}^{-1}$ and $[\text{In}] = 1 \times 10^{-8} \text{ mol L}^{-1}$, respectively, would be the dissolved concentration for congruent dissolution if $[\text{Sn}] = 1 \times 10^{-9} \text{ mol L}^{-1}$ (the LOD), but the aqueous concentrations of In for 5% and 10% were $< 5 \times 10^{-9} \text{ mol L}^{-1}$. Thus, the ICP/MS LOD for Sn prohibits determination of the congruency of dissolution at $\text{pH}_i = 6$.

Slight restructuring of bond lengths upon Sn doping¹³¹ and dissociative chemisorption of O₂ and H₂O has been shown through first-principal calculations.¹³² Hydroxylation of clean In₂O₃ or ITO surfaces after exposure to water vapor or aqueous systems has also been shown experimentally.^{133–137} Increased dissolution of In from ITO at pH = 4 and decreased dissolution at pH = 6 relative to In(OH)_{3(s)} and In₂O_{3(s)} possibly suggests different In–O bond energies or abilities of protons to approach the surface for proton-promoted dissolution. The p.z.c. of SnO₂ occurs at about pH = 4,⁹⁴ so the majority of surface Sn atoms may be hydroxylated and hold a neutral charge. This may enable proton adsorption to sites near the terminal –SnOH group or cause a weakening of nearby In–O bonds that would be more susceptible to proton-promoted attack and subsequent In release.¹³⁸ At pH = 6, surface Sn are likely oxygen terminated and hold a negative charge, –SnO[–]. The difference in charge of surface Sn groups could possibly strengthen nearby In–O bonds, making them more resistant to proton-promoted dissolution, or weaken the ability of proton-promoted dissolution at nearby sites due to favorable interaction between –SnO[–] and –InOH₂⁺. Whatever the mechanism may be, this study shows prediction of ITO dissolution behavior is not a straightforward weighted average of dissolution behavior of the mole fraction of the binary end-members SnO₂ and In₂O₃ as would be the case in an ideal solid solution.

4.3.2 Dissolution monitored by flow-through AFM

Monitoring of the dissolution of 5% ITO at pH = 4 was the focus of the AFM study, as this condition showed the highest dissolution rate in the batch study. A fluid flow rate of 0.5 mL min^{–1} was maintained through the flow cell for 6 d except during imaging events to ensure a strong gradient for dissolution. The volume of the flow cell is roughly 100 μ L, which corresponds to replenishment of the fluid in the cell every 12 s. Figure 4.4 shows 2.2 μ m \times 2.2 μ m images of the same particles at the start of the

experiment (Day 0, Fig. 4.4a) and at 6 d (Fig. 4.4b). The experiment continued for an additional 8 d, but degraded image quality made these images too difficult to analyze with confidence. As a result, the experiment was terminated after 8 d, as image quality was unlikely to improve with additional time.

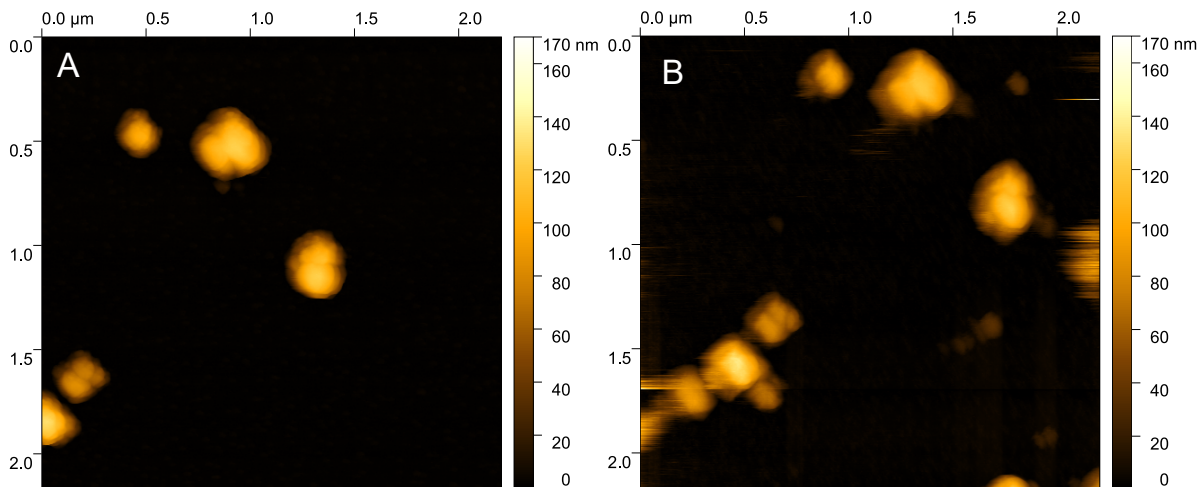


Figure 4.4: Topographical height images of 5 percent ITO on mica in $10 \text{ mmol L}^{-1} \text{ NaNO}_3$ at $\text{pH} = 4$ at (a) the start of the flow-through experiment and (b) after 6 d of 0.5 mL min^{-1} flow through the fluid cell. Images were acquired with a Bruker DNP-10 “A” cantilever using PeakForce QNM at a scan rate of 1.0 Hz with 512 samples/line and a PeakForce Setpoint of 0.3 V

Several differences between the 0 d and 6 d images are worthy of note. First 6 d image clearly had more artifacts (e.g., lines) due to diminishing tip cleanliness and entrapment of small air bubbles behind the cantilever. Image artifacts made automatic processing of images difficult without further adjustments to the image, which may result in changes to the extracted particle heights. Thus, particles were manually identified and matched among images. Second, smaller particles appeared after the first day of the experiment. For example, the small particle at $(1.75 \text{ } \mu\text{m}, 0.25 \text{ } \mu\text{m})$ in Figure 4.4b first appeared in the 1 d image and had a maximum height of about 35 nm. These particles may be particles from the fluid source or may be primary ITO particles that

were dislodged and transported to their locations when the flow was pulsed to remove air bubbles from the flow cell. However, since the source of these particles could not be positively known, they were not used in analyses of ITO dissolution kinetics. The final difference of note between Figures 4.4a and 4.4b is the roughness of the mica surface. The 0 d image exhibited a root mean square (RMS) surface roughness of about 0.60 nm, while subsequent images, starting at 1 d, had RMS roughnesses of 0.85 nm to 1.0 nm. The RMS roughness of the mica surface was used as an estimate of uncertainty in particle height measurements.

A low PeakForce Setpoint was used to reduce the force of tip-sample interaction to prevent the tip from moving or picking up particles while scanning. The low setting for PeakForce Setpoint also made the nanoparticle clusters appear “fluffy,” making identification of individual particles within clusters difficult. Thus, the maximum height of each cluster instead of individual particles was used to monitor dissolution. Figure 4.5 depicts the change in particle heights for the five particles in Figure 4.4a from the initial particle height measured at 0 d. The slope of the linear regression was found to be $(-0.24 \pm 0.16) \text{ nm d}^{-1}$ with a p -value of 0.149, indicating it was not significantly different than 0 nm d^{-1} . Thus, the kinetics of 5% ITO dissolution at $\text{pH} = 4$ in inert electrolyte were too slow to be quantified using flow-through AFM imaging in the 6 d time period investigated, corroborating the findings from the batch experiments. Images collected at longer time points showed poor image quality likely due to reduced tip cleanliness and bubble entrapment behind the cantilever. These images required further image cleaning, causing peak height determinations to be less reliable, and were therefore not used in the present analysis. However, this method may be useful to investigate the effects of various capping or aqueous ligands on mixed-metal oxide dissolution rates in future studies, similar to a recent study on capping effects on nano-Ag dissolution.¹²

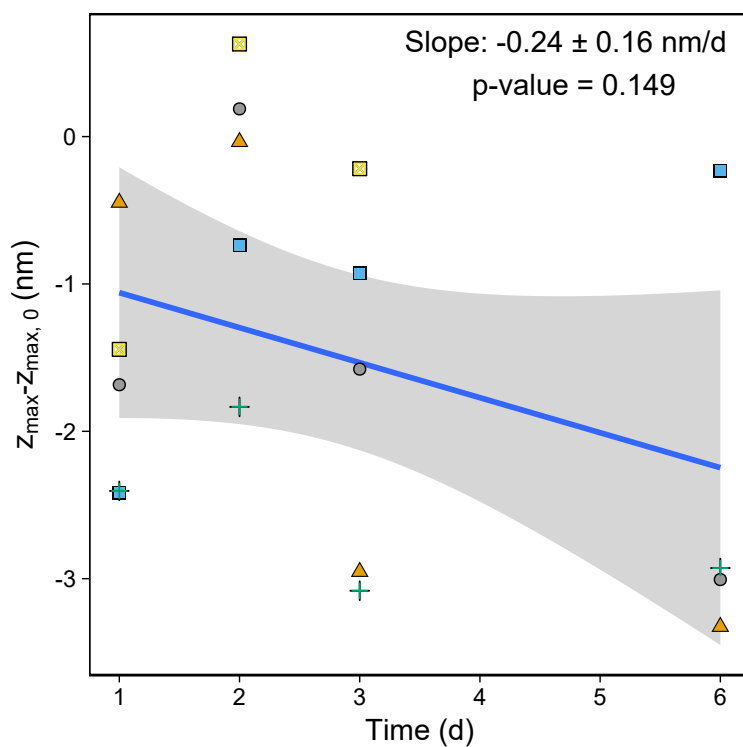


Figure 4.5: Difference of particle height, z_{max} , from initial height as measured at 0 d, $z_{max,0}$, for 5% ITO in 10 mmol L^{-1} at $\text{pH} = 4$. The five particles in Figure 4.4a were used and are each represented by a unique combination of shape and color. Note one particle was not included in the 6 d sampling due to interference of image artifacts in determining z_{max} for that particle.

4.3.3 Apparent optical band gap

The reflectance spectra of the ITO nanopowders and associated Kubelka-Munk determinations of $E_{g,opt}$ are shown in Figure 4.6. The values determined for $E_{g,opt}$, represented by a vertical black line in the figure, were 3.64 eV, 3.70 eV, and 3.74 eV for 0 %, 5 %, and 10 % ITO, respectively. These values match well with those found in literature for thin film and nanoparticulate ITO¹³⁹ and In_2O_3 .¹⁴⁰

For all ITO types, $E_{g,opt} < 3.99$ eV, which is the peak intensity of the UVB lamp used in hydroxyl radical photogeneration experiments. Thus, each type of ITO would be able to absorb UVB photons to make photogenerated e^-h^+ pairs. However, UVA photons, usually considered to have energies of 3.94 eV to 3.26 eV and are far more abundant in ambient sunlight, would only be absorbed if $h\nu_{\text{UVA}} > E_{g,b}$. Thus, absorption of ambient sunlight and subsequent photogeneration of reactive oxygen species by bare ITO nanoparticles is unlikely in environmental aqueous conditions.

4.3.4 Dry particle electron band energetics

Work functions, $\phi = E_{\text{vac}} - E_{\text{F}}$, of $\phi_0 = 4.05$ eV, $\phi_5 = 4.33$ eV, and $\phi_{10} = 4.33$ eV for 0 %, 5 %, and 10 % ITO, respectively, were determined from the half height of the secondary electron cutoff of the UPS spectra. The value of the energy difference between the Fermi level and the valence band maximum (VBM), $E_{\text{F}} - E_{\text{VBM}}$, was estimated from the intersection of a linear extrapolation of the valence band onset to the baseline. For all particle types, $E_{\text{F}} - E_{\text{VBM}} \approx 3.0$ eV.

In an intrinsic semiconductor, the fundamental band gap is given by $E_{g0} = E_{\text{CBM}} - E_{\text{VBM}}$, where CBM refers to conduction band minimum, and E_{F} lies somewhere between E_{CBM} and E_{VBM} . Typically, the optical band gap of intrinsic semiconductors matches that of the fundamental band gap, $E_{g,opt} = E_{g0}$. In a degenerate semiconductor such

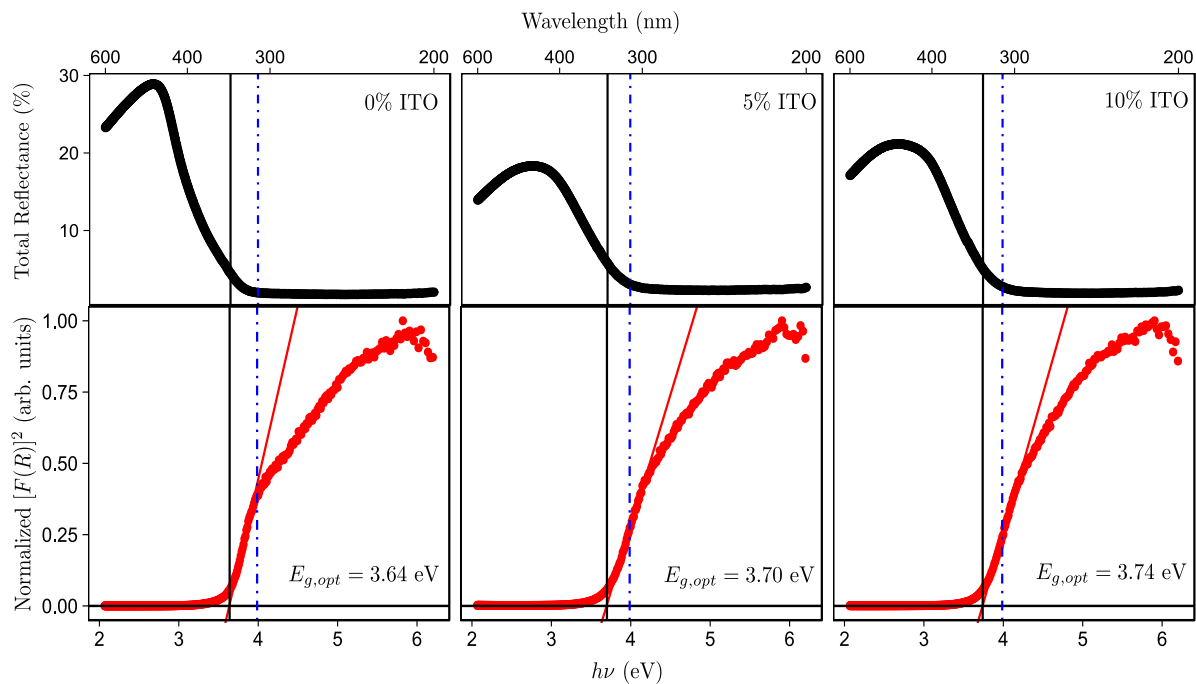


Figure 4.6: Total reflectance (top panel) and Kubelka-Munk transformations (bottom panel) of UV-Vis reflectance spectra. The vertical black lines are the $E_{g,opt}$ determined as intercepts with the abscissa on the bottom panel. The vertical blue dot dash lines is the wavelength of peak intensity of the UVB lamp used in experiments to determine photocatalytic generation of hydroxyl radicals.

as ITO, enough dopants are in the crystal to cause the Fermi level to rise to an energy level above that of E_{CBM} , causing population of the conduction band with electrons between E_F and E_{CBM} .⁹ Thus, the minimum energy required to promote an electron from the valence band to the conduction band is $h\nu > E_F - E_{VBM} > E_{CBM} - E_{VBM}$. In the case of In_2O_3 and ITO, however, experimental and modeling results have indicated that the fundamental band gap is about $E_{g0} \approx 2.9$ eV, significantly less than the optical band gap of $E_{g,opt} \approx 3.6$ eV. Reasons for this difference are parity-forbidden transitions at the VBM at the Γ point¹⁴¹ and possible Fermi-level pinning and associated surface band-bending.¹⁴⁰ Electrons from roughly 0.8 eV below the VBM are associated with the onset of strong photon absorption, both in pure In_2O_3 and ITO.¹⁴¹ Thus, photogenerated holes would have an energy roughly 0.8 eV more negative (with respect to vacuum), or more oxidizing, than E_{VBM} , resulting in energetics more favorable to hydroxyl radical production. At the same time, it means photons need 0.8 eV more energy to promote an electron, making photon absorption from ambient sunlight much less likely.

Figure 4.7 combines the $E_{g,opt}$ estimated from diffuse reflectance data with the estimated I_p and ϕ for 0%, 5%, and 10% ITO in relation to possible pathways for nanoparticle-associated toxicity. In a study of 24 single metal oxides, Zhang et al. found that a calculated CBM energy of -4.84 eV $< E_{CBM} < -4.12$ eV (grey rectangle in Fig. 4.7) correlated to inflammation and oxidative stress of pulmonary cells due to disruption of the electron-transport systems within the cell.¹³ The same research group found similar results for toxicity in *E. coli*,¹⁴ and other researchers correlated antibacterial activity of metal oxide nanoparticles to production rates of reactive oxygen species (ROS), the redox potentials of which are included as dashed lines in Figure 4.7 for aerated water at pH = 5.6. As dry nanopowders, it would appear all ITO nanoparticles investigated could lead to CBM-related toxicity, since the CBM of each particle is likely within the

cellular redox window. Additionally, each nanoparticle has the thermodynamic capability to oxidize water to produce hydroxyl radicals (OH^\bullet) since $E_{\text{VBM}} < E_{\text{H}_2\text{O}/\text{OH}^\bullet}$ with respect to E_{vac} .

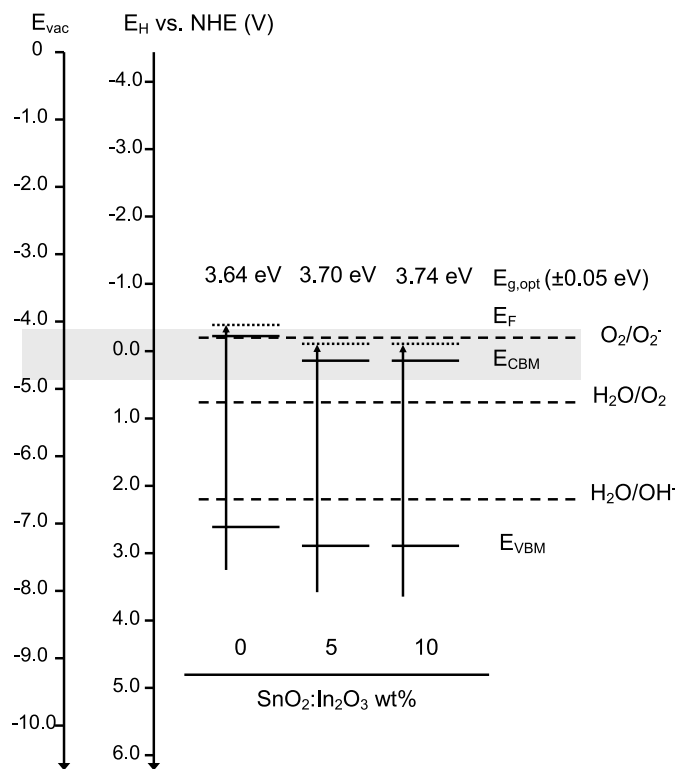


Figure 4.7: Estimated band structure of 0%, 5%, and 10% ITO from UV-Vis diffuse reflectance spectroscopy and UPS measurements. The values for E_{CBM} are approximate — each assumes a 0.8 eV offset from E_{VBM} for the onset of significant absorption. The arrows indicate promotion of valence band electrons through absorption of a photon of energy $h\nu = E_{g,\text{opt}}$, the dotted lines are the E_{F} of the particles, and the solid lines are the VBM and CBM. The grey box indicates the cellular redox window,¹³ and the dashed lines represent redox potentials at pH = 5.6 for ROS species of interest.¹⁵

4.3.5 Hydroxyl radical production

The band structure proposed in Figure 4.7 suggests that 0%, 5%, and 10% ITO are all thermodynamically capable of producing OH^\bullet under UVB irradiation in contact with water. To test whether thermodynamics were the controlling factor in photogener-

ation of OH^\bullet , i.e., whether one can rely solely on band energetics for prediction of ROS production, an assay utilizing the TPA fluorescence probe was used.

The concentration of TPA required to measure the hydroxyl radical production rate was determined by adjusting the final concentration of TPA in the mixture irradiated with UVB. Figure 4.8 depicts the fluorescence of the supernatant after 20 min of UVB irradiation as a function of the total concentration of TPA ($[\text{TPA}]_{\text{T}} = [\text{H}_2\text{TP}] + [\text{HTP}]^- + [\text{TP}]^{2-}$). The pH of solution during UVB irradiation and fluorescence measurements of these samples was $\text{pH} = 6.2 \pm 0.1$ and $C_{\text{ITO}} = 25 \text{ mg L}^{-1}$. Since $\text{p}K_{\text{a}2} = 4.81$ for terephthalic acid, $[\text{TP}^{2-}] = 0.93[\text{TPA}]_{\text{T}}$ at $\text{pH} = 6.0$ and $[\text{TP}^{2-}] = 0.99[\text{TPA}]_{\text{T}}$ at $\text{pH} = 6.8$, meaning nearly all TPA was present as the active divalent anion terephthalate (TP) during these experiments.

From the results shown in Figure 4.8, a TPA concentration of 0.5 mmol L^{-1} was chosen for subsequent experiments. Under the pseudo steady-state assumption for $[\text{OH}^\bullet]$, the plateau in fluorescence at larger concentrations of TPA indicates the rate of hydroxylation of TPA is limited by the rate of production of hydroxyl radicals, e.g., $r = k' = k[\text{OH}^\bullet]$, whereas the large difference in fluorescence at lower TPA concentrations indicates the hydroxylation reaction rate is also dependent on the concentration of TP, e.g., $r = k'[\text{PA}]^{2-} = k[\text{OH}^\bullet][\text{PA}]^{2-}$.¹²⁵ The fluorescence at $[\text{TPA}]_{\text{T}} = 0.5 \text{ mmol L}^{-1}$ was within 5% of that observed at $[\text{TPA}]_{\text{T}} = 1.0 \text{ mmol L}^{-1}$ for 10% ITO at a given vial location. The fluorescence of 0% and 5% ITO were significantly lower, but similar plateau behavior was also observed by $[\text{TPA}]_{\text{T}} = 0.4 \text{ mmol L}^{-1}$. A difference in fluorescence between the middle vial location along the centerline of the UVB bulb and vials on either side of the centerline was observed. The discrepancy is due to differences in incident intensity, so subsequent discussion will focus on comparisons of vials in the same position. i.e., same incident light intensities.

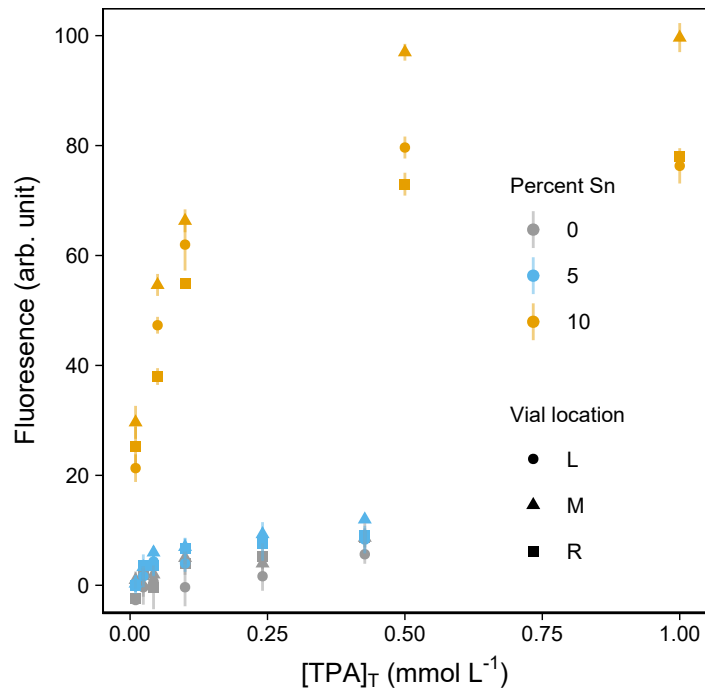


Figure 4.8: Relative fluorescence of supernatant after 20 min UVB irradiation as a function of total terephthalic acid concentration. Error bars represent the standard deviation of fluorescence from triplicate aliquots from a single irradiated vial. Each point had $[\text{NaCl}] = 10 \text{ mmol L}^{-1}$ and $C_{\text{ITO}} = 25 \text{ mg L}^{-1}$ during UVB irradiation. Vial location refers to relative location of the irradiated vial to the centerline of the UVB bulb when viewed from above: L is to the left, M is on the centerline, and R is to the right.

Since $[\text{TPA}]_{\text{T}}$ was chosen such that the rate of hydroxyl radical production was the limiting step (i.e., pseudo-first order conditions), direct comparison of fluorescence measurements could be made to compare relative hydroxyl production rates among experimental conditions, according to Equation 4.4, where k' is the slope of the fluorescence vs. time plot. The relative rates of hydroxyl radical production among ITO are shown in Figure 4.9 and summarized in Figure 4.10.

$$\frac{d\text{TPOH}}{dt} = k[\text{OH}^{\bullet}]_{(aq)}^{\alpha}[\text{TP}^{2-}]^{\beta} \approx k[\text{OH}^{\bullet}]_{(aq),ss} = k' \quad (4.4)$$

Figure 4.9 depicts the fluorescence response at approximate initial pHs of 6 (Fig. 4.9a) and 9 (Fig. 4.9b) as a function of UVB irradiation time for all ITO suspensions investigated. pH 6 was chosen to investigate the ROS production behavior at an environmentally relevant pH where the ITO particles were stable in the background electrolyte (10 mmol L⁻¹ NaCl). On the other hand, pH 9 was near the isoelectric point of the ITO particles, so the particles were likely to aggregate during the experiment. A previous study showed that diffusion-limited aggregate structure, like that which would be formed near pH = 9 for ITO particles, did not decrease the generation rate of free OH[•], likely due to the ability of photogenerated OH[•] to diffuse out of the open structure.¹⁴² Thus, the free OH[•] generation rate would not be significantly inhibited by mass transfer at pH = 9 in this study, enabling elucidation of the affect of pH on photogeneration rate. Theoretically, two main differences between pH = 6 and pH = 9 as it relates to OH[•] production exist: (1) The higher pH could lead to more adsorbed OH⁻ on the particle surface, increasing the rate of $\text{OH}_{\text{ads}}^{-} + \text{h}^{+} \longrightarrow \text{OH}_{\text{ads}}^{\bullet}$, and (2) the Fermi level of the surface states becomes less negative with respect to vacuum, causing the thermodynamic drive for hole production to decrease.

From Figure 4.10, 10 % ITO clearly exhibits significantly higher photogeneration

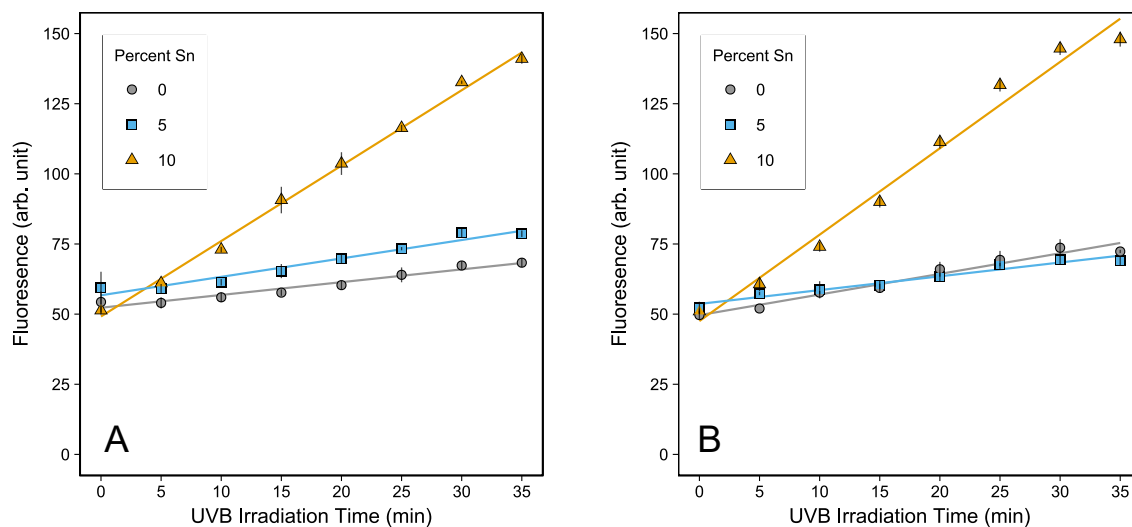


Figure 4.9: Fluorescence of supernatant following UVB irradiation of dispersions containing $C_{\text{ITRO}} = 25 \text{ mg L}^{-1}$, $[\text{TPA}]_{\text{T}} = 0.5 \text{ mmol L}^{-1}$, and $[\text{NaCl}] = 10 \text{ mmol L}^{-1}$ at (a) $\text{pH}_i = 6$ and (b) $\text{pH}_i = 9$. All points were from the centerline under the UVB lamp (position M).

rates of hydroxyl radicals than 0% or 5% ITO at both $\text{pH}_i = 6$ and $\text{pH}_i = 9$. Furthermore, 0% and 5% ITO do not have significantly different hydroxyl photogeneration rates for the same experimental conditions. Lastly, only 0% ITO showed a significant difference (increase) in hydroxyl production rate at $\text{pH}_i = 9$ when compared to $\text{pH}_i = 6$. If one were to predict hydroxyl production capabilities solely based on E_{VBM} , all three ITO types would have had similar rates, since all had thermodynamically favorable energetics. However, these results indicate the energy level of the VBM and CBM do not adequately explain the photocatalytic activity of the different ITO nanoparticles to produce hydroxyl radicals — band-bending or specificity of surface sites for hole transfer to OH^- or H_2O must also play an important role, as evidenced in the significantly different production rates exhibited by the 10% ITO.

4.3.6 Environmental implications

This study demonstrated that dissolution behavior, the energy level of the conduction band, and photocatalytic ability for hydroxyl radical production for different levels of Sn doping in ITO nanoparticles cannot be predicted from the two binary oxide end members, In_2O_3 and SnO_2 . Over a 35 d period, indium was leached from ITO at concentrations greater than solubility at $\text{pH} = 4$, but less than solubility at $\text{pH} = 6$, behavior that does not fit well within established theories on dissolution of solid solutions. Furthermore, from the electronic band structures determined for dry nanopowders, photocatalytic production of hydroxyl radicals was thermodynamically favorable for 0%, 5%, and 10% ITO. However, 10% ITO produced hydroxyl radicals at a significantly higher rate.

The inability to predict the behaviors of mixed metal oxides based on the binary metal oxide end-members presents a unique challenge when attempting to predict the

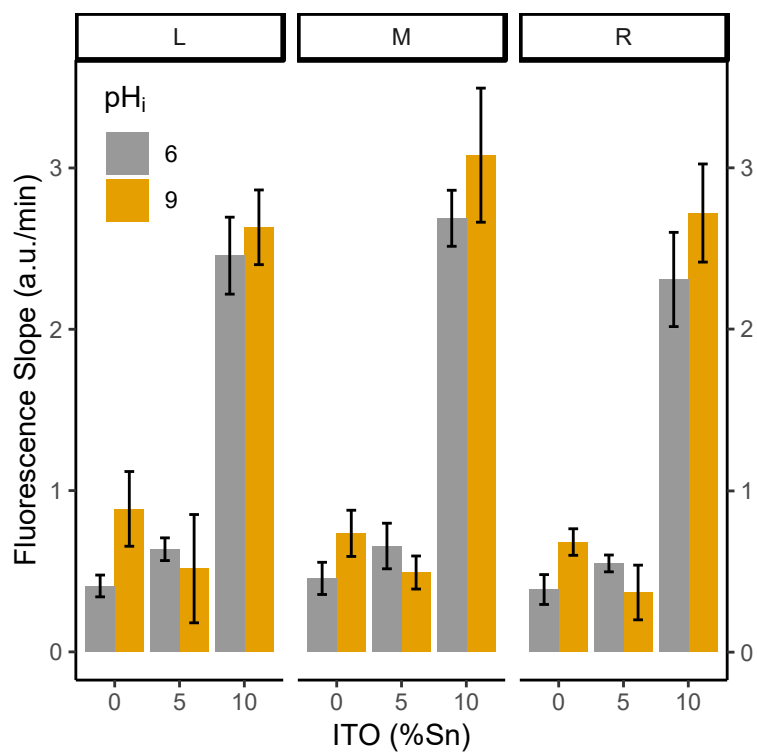


Figure 4.10: Slopes of ordinary least squares linear fit of fluorescence versus UVB irradiation time. Error bars signify a 95% CI on the slope regression parameter. The values L, M, and R refer to relative location of the irradiated vial to the centerline of the UVB bulb when viewed from above: L is to the left, M is on the centerline, and R is to the right.

fate and toxicity of these ENMs. Comprehensive studies have found metal release and the positions of electronic bands as significant predictors of cellular toxicity¹³⁻¹⁵ for binary metal oxide nanoparticles. However, this study showed that ITO, and thus other mixed metal oxides, may not behave as expected, and further study of more mixed metal oxides is needed to determine if or when environmental toxicity can be predicted from end member binary metal oxides.

Chapter 5

Conclusions and recommendations

5.1 Conclusions

The electronic band structure, aqueous suspension stability, dissolution behavior, and ability to photocatalytically produce ROS was investigated for ITO nanoparticles with varying Sn content to elucidate the role doping level plays in transport, transformation, and potential toxicity of ITO in aqueous environmental matrices. The major findings of this research are summarized below in relation to the research objective and tasks outlined in Chapter 1.

Effect of Sn level on electrolyte-induced homoaggregation

A novel method, the TAA-logistic method, for more accurate and precise estimation of the CCC from particle aggregation as monitored by DLS was developed to enable improved comparison of particle stability. Electrolyte-induced aggregation of ITO nanoparticles at near-neutral pH was monitored while changing the capping ligand, electrolyte type, and concentration of NOM to elucidate the effect doping level of Sn had on particle stability. Inclusion of Sn reduced particle stability from that of un-doped In_2O_3 , and the changes were primarily due to changes in surface charge. However, surface charge, and thus particle stability, was not a weighted combination of the binary ITO end-members, indicating the distribution of Sn within ITO crystals was also an important factor.

Effect of Sn level on aqueous dissolution in inert electrolyte

Batch dissolution experiments confirmed the low solubility of ITO at pH = 4 and pH = 6 in the presence of 5 mmol L⁻¹ NaClO₄. Slow kinetics were also confirmed using flow-through AFM dissolution experiments. At pH = 6, inclusion of Sn in In₂O₃ reduced the solubility of In relative to In₂O₃, but inclusion of Sn appeared to increase solubility of In over than of In₂O₃ at pH = 4. This behavior cannot be explained by ideal solid solution aqueous solution theory, which may suggest lattice distortions near the surface of ITO crystals can lead to more energetically favorable proton-promoted dissolution of In from the crystal surface. Thus, ITO dissolution cannot be predicted using simple theories on dissolution of solid solutions.

Modulation of band gap energetics

The estimated band structure of nanoparticulate ITO was constructed using UPS and UV-Vis diffuse reflectance spectra. From the estimated band energies, both ITO and In₂O₃ may exhibit toxicity through disruption of cellular processes, as E_{CBM} fell within the estimated cellular redox window. Furthermore, both Sn-doped and un-doped In₂O₃ would thermodynamically be able to produce hydroxyl radicals upon illumination with UVB, but not UVA, light through oxidation of water by photogenerated holes. However, a hydroxyl radical assay utilizing terephthalate as a hydroxyl scavenger showed significantly higher hydroxyl radical photogeneration rates under UVB illumination for 10 % Sn ITO than 5 % Sn ITO and un-doped In₂O₃. Since the electronic band energetics determined for 0 I, 5 I, and 10 ITO would suggest all three Sn doping levels would produce hydroxyl radicals upon UVB illumination, ROS production rates cannot be predicted solely from estimated electronic band structure — other factors, such as band bending and surface specificity for hole transfer, may play an important role in both photocatalysis

and toxicity pathways.

5.2 Environmental implications

None of the investigated properties related to environmental fate and transport of ITO could be predicted by considering ITO as an ideal homogeneous mixture of the two end-members, In_2O_3 and SnO_2 . Non-ideal or non-predictable behavior was observed in particle stability, solubility, and band energetics and associated routes of toxicity when these characteristics were investigated for various levels of Sn doping in ITO. Thus, other factors, such as crystal structure and strain, are likely important to the aqueous behavior of ITO nanoparticles. Since these material properties are not often considered when investigating the environmental fate, transport and toxicity of ENMs but are important for doped metal oxides, the associated environmental risk of doped metal oxides would be difficult to predict within the existing framework. Thus, more research on the aqueous behavior of ITO and other doped metal oxides is needed to help identify important material properties unique to doped metal oxides and expand the modeling and framework to include this class of ENMs.

5.3 Recommendations for future work

To expand upon the findings of this research, the following studies could be performed:

Effect of ligand type and/or length on ITO particle stability

The current study considered the effect of one type of capping ligand on stability of ITO nanoparticles in electrolyte solutions. It was clear the amount of tin was an important factor for the trend of particle stability. Another set of ligand-capped ITO

nanoparticles synthesized for this study was stable in electrolyte solution even at concentrations of $[\text{CaCl}_2] > 1 \text{ mol L}^{-1}$ regardless of Sn content. For this set of stable particles, the influence of Sn, and likely the entire ITO nanoparticle, was lost. This would indicate a core-shell type situation, where properties of the ligand (shell) can mask the properties of the nanoparticle (core). Investigation of the properties that cause shielding of the core, such as ligand length or charge density, could inform optimization of ligand type for both utility of the nanoparticle for the intended purpose while reducing possible environmental impacts.

Study of ligand-promoted dissolution of ITO

This research studied the solubility and dissolution kinetics of ITO in NaClO_4 , an indifferent electrolyte. Natural waters and internal environments of organisms contain other ions and molecules that could act as ligands or otherwise promote ITO dissolution. While some research has investigated ITO etching and dissolution in small organic acids, such as oxalic acid, little study has been done to quantify stability constants of In-ligand and Sn-ligand complexes of non-halide ligands. Recent research has shown increased solubility of ITO in some biological media, but the ligands causing the increase in dissolution were not investigated. Investigation of possible interactions of ITO with biologically-relevant ligands could inform future toxicity studies on cellular environments that may have increased risk of adverse affects from ITO exposure and dissolution.

Investigation of other industrially-relevant doped metal oxides

ITO was chosen in this study because it is a doped metal oxide that is already produced on a large scale. However, many other doped metal oxides have industrial potential. The results of this study indicated that behavior of ITO nanoparticles in aqueous media was unpredictable — predictability should also be assessed for other

doped metal oxides. Only one recent study has considered particle stability, dissolution, and toxicity for a doped metal oxide,¹⁶ and while many characteristics seemed to be a function of the relative amount of end-members, some unique behaviors were also observed. Thus, more study is needed on a more extensive set of doped metal oxides to see if trends in predictability emerge.

Appendix

Appendix A

Appendix for Chapter 2

A.1 Discussion of W relating to DLS measurements

Experimental determination of W from DLS data relies on estimating k_{fast} and k_{obs} from aggregation histories of a given experimental condition. It is important to note that Fuchs originally developed the concept of W by calculation of particle number fluxes in a diffusive force field. Thus, in the purest state, W is a measure of relative rates of particle number aggregation as monitored by changes in particle number. Dynamic light scattering monitors the increase in the intensity-averaged, apparent hydrodynamic radius (\bar{R}_{DLS}) over time. This value is often larger than the real hydrodynamic radius and is a complex function of primary particle size, optical parameters, as well as aggregate size and morphology. Conversion of an intensity-averaged, apparent hydrodynamic radius to volume- or number-average hydrodynamic radius requires knowledge of particle and cluster morphology, along with optical properties of the material; intensity-averaged data are usually used in analysis to avoid possibly erroneous assumptions.

As noted in the manuscript, the scaling method of determining W requires assumption of a functional form of $\bar{R}_{DLS}(t, W)$ and adjustment of W for each aggregation curve such that all curves align on a single master curve.^{58,64} The functional forms have typically been determined from simulations and numerical solutions to the Smoluchowski population balance equation assuming various aggregation kernels. Studies have found that in the diffusion-limited regime, $\bar{R}_{DLS} \propto (1 + t/t_p)^{z/d_f}$, where $t_p = 3\eta W/(4k_B T N_0)$ is the characteristic time of aggregation, $z \approx 1$, η is the fluid viscosity, k_B is the Boltzmann

constant, T is temperature, and d_f is the fractal dimension of the aggregate cluster, usually taken to be $d_f \approx 1.85$ for diffusion-limited aggregation.^{51,58,64} In the reaction-limited regime, $\bar{R}_{DLS} \propto \exp(t/t_p)$, so if $t \ll t_p$, which is typical in reaction-limited aggregation studies, $\bar{R}_{DLS} \propto t/t_p$ and the aggregation appears linear. Although this method has shown promise in determining W that match well with the linear-fitting method, some disagreement exists regarding the range of W in which each range applies. This paper seeks to develop a method that makes few assumptions during the data analysis process, and since the scaling method requires application of either a diffusion- or reaction-limited equation for \bar{R}_{DLS} to data that may not exhibit such behavior, it was not explored in this study.

A.2 Discussion of CCC

The aggregation process can be viewed as being controlled by two processes, mass transfer and reaction, or sticking. Equation A.1 describes the observed aggregation rate as two resistances in series.

$$\frac{1}{k_{obs}} = \frac{1}{k_r} + \frac{1}{k_{mt}} \quad (\text{A.1})$$

Multiplying Equation A.1 by k_{mt} and using the definition of W provided in Equation 2.1a, one arrives at Equation A.2. When $k_{mt} = k_r$, or when aggregation is equally limited by mass transfer and reaction, it follows that $W = 2$. In this paper, the CCC is defined as the point when $k_r = k_{mt} = k_{r,CCC}$, or $W = 2$, which gives the rightmost expression for W in Equation A.2. Thus, one can find an analytical or approximate

expression for W by assuming a functional form for $k_r(C_s)$

$$W = \frac{k_{mt}}{k_{obs}} = \frac{k_{mt}}{k_r} + 1 = \frac{k_{r,CCC}}{k_r} + 1 \quad (\text{A.2})$$

If one assumes a functional form of $k_r = C_1 C_s^\beta$, as originally posited by Reerink and Overbeek, substitution of $k_r = C_1 C_s^\beta$ and $k_{r,CCC} = C_1 CCC^\beta$ into Equation A.2 results in Equation 2.3a. This equation was used by Grolimund et al. to empirically fit $W(C_s)$ to find the CCC, but appeared to not have been used much subsequent studies.⁶³ This article demonstrates Equation 2.3a has a theoretical basis in DLVO theory. Furthermore, rearrangement and transformation of Equation 2.3a results in Equations A.3a and A.3b.

$$W^{-1} = \frac{1}{1 + CCC^\beta \exp(-\beta \ln C_s)} \quad (\text{A.3a})$$

$$\log W^{-1} = \log [1 + (CCC/C_s)^\beta] \quad (\text{A.3b})$$

Equation A.3a is a logistic function, with an inflection point at $W^{-1} = 0.5$ and $C_s = CCC$, with β affecting the sharpness of the curve around the inflection point. Equation A.3b exhibits linear behavior for both $C_s \ll CCC$ and $C_s \gg CCC$, which matches the current practice of the tangent method.

Equation A.2 can be used with any functional form of k_r . For example, one could use a form of k_r often assumed in collision theory, which takes the Arrhenius-like form $k_r = A \exp(-E_a/k_B T)$. If this is plugged Equation A.2, the result is Equation A.4

$$W = 1 + \exp\left(\frac{E_a - E_{a,CCC}}{k_B T}\right) \quad (\text{A.4})$$

which is also a logistic function when inverted. Regardless of the choice for the form of k_r , $W = 2$ at $C_s = CCC$ holds in this framework, which is desirable when estimating a CCC from experimental W data.

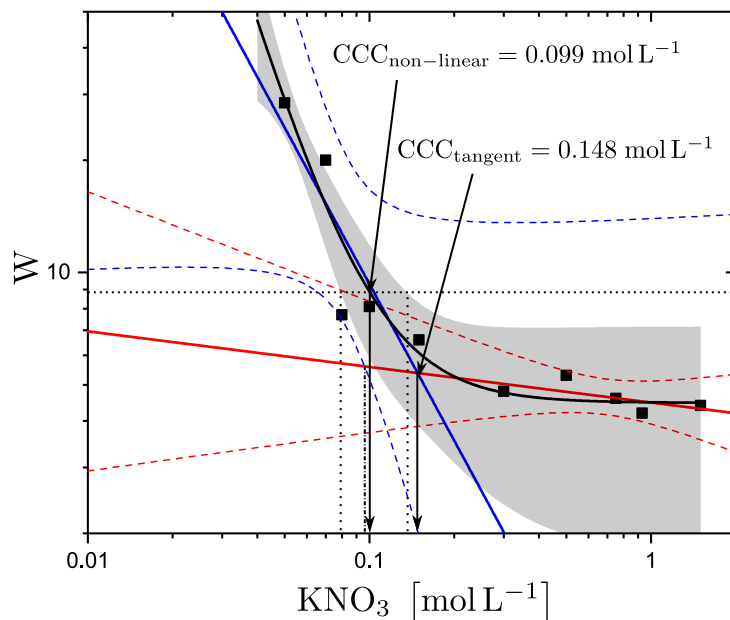


Figure A.1: Determination of the CCC from stability ratio data reported in [Kim and Berg](#) using the tangent method (solid blue and red straight lines) and fitting of $W = W_{min}[1 + (CCC/C_s)^\beta]$ (black solid). The rightmost 5 points were used for fitting the fast aggregation line (red), and the leftmost 5 points were used to fit the reaction-limited line (blue), as was done in the original study. The dashed lines around the linear fits and the ribbon around the non-linear fit are 95% confidence bands. The horizontal dashed line signifies $W/W_{min} = 2$, which is the location of the CCC. Dropped dotted lines (for non-linear) and dropped dash-dot line (tangent method) to the axis indicate the range of CCC estimates within the confidence bands. The upper bound for the tangent method is located out of the plotting bounds (i.e. $> 1.2 \text{ mol L}^{-1}$). The value of CCC reported in the original study was 0.16 mol L^{-1} .

Bibliography

- [1] Piccinno, F.; Gottschalk, F.; Seeger, S.; Nowack, B. Industrial production quantities and uses of ten engineered nanomaterials in Europe and the world. *J. Nanoparticle Res.* **2012**, *14*, 1109.
- [2] Vance, M. E.; Kuiken, T.; Vejerano, E. P.; McGinnis, S. P.; Hochella, M. F.; Hull, D. R. Nanotechnology in the real world: Redeveloping the nanomaterial consumer products inventory. *Beilstein J. Nanotechnol.* **2015**, *6*, 1769–1780.
- [3] Colvin, V. L. The potential environmental impact of engineered nanomaterials. *Nat. Biotechnol.* **2003**, *21*, 1166–1171.
- [4] Klaine, S. J.; Alvarez, P. J. J.; Batley, G. E.; Fernandes, T. F.; Handy, R. D.; Lyon, D. Y.; Mahendra, S.; McLaughlin, M. J.; Lead, J. R. Nanomaterials in the environment: behavior, fate, bioavailability, and effects. *Environ. Toxicol. Chem.* **2008**, *27*, 1825–1851.
- [5] Boyes, W. K.; Thornton, B. L. M.; Al-Abed, S. R.; Andersen, C. P.; Bouchard, D. C.; Burgess, R. M.; Hubal, E. A.; Ho, K. T.; Hughes, M. F.; Kitchin, K.; Reichman, J. R.; Rogers, K. R.; Ross, J. A.; Rygiewicz, P. T.; Scheckel, K. G.; Thai, S. F.; Zepp, R. G.; Zucker, R. M. A comprehensive framework for evaluating the environmental health and safety implications of engineered nanomaterials. *Crit. Rev. Toxicol.* **2017**, *47*, 767–810.
- [6] Petosa, A. R.; Jaisi, D. P.; Quevedo, I. R.; Elimelech, M.; Tufenkji, N. Aggregation

- and Deposition of Engineered Nanomaterials in Aquatic Environments: Role of Physicochemical Interactions. *Environ. Sci. Technol.* **2010**, *44*, 6532–6549.
- [7] Saleh, N. B.; Afrooz, A. R. M. N.; Bisesi, Jr., J. H.; Aich, N.; Plazas-Tuttle, J.; Sabo-Attwood, T. Emergent Properties and Toxicological Considerations for Nanohybrid Materials in Aquatic Systems. *Nanomaterials* **2014**, *4*, 372–407.
- [8] Saleh, N. B.; Milliron, D. J.; Aich, N.; Katz, L. E.; Liljestrand, H. M.; Kirisits, M. J. Importance of doping, dopant distribution, and defects on electronic band structure alteration of metal oxide nanoparticles: Implications for reactive oxygen species. *Sci. Total Environ.* **2016**, *568*, 926–932.
- [9] Klein, A.; Körber, C.; Wachau, A.; Säuberlich, F.; Gassenbauer, Y.; Harvey, S. P.; Proffit, D. E.; Mason, T. O. Transparent Conducting Oxides for Photovoltaics: Manipulation of Fermi Level, Work Function and Energy Band Alignment. *Materials (Basel)*. **2010**, *3*, 4892–4914.
- [10] Stadler, A. Transparent Conducting Oxides—An Up-To-Date Overview. *Materials (Basel)*. **2012**, *5*, 661–683.
- [11] Agrawal, A.; Cho, S. H.; Zandi, O.; Ghosh, S.; Johns, R. W.; Milliron, D. J. Localized Surface Plasmon Resonance in Semiconductor Nanocrystals. *Chem. Rev.* **2018**, *118*, 3121–3207.
- [12] Liu, C.; Leng, W.; Vikesland, P. J. Controlled Evaluation of the Impacts of Surface Coatings on Silver Nanoparticle Dissolution Rates. *Environ. Sci. Technol.* **2018**, *52*, 2726–2734.
- [13] Zhang, H.; Ji, Z.; Xia, T.; Meng, H.; Low-Kam, C.; Liu, R.; Pokhrel, S.; Lin, S.; Wang, X.; Liao, Y. P.; Wang, M.; Li, L.; Rallo, R.; Damoiseaux, R.; Telesca, D.;

- Mädler, L.; Cohen, Y.; Zink, J. I.; Nel, A. E. Use of Metal Oxide Nanoparticle Band Gap To Develop a Predictive Paradigm for Oxidative Stress and Acute Pulmonary Inflammation. *ACS Nano* **2012**, *6*, 4349–4368.
- [14] Kaweeteerawat, C.; Ivask, A.; Liu, R.; Zhang, H.; Chang, C. H.; Low-Kam, C.; Fischer, H.; Ji, Z.; Pokhrel, S.; Cohen, Y.; Telesca, D.; Zink, J.; Mädler, L.; Holden, P. A.; Nel, A.; Godwin, H. Toxicity of Metal Oxide Nanoparticles in *Escherichia coli* Correlates with Conduction Band and Hydration Energies. *Environ. Sci. Technol.* **2015**, *49*, 1105–1112.
- [15] Li, Y.; Zhang, W.; Niu, J.; Chen, Y. Mechanism of Photogenerated Reactive Oxygen Species and Correlation with the Antibacterial Properties of Engineered Metal-Oxide Nanoparticles. *ACS Nano* **2012**, *6*, 5164–5173.
- [16] Adeleye, A. S.; Pokhrel, S.; Mädler, L.; Keller, A. A. Influence of nanoparticle doping on the colloidal stability and toxicity of copper oxide nanoparticles in synthetic and natural waters. *Water Res.* **2018**, *132*, 12–22.
- [17] George, S.; Pokhrel, S.; Xia, T.; Gilbert, B.; Ji, Z.; Schowalter, M.; Rosenauer, A.; Damoiseaux, R.; Bradley, K. A.; Mädler, L.; Nel, A. E. Use of a Rapid Cytotoxicity Screening Approach To Engineer a Safer Zinc Oxide Nanoparticle through Iron Doping. *ACS Nano* **2010**, *4*, 15–29.
- [18] Xia, T.; Zhao, Y.; Sager, T.; George, S.; Pokhrel, S.; Li, N.; Schoenfeld, D.; Meng, H.; Lin, S.; Wang, X.; Wang, M.; Ji, Z.; Zink, J. I.; Mädler, L.; Castanova, V.; Lin, S.; Nel, A. E. Decreased Dissolution of ZnO by Iron Doping Yields Nanoparticles with Reduced Toxicity in the Rodent Lung and Zebrafish Embryos. *ACS Nano* **2011**, *5*, 1223–1235.

- [19] Ikeuchi, H.; Shibata, A.; Sano, Y.; Koizumi, T. Dissolution Behavior of Irradiated Mixed-oxide Fuels with Different Plutonium Contents. *Procedia Chem.* **2012**, *7*, 77–83.
- [20] Horlait, D.; Clavier, N.; Szenknect, S.; Dacheux, N.; Dubois, V. Dissolution of cerium(IV)-lanthanide(III) oxides: Comparative effect of chemical composition, temperature, and acidity. *Inorg. Chem.* **2012**, *51*, 3868–3878.
- [21] Tocino, F.; Szenknect, S.; Mesbah, A.; Clavier, N.; Dacheux, N. Dissolution of uranium mixed oxides: The role of oxygen vacancies vs the redox reactions. *Prog. Nucl. Energy* **2014**, *72*, 101–106.
- [22] Lu, X.; Neeway, J. J.; Ryan, J. V.; Du, J. Influence of low concentration V and Co oxide doping on the dissolution behaviors of simplified nuclear waste glasses. *J. Non. Cryst. Solids* **2016**, *452*, 161–168.
- [23] George, S.; Pokhrel, S.; Ji, Z.; Henderson, B. L.; Xia, T.; Li, L.; Zink, J. I.; Nel, A. E.; Mädler, L. Role of Fe doping in tuning the band gap of TiO₂ for the photo-oxidation-induced cytotoxicity paradigm. *J. Am. Chem. Soc.* **2011**, *133*, 11270–11278.
- [24] U.S. Geological Survey, *Mineral Commodity Summaries 2018*; 2018; p 200.
- [25] Sun, J.; Velamakanni, B. V.; Gerberich, W. W.; Francis, L. F. Aqueous latex/ceramic nanoparticle dispersions: colloidal stability and coating properties. *J. Colloid Interface Sci.* **2004**, *280*, 387–399.
- [26] Choi, J.-H.; Kim, S.-O.; Hilton, D. L.; Cho, N. o. Acid-catalyzed kinetics of indium tin oxide etching. *Thin Solid Films* **2014**, *565*, 179–185.

- [27] Tsai, T.-H.; Wu, Y.-F. Organic Acid Mixing to Improve ITO Film Etching in Flat Panel Display Manufacturing. *J. Electrochem. Soc.* **2006**, *153*, C86.
- [28] Tsai, T. H.; Wu, Y. F. Wet etching mechanisms of ITO films in oxalic acid. *Microelectron. Eng.* **2006**, *83*, 536–541.
- [29] Andersen, J. C. Ø.; Cropp, A.; Paradise, D. C. Solubility of indium-tin oxide in simulated lung and gastric fluids: Pathways for human intake. *Sci. Total Environ.* **2017**, *579*, 628–636.
- [30] Lison, D.; Laloy, J.; Corazzari, I.; Muller, J.; Rabolli, V.; Panin, N.; Huaux, F.; Fenoglio, I.; Fubini, B. Sintered Indium-Tin-Oxide (ITO) particles: A new pneumotoxic entity. *Toxicol. Sci.* **2009**, *108*, 472–481.
- [31] Badding, M. A.; Stefaniak, A. B.; Fix, N. R.; Cummings, K. J.; Leonard, S. S. Cytotoxicity and Characterization of Particles Collected from an Indium-Tin Oxide Production Facility. *J. Toxicol. Environ. Heal. - Part A Curr. Issues* **2014**, *77*, 1193–1209.
- [32] Olgun, N. S.; Morris, A. M.; Barber, T. L.; Stefaniak, A. B.; Kashon, M. L.; Schwegler-Berry, D.; Cummings, K. J.; Leonard, S. S. Comparison of the toxicity of sintered and unsintered indium-tin oxide particles in murine macrophage and epidermal cells. *Toxicol. Appl. Pharmacol.* **2017**, *331*, 85–93.
- [33] Badding, M. A.; Fix, N. R.; Orandle, M. S.; Barger, M. W.; Dunnick, K. M.; Cummings, K. J.; Leonard, S. S. Pulmonary toxicity of indium-tin oxide production facility particles in rats. *J. Appl. Toxicol.* **2016**, *36*, 618–626.
- [34] Cummings, K. J.; Nakano, M.; Omae, K.; Takeuchi, K.; Chonan, T.; Xiao, Y. L.; Harley, R. A.; Roggli, V. L.; Hebisawa, A.; Tallaksen, R. J.; Trapnell, B. C.;

- Day, G. A.; Saito, R.; Stanton, M. L.; Suarathana, E.; Kreiss, K. Indium lung disease. *Chest* **2012**, *141*, 1512–1521.
- [35] Blaise, C.; Gagné, F.; Férard, J.; Eullaffroy, P. Ecotoxicity of Selected Nano-Materials to Aquatic Organisms. *Environ. Toxicol.* **2008**, *23*, 591–598.
- [36] Brun, N. R.; Christen, V.; Furrer, G.; Fent, K. Indium and Indium Tin Oxide Induce Endoplasmic Reticulum Stress and Oxidative Stress in Zebrafish (*Danio rerio*). *Environ. Sci. Technol.* **2014**, *48*, 11679–11687.
- [37] Gwinn, W. M.; Qu, W.; Bousquet, R. W.; Price, H.; Shines, C. J.; Taylor, G. J.; Waalkes, M. P.; Morgan, D. L. Macrophage Solubilization and Cytotoxicity of Indium-Containing Particles as *in vitro* Correlates to Pulmonary Toxicity *in vivo*. *Toxicol. Sci.* **2015**, *144*, 17–26.
- [38] Tanaka, A.; Hirata, M.; Matsumura, N.; Koga, K.; Shiratani, M.; Kiyohara, Y. Comparative Study on the Pulmonary Toxicity of Indium Hydroxide, Indium-Tin Oxide, and Indium Oxide Following Intratracheal Instillations into the Lungs of Rats. *MRS Proc.* **2015**, *1723*, mrsf14–1723–g02–03.
- [39] Hornberger, G. M.; Mills, A. L.; Herman, J. S. Bacterial Transport in Porous Media: Evaluation of a Model Using Laboratory Observation. *Water Resources Res.* **1992**, *28*, 915–938.
- [40] Ryan, J. N.; Elimelech, M. Colloid mobilization and transport in groundwater. *Colloids Surfaces A Physicochem. Eng. Asp.* **1996**, *107*, 1–56.
- [41] Dowd, S. E.; Pillai, S. D.; Wang, S.; Corapcioglu, M. Y. Delineating the Specific Influence of Virus Isoelectric Point and Size on Virus Adsorption and Transport through Sandy Soils. *Appl. Environ. Microbiol.* **1998**, *64*, 405–410.

- [42] Filella, M.; Buffle, J. Factors controlling the stability of submicron colloids in natural waters. *Colloids Surfaces A Physicochem. Eng. Asp.* **1993**, *73*, 255–273.
- [43] Keller, A. A.; Wang, H.; Zhou, D.; Lenihan, H. S.; Cherr, G.; Cardinale, B. J.; Miller, R.; Ji, Z. Stability and Aggregation of Metal Oxide Nanoparticles in Natural Aqueous Matrices. *Environ. Sci. Technol.* **2010**, *44*, 1962–1967.
- [44] Hotze, E. M.; Phenrat, T.; Lowry, G. V. Nanoparticle Aggregation: Challenges to Understanding Transport and Reactivity in the Environment. *J. Environ. Qual.* **2010**, *39*, 1909–1924.
- [45] Elimelech, M.; Gregory, J.; Jia, X.; Williams, R. A. *Particle Deposition & Aggregation: Measurement, Modelling, and Simulation*; Butterworth-Heinemann Ltd.: Oxford, 1995.
- [46] Hiemenz, P. C.; Rajagopalan, R. *Principles of Colloid and Surface Chemistry*, 3rd ed.; Marcel Dekker: New York, 1997.
- [47] Hunter, R. J. *Foundations of Colloid Science*, 2nd ed.; Oxford University Press: Oxford, 2001.
- [48] Saleh, N. B.; Pfefferle, L. D.; Elimelech, M. Aggregation Kinetics of Multiwalled Carbon Nanotubes in Aquatic Systems: Measurements and Environmental Implications. *Environ. Sci. Technol.* **2008**, *42*, 7963–7969.
- [49] He, Y. T.; Wan, J.; Tokunaga, T. Kinetic stability of hematite nanoparticles: the effect of particle sizes. *J. Nanoparticle Res.* **2008**, *10*, 321–332.
- [50] Ghosh, S.; Mashayekhi, H.; Bhowmik, P.; Xing, B. Colloidal Stability of Al₂O₃ Nanoparticles as Affected by Coating of Structurally Different Humic Acids. *Langmuir* **2010**, *26*, 873–879.

- [51] Li, K.; Zhang, W.; Huang, Y.; Chen, Y. Aggregation kinetics of CeO₂ nanoparticles in KCl and CaCl₂ solutions: measurements and modeling. *J. Nanoparticle Res.* **2011**, *13*, 6483–6491.
- [52] Xu, C.-y.; Deng, K.-y.; Li, J.-y.; Xu, R.-k. Impact of environmental conditions on aggregation kinetics of hematite and goethite nanoparticles. *J. Nanoparticle Res.* **2015**, *17*, 394.
- [53] Aich, N.; Boateng, L. K.; Sabaraya, I. V.; Das, D.; Flora, J. R. V.; Saleh, N. B. Aggregation Kinetics of Higher-Order Fullerene Clusters in Aquatic Systems. *Environ. Sci. Technol.* **2016**, *50*, 3562–3571.
- [54] Russel, W. B.; Saville, D. A.; Schowalter, W. R. *Colloidal Dispersions*; Cambridge University Press: Cambridge, 1989.
- [55] Chen, K. L.; Elimelech, M. Aggregation and deposition kinetics of fullerene (C₆₀) nanoparticles. *Langmuir* **2006**, *22*, 10994–11001.
- [56] Schudel, M.; Behrens, S. H.; Holthoff, H.; Kretzschmar, R.; Borkovec, M. Absolute Aggregation Rate Constants of Hematite Particles in Aqueous Suspensions: A Comparison of Two Different Surface Morphologies. *J. Colloid Interface Sci.* **1997**, *196*, 241–253.
- [57] Holthoff, H.; Egelhaaf, S. U.; Borkovec, M.; Schurtenberger, P.; Sticher, H. Coagulation Rate Measurements of Colloidal Particles by Simultaneous Static and Dynamic Light Scattering. *Langmuir* **1996**, *12*, 5541–5549.
- [58] Hanus, L. H.; Hartzler, R. U.; Wagner, N. J. Electrolyte-Induced Aggregation of Acrylic Latex. 1. Dilute Particle Concentrations. *Langmuir* **2001**, *17*, 3136–3147.

- [59] Grolimund, D.; Elimelech, M.; Borkovec, M. Aggregation and deposition kinetics of mobile colloidal particles in natural porous media. *Colloids Surfaces A Physicochem. Eng. Asp.* **2001**, *191*, 179–188.
- [60] Dumont, F.; Watillon, A. Stability of Ferric Oxide Hydrosols. *Discuss. Faraday Soc.* **1971**, *52*, 352–360.
- [61] Kim, A. Y.; Berg, J. C. Fractal Aggregation: Scaling of Fractal Dimension with Stability Ratio. *Langmuir* **2000**, *16*, 2101–2104.
- [62] Vikesland, P. J.; Rebodos, R.; Bottero, J.; Rose, J.; Masion, A. Aggregation and sedimentation of magnetite nanoparticle clusters. *Environ. Sci. Nano* **2016**, *3*, 567–577.
- [63] Mylon, S. E.; Chen, K. L.; Elimelech, M. Influence of Natural Organic Matter and Ionic Composition on the Kinetics and Structure of Hematite Colloid Aggregation: Implications to Iron Depletion in Estuaries Steven. *Langmuir* **2004**, *20*, 9000–9006.
- [64] Berka, M.; Rice, J. A. Relation between Aggregation Kinetics and the Structure of Kaolinite Aggregates. *Langmuir* **2005**, *21*, 1223–1229.
- [65] von Smoluchowski, M. Versuch einer mathematischen Theorie der Koagulationskinetik kolloider Lösungen. *Zeitschrift für Phys. Chemie* **1917**, *92*, 129–168.
- [66] Spielman, L. A. Viscous interactions in Brownian coagulation. *J. Colloid Interface Sci.* **1970**, *33*, 562–571.
- [67] Honig, E. P.; Roeberson, G. J.; Wiersema, P. H. Effect of Hydrodynamic Interaction on the Coagulation Rate of Hydrophobic Colloids. *J. Colloid Interface Sci.* **1971**, *36*, 97–109.

- [68] McGown, D. N. L.; Parfitt, G. D. Improved Theoretical Calculation of the Stability Ratio for Colloidal Systems. *J. Phys. Chem.* **1967**, *71*, 449–450.
- [69] Zhang, W.; Crittenden, J.; Li, K.; Chen, Y. Attachment Efficiency of Nanoparticle Aggregation in Aqueous Dispersions: Modeling and Experimental Validation. *Environ. Sci. Technol.* **2012**, *46*, 7054–7062.
- [70] Yato, A.; Papadopoulos, K. D. Stability of polydisperse brownian suspensions. *Colloids and Surfaces* **1985**, *16*, 55–72.
- [71] Cooper, W. D. Coagulation of polydisperse colloidal systems. *Kolloid-Zeitschrift Zeitschrift für Polym.* **1972**, *250*, 38–45.
- [72] Virden, J. W.; Berg, J. C. The Use of Photon Correlation Spectroscopy for Estimating the Rate Constant for Doublet Formation in an Aggregating Colloidal Dispersion. *J. Colloid Interface Sci.* **1992**, *149*, 528–535.
- [73] Jia, M.; Li, H.; Zhu, H.; Tian, R.; Gao, X. An approach for the critical coagulation concentration estimation of polydisperse colloidal suspensions of soil and humus. *J. Soils Sediments* **2013**, *13*, 325–335.
- [74] Li, K.; Chen, Y. Effect of natural organic matter on the aggregation kinetics of CeO₂ nanoparticles in KCl and CaCl₂ solutions: Measurements and modeling. *J. Hazard. Mater.* **2012**, *209-210*, 264–270.
- [75] Chen, K. L.; Elimelech, M. Influence of humic acid on the aggregation kinetics of fullerene (C₆₀) nanoparticles in monovalent and divalent electrolyte solutions. *J. Colloid Interface Sci.* **2007**, *309*, 126–134.
- [76] Zhang, Y.; Chen, Y.; Westerhoff, P.; Hristovski, K.; Crittenden, J. C. Stability of commercial metal oxide nanoparticles in water. *Water Res.* **2008**, *42*, 2204–2212.

- [77] Trinh, L. T. T.; Kjøniksen, A. L.; Zhu, K.; Knudsen, K. D.; Volden, S.; Glomm, W. R.; Nyström, B. Slow salt-induced aggregation of citrate-covered silver particles in aqueous solutions of cellulose derivatives. *Colloid Polym. Sci.* **2009**, *287*, 1391–1404.
- [78] Pamies, R.; Cifre, J. G. H.; Espín, V. F.; Collado-González, M.; Baños, F. G. D.; De La Torre, J. G. Aggregation behaviour of gold nanoparticles in saline aqueous media. *J. Nanoparticle Res.* **2014**, *16*.
- [79] Park, K. S.; Sato, W.; Grause, G.; Kameda, T.; Yoshioka, T. Recovery of indium from In₂O₃ and liquid crystal display powder via a chloride volatilization process using polyvinyl chloride. *Thermochim. Acta* **2009**, *493*, 105–108.
- [80] Kosmulski, M. *Chemical Properties of Material Surfaces*; Marcel Dekker, Inc.: New York, 2001.
- [81] Betts, J. N.; Johnson, M. G.; Rygiewicz, P. T.; King, G. A.; Andersen, C. P. Potential for metal contamination by direct sonication of nanoparticle suspensions. *Environ. Toxicol. Chem.* **2013**, *32*, 889–893.
- [82] Kanehara, M.; Koike, H.; Yoshinaga, T.; Teranishi, T. Indium Tin Oxide Nanoparticles with Compositionally Tunable Surface Plasmon Resonance Frequencies in the Near-IR Region. *J. Am. Chem. Soc.* **2009**, *131*, 17736–17737.
- [83] Dong, A.; Ye, X.; Chen, J.; Kang, Y.; Gordon, T.; Kikkawa, J. M.; Murray, C. B. A generalized ligand-exchange strategy enabling sequential surface functionalization of colloidal nanocrystals. *J. Am. Chem. Soc.* **2011**, *133*, 998–1006.

- [84] Choi, S.-I.; Nam, K. M.; Park, B. K.; Seo, W. S.; Park, J. T. Preparation and Optical Properties of Colloidal, Monodisperse, and Highly Crystalline ITO Nanoparticles. *Chem. Mater.* **2008**, *20*, 2609–2611.
- [85] Green, N. W.; McInnis, D.; Hertkorn, N.; Maurice, P. A.; Perdue, E. M. Suwannee River Natural Organic Matter: Isolation of the 2R101N Reference Sample by Reverse Osmosis. *Environ. Eng. Sci.* **2015**, *32*, 38–44.
- [86] Pecora, R. Dynamic light scattering measurement of nanometer particles in liquids. *J. Nanoparticle Res.* **2000**, *2*, 123–131.
- [87] Laliberté, M. Model for Calculating the Viscosity of Aqueous Solutions. *J. Chem. Eng. Data* **2007**, *52*, 321–335.
- [88] Burns, J. L.; Yan, Y.-d.; Jameson, G. J.; Biggs, S. A Light Scattering Study of the Fractal Aggregation Behavior of a Model Colloidal System. *Langmuir* **1997**, *13*, 6413–6420.
- [89] Zhang, Z.; Zhao, L.; Li, Y.; Chu, M. A Modified Method to Calculate Critical Coagulation Concentration Based on DLVO Theory. *Math. Probl. Eng.* **2015**, *2015*, 1–6.
- [90] Heward, W. J.; Swenson, D. J. Phase equilibria in the pseudo-binary In_2O_3 — SnO_2 system. *J. Mater. Sci.* **2007**, *42*, 7135–7140.
- [91] González, G. B.; Mason, T. O.; Okasinski, J. S.; Buslaps, T.; Honkimäki, V. Determination of the Solubility of Tin in Indium Oxide Using *In Situ* and *Ex Situ* X-Ray Diffraction. *J. Am. Ceram. Soc.* **2012**, *95*, 809–815.
- [92] Kosmulski, M. Pristine Points of Zero Charge of Gallium and Indium Oxides. *J. Colloid Interface Sci.* **2001**, *238*, 225–227.

- [93] Schwarz, J. A.; Driscoll, C. T.; Bhanot, A. K. The Zero Point of Charge of Silica-Alumina Oxide Suspensions. *J. Colloid Interface Sci.* **1984**, *97*, 55–61.
- [94] Kosmulski, M. Compilation of PZC and IEP of sparingly soluble metal oxides and hydroxides from literature. *Adv. Colloid Interface Sci.* **2009**, *152*, 14–25.
- [95] Hsu, J.-P.; Kuo, Y.-C. The Critical Coagulation Concentration of Counterions: Spherical Particles in Asymmetric Electrolyte Solutions. *J. Colloid Interface Sci.* **1997**, *185*, 530–537.
- [96] Omar, F. M.; Aziz, H. A.; Stoll, S. Aggregation and disaggregation of ZnO nanoparticles: Influence of pH and adsorption of Suwannee River humic acid. *Sci. Total Environ.* **2014**, *468-469*, 195–201.
- [97] Liu, X.; Wazne, M.; Han, Y.; Christodoulatos, C.; Jasinkiewicz, K. L. Effects of natural organic matter on aggregation kinetics of boron nanoparticles in monovalent and divalent electrolytes. *J. Colloid Interface Sci.* **2010**, *348*, 101–107.
- [98] Linsebigler, A. L.; Lu, G.; Yates, J. T. Photocatalysis on TiO₂ Surfaces: Principles, Mechanisms, and Selected Results. *Chem. Rev.* **1995**, *95*, 735–758.
- [99] Sakthivel, S.; Hidalgo, M. C.; Bahnemann, D. W.; Geissen, S.-U.; Murugesan, V.; Vogelpohl, A. A fine route to tune the photocatalytic activity of TiO₂. *Appl. Catal. B Environ.* **2006**, *63*, 31–40.
- [100] Kim, W.; Tachikawa, T.; Moon, G. H.; Majima, T.; Choi, W. Molecular-level understanding of the photocatalytic activity difference between anatase and rutile nanoparticles. *Angew. Chemie - Int. Ed.* **2014**, *53*, 14036–14041.

- [101] Sreeja, V.; Jayaprabha, K. N.; Joy, P. A. Water-dispersible ascorbic-acid-coated magnetite nanoparticles for contrast enhancement in MRI. *Appl. Nanosci.* **2015**, *5*, 435–441.
- [102] Chertok, B.; Moffat, B. A.; David, A. E.; Yu, F.; Bergemann, C.; Ross, B. D.; Yang, V. C. Iron oxide nanoparticles as a drug delivery vehicle for MRI monitored magnetic targeting of brain tumors. *Biomaterials* **2008**, *29*, 487–496.
- [103] Sakthivel, S.; Kisch, H. Photocatalytic and photoelectrochemical properties of nitrogen-doped titanium dioxide. *ChemPhysChem* **2003**, *4*, 487–490.
- [104] Mitoraj, D.; Kisch, H. Analysis of Electronic and Photocatalytic Properties of Semiconductor Powders through Wavelength-Dependent Quasi-Fermi Level and Reactivity Measurements. *J. Phys. Chem. C* **2009**, *113*, 20890–20895.
- [105] Kent, R. D.; Vikesland, P. J. Dissolution and Persistence of Copper-Based Nanomaterials in Undersaturated Solutions with Respect to Cupric Solid Phases. *Environ. Sci. Technol.* **2016**, *50*, 6772–6781.
- [106] Kuech, T. R.; Hamers, R. J.; Pederson, J. A. In *Eng. Nanoparticles Environ. Biophys. Process. Toxic.*, 1st ed.; Xing, B., Vecitis, C. D., Senesi, N., Eds.; John Wiley & Sons: Hoboken, New Jersey, 2016; Chapter 14, pp 261–291.
- [107] Stankic, S.; Suman, S.; Haque, F.; Vidic, J. Pure and multi metal oxide nanoparticles: Synthesis, antibacterial and cytotoxic properties. *J. Nanobiotechnology* **2016**, *14*, 1–20.
- [108] Gordon, T.; Perlstein, B.; Houbara, O.; Felner, I.; Banin, E.; Margel, S. Synthesis and characterization of zinc/iron oxide composite nanoparticles and their antibacterial properties. *Colloids Surfaces A Physicochem. Eng. Asp.* **2011**, *374*, 1–8.

- [109] Sharma, N.; Jandaik, S.; Kumar, S.; Chitkara, M.; Sandhu, I. S. Synthesis, characterisation and antimicrobial activity of manganese- and iron-doped zinc oxide nanoparticles. *J. Exp. Nanosci.* **2016**, *11*, 54–71.
- [110] Gilstrap, R. A.; Capozzi, C. J.; Carson, C. G.; Gerhardt, R. A.; Summers, C. J. Synthesis of a nonagglomerated indium tin oxide nanoparticle dispersion. *Adv. Mater.* **2008**, *20*, 4163–4166.
- [111] Lounis, S. D.; Runnerstrom, E. L.; Bergerud, A.; Nordlund, D.; Milliron, D. J. Influence of Dopant Distribution on the Plasmonic Properties of Indium Tin Oxide Nanocrystals. *J. Am. Chem. Soc.* **2014**, *136*, 7110–7116.
- [112] Ma, K.; Zhou, N.; Yuan, M.; Li, D.; Yang, D. Tunable surface plasmon resonance frequencies of monodisperse indium tin oxide nanoparticles by controlling composition, size, and morphology. *Nanoscale Res. Lett.* **2014**, *9*, 547.
- [113] Schimpf, A. M.; Lounis, S. D.; Runnerstrom, E. L.; Milliron, D. J.; Gamelin, D. R. Redox chemistries and plasmon energies of photodoped In_2O_3 and Sn-Doped In_2O_3 (ITO) nanocrystals. *J. Am. Chem. Soc.* **2015**, *137*, 518–524.
- [114] Scholten, M.; Van Den Meerakker, J. E. A. M. On the Mechanism of ITO Etching: The Specificity of Halogen Acids. *J. Electrochem. Soc.* **1993**, *140*, 471.
- [115] Virolainen, S.; Ibane, D.; Paatero, E. Recovery of indium from indium tin oxide by solvent extraction. *Hydrometallurgy* **2011**, *107*, 56–61.
- [116] Kosmulski, M. *Surface Charging and Points of Zero Charge*, 1st ed.; CRC Press: Boca Raton, FL, 2009.

- [117] Grobelny, J.; DelRio, F. W.; Pradeep, N.; Kim, D.-I.; Hackley, V. A.; Cook, R. F. In *Charact. Nanoparticles Intend. Drug Deliv. Methods Mol. Biol. (Methods Protoc.*; McNeil, S., Ed.; Humana Press, 2011; Vol. 697; pp 71–82.
- [118] Rai, D.; Yui, M.; Schaef, H. T.; Kitamura, A. Thermodynamic Model for SnO₂(cr) and SnO₂(am) Solubility in the Aqueous Na⁺-H⁺-OH⁻-Cl⁻-H₂O system. *J. Solution Chem.* **2011**, *40*, 1155–1172.
- [119] Nečas, D.; Klapetek, P. Gwyddion: An open-source software for SPM data analysis. *Cent. Eur. J. Phys.* **2012**, *10*, 181–188.
- [120] Souza, T. G.; Ciminelli, V. S.; Mohallem, N. D. An assessment of errors in sample preparation and data processing for nanoparticle size analyses by AFM. *Mater. Charact.* **2015**, *109*, 198–205.
- [121] López, R.; Gómez, R. Band-gap energy estimation from diffuse reflectance measurements on sol-gel and commercial TiO₂: a comparative study. *J. Sol-Gel Sci. Technol.* **2012**, *61*, 1–7.
- [122] Sangiorgi, N.; Aversa, L.; Tatti, R.; Verucchi, R.; Sanson, A. Spectrophotometric method for optical band gap and electronic transitions determination of semiconductor materials. *Opt. Mater. (Amst).* **2017**, *64*, 18–25.
- [123] Dolgonos, A.; Mason, T. O.; Poeppelmeier, K. R. Direct optical band gap measurement in polycrystalline semiconductors: A critical look at the Tauc method. *J. Solid State Chem.* **2016**, *240*, 43–48.
- [124] Ishibashi, K.; Fujishima, A.; Watanabe, T.; Hashimoto, K. Detection of active oxidative species in TiO₂ photocatalysis using the fluorescence technique. *Electrochem. commun.* **2000**, *2*, 207–210.

- [125] Hirakawa, T.; Nosaka, Y. Properties of $\text{O}_2^{\bullet-}$ and OH^\bullet Formed in TiO_2 aqueous suspensions by photocatalytic reaction and the influence of H_2O_2 and some ions. *Langmuir* **2002**, *18*, 3247–3254.
- [126] Jing, Y.; Chaplin, B. P. Mechanistic Study of the Validity of Using Hydroxyl Radical Probes to Characterize Electrochemical Advanced Oxidation Processes. *Environ. Sci. Technol.* **2017**, *51*, 2355–2365.
- [127] Page, S. E.; Arnold, W. A.; McNeill, K. Terephthalate as a probe for photochemically generated hydroxyl radical. *J. Environ. Monit.* **2010**, *12*, 1658–1665.
- [128] Brown, P. L.; Ekberg, C. *Hydrolys. Met. Ions*, 1st ed.; Wiley-VCH Verlag GmbH & Co. KGaA: Weinheim, Germany, 2016; Chapter 13, pp 757–833.
- [129] Wood, S. A.; Samson, I. M. The aqueous geochemistry of gallium, germanium, indium and scandium. *Ore Geol. Rev.* **2006**, *28*, 57–102.
- [130] Stumm, W.; Morgan, J. *Aquatic Chemistry: Chemical Equilibria and Rates in Natural Waters*, 3rd ed.; John Wiley & Sons: New York, 1996.
- [131] Harrell, J.; Acikgoz, M.; Lieber Sasson, H.; Visoly-Fisher, I.; Genova, A.; Pavanello, M. Models of Surface Morphology and Electronic Structure of Indium Oxide and Indium Tin Oxide for Several Surface Hydroxylation Levels. *J. Phys. Chem. C* **2018**, *122*, 584–595.
- [132] Zhou, C.; Li, J.; Chen, S.; Wu, J.; Heier, K. R.; Cheng, H. First-Principles Study on Water and Oxygen Adsorption on Surfaces of Indium Oxide and Indium Tin Oxide Nanoparticles. *J. Phys. Chem. C* **2008**, *112*, 14015–14020.

- [133] Purvis, K. L.; Lu, G.; Schwartz, J.; Bernasek, S. L. Surface characterization and modification of indium tin oxide in ultrahigh vacuum. *J. Am. Chem. Soc.* **2000**, *122*, 1808–1809.
- [134] Nüesch, F.; Forsythe, E. W.; Le, Q. T.; Gao, Y.; Rothberg, L. J. Importance of indium tin oxide surface acido basicity for charge injection into organic materials based light emitting diodes. *J. Appl. Phys.* **2000**, *87*, 7973–7980.
- [135] Donley, C.; Dunphy, D.; Paine, D.; Carter, C.; Nebesny, K.; Lee, P.; Alloway, D.; Armstrong, N. R. Characterization of indium-tin oxide interfaces using X-ray photoelectron spectroscopy and redox processes of a chemisorbed probe molecule: Effect of surface pretreatment conditions. *Langmuir* **2002**, *18*, 450–457.
- [136] Brumbach, M.; Veneman, P. A.; Matrikar, F. S.; Schulmeyer, T.; Simmonds, A.; Xia, W.; Lee, P.; Armstrong, N. R. Surface composition and electrical and electrochemical properties of freshly deposited and acid-etched indium tin oxide electrodes. *Langmuir* **2007**, *23*, 11089–11099.
- [137] White, J. L.; Bocarsly, A. B. Enhanced Carbon Dioxide Reduction Activity on Indium-Based Nanoparticles. *J. Electrochem. Soc.* **2016**, *163*, H410–H416.
- [138] Furrer, G.; Stumm, W. The coordination chemistry of weathering I: Dissolution kinetics of δ -Al₂O₃ and BeO. *Geochim. Cosmochim. Acta* **1986**, *50*, 1847–1860.
- [139] Wang, T.; Radovanovic, P. Free Electron Concentration in Colloidal Indium Tin Oxide Nanocrystals Determined by Their Size and Structure. *J. Phys. Chem. C* **2011**, *115*, 406–413.
- [140] King, P. D. C.; Veal, T. D.; Fuchs, F.; Wang, C. Y.; Payne, D. J.; Bourlange, A.; Zhang, H.; Bell, G. R.; Cimalla, V.; Ambacher, O.; Egdell, R. G.; Bechstedt, F.;

- McConville, C. F. Band gap, electronic structure, and surface electron accumulation of cubic and rhombohedral In_2O_3 . *Phys. Rev. B - Condens. Matter Mater. Phys.* **2009**, *79*, 1–10.
- [141] Walsh, A.; Da Silva, J. L.; Wei, S. H.; Körber, C.; Klein, A.; Piper, L. F.; Demasi, A.; Smith, K. E.; Panaccione, G.; Torelli, P.; Payne, D. J.; Bourlange, A.; Egdell, R. G. Nature of the band gap of In_2O_3 revealed by first-principles calculations and X-ray spectroscopy. *Phys. Rev. Lett.* **2008**, *100*, 2–5.
- [142] Jassby, D.; Farner Budarz, J.; Wiesner, M. Impact of aggregate size and structure on the photocatalytic properties of TiO_2 and ZnO nanoparticles. *Environ. Sci. Technol.* **2012**, *46*, 6934–6941.

Vita

James Sylvester Grundy was born and raised in Bemidji, Minnesota. After graduating from Bemidji High School in 2005, he enrolled at Harvard University and received a Bachelor of Science degree in Engineering Sciences (Environmental track) in 2009. Following college, James worked at TRC Environmental, Inc. in Lowell, Massachusetts, on environmental remediation projects across the northeast United States. He matriculated at the University of Texas at Austin in the fall of 2011 and completed a Masters of Science in Engineering in Environmental and Water Resources Engineering in 2013 under the guidance of Professor Danny Reible and Professor Lynn Katz before continuing onto the PhD program in Civil Engineering under the supervision of Professor Lynn Katz. James has accepted a postdoctoral fellowship position under the supervision of Professor Qingxia Liu in the Department of Chemical and Materials Engineering at the University of Alberta in Edmonton, Alberta, Canada, following the completion of his PhD.

Permanent email: jgrundy@utexas.edu

This dissertation was typeset with L^AT_EX by the author.